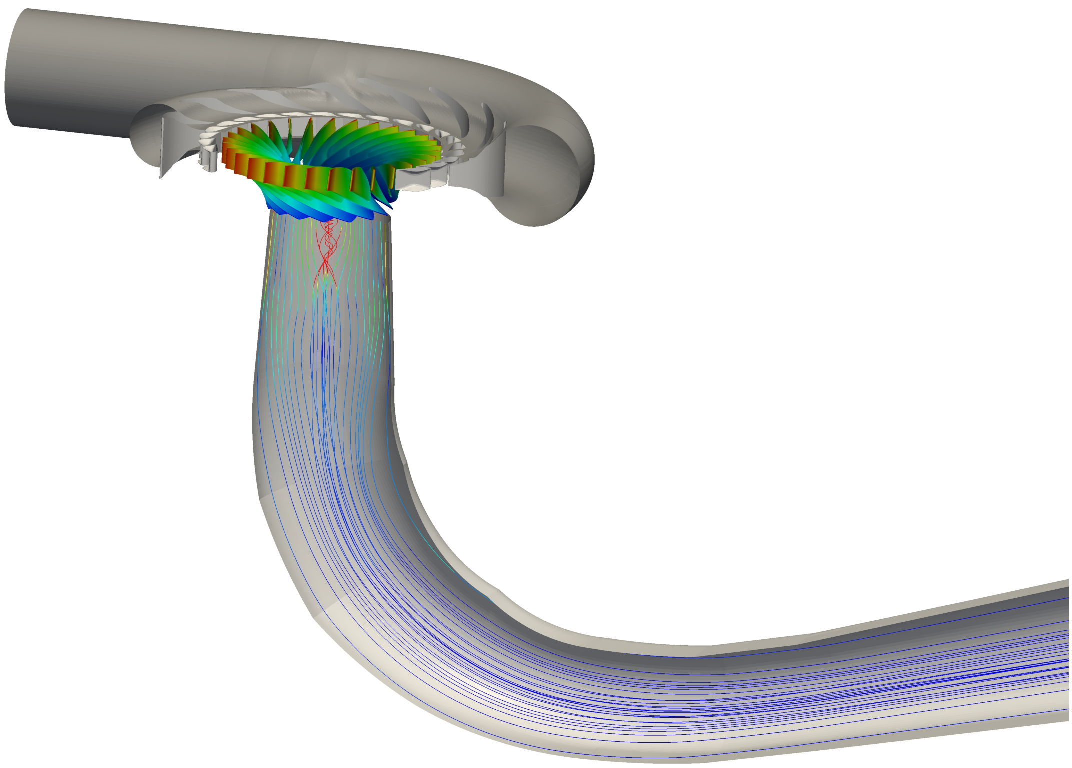

Numerical simulations of the flow in the Francis-99 turbine

Steady and unsteady simulations at different operating points

Master's thesis in applied mechanics

LUCIEN STOESSEL

Department of Applied Mechanics
Division of Fluid Mechanics
CHALMERS UNIVERSITY OF TECHNOLOGY
Göteborg, Sweden 2014

Master's thesis 2014:67

MASTER'S THESIS IN APPLIED MECHANICS

Numerical simulations of the flow in the Francis-99 turbine

Steady and unsteady simulations at different operating points

LUCIEN STOESSEL

Department of Applied Mechanics
Division of Fluid Mechanics
CHALMERS UNIVERSITY OF TECHNOLOGY

Göteborg, Sweden 2014

Numerical simulations of the flow in the Francis-99 turbine
Steady and unsteady simulations at different operating points
LUCIEN STOESSEL

Master's thesis 2014:67
ISSN 1652-8557
Department of Applied Mechanics
Division of Fluid Mechanics
Chalmers University of Technology
SE-412 96 Göteborg
Sweden
Telephone: +46 (0)31-772 1000

Cover:
Time-averaged flow in the Francis-99 turbine at best efficiency point. The streamlines are coloured by velocity, the blades by static pressure.

Chalmers Reproservice
Göteborg, Sweden 2014

Numerical simulations of the flow in the Francis-99 turbine
Steady and unsteady simulations at different operating points
Master's thesis in applied mechanics
LUCIEN STOESSEL
Department of Applied Mechanics
Division of Fluid Mechanics
Chalmers University of Technology

Abstract

In a modern electricity generation framework, hydroturbines are used to stabilise the grid and equilibrate supply variations of other renewable energy sources and are therefore often operated at off-design conditions. In this thesis, the scale model of a high-head Francis turbine is investigated at part load, best efficiency point and high load using a finite volume method in OpenFOAM. The investigated Francis-99 turbine is the subject of an upcoming workshop, and the scale model has been investigated experimentally. The geometry, an initial hexahedral mesh and the proposed operating points are therefore taken from the workshop specifications. The mesh is then adapted for the different simulations. Steady-state RANS simulations are conducted with only one guide vane and blade channel and without the spiral casing, and a mixing plane interface is used between the stationary and rotating parts. Different variants of the k-ε and k-ω turbulence models are used and a linear explicit algebraic Reynolds stress model is implemented and compared to the other models. Time-resolved URANS simulations are performed including the entire turbine geometry, using a sliding grid method with a general grid interface between the runner and the stationary parts. For the unsteady simulations, the k-ω SSTF model is implemented and used in addition to the standard k-ε model. The data from both types of simulations is compared to numerical and experimental results, and both the steady and unsteady simulations give a good prediction of the pressure distribution in the turbine. The velocity profiles at the runner outlet are well predicted at off-design conditions, but a strong swirl is obtained at best efficiency point which is not observed in the experiments. The accuracy of the velocity and pressure prediction of the mixing plane simulations is equivalent to the unsteady results, and for both types of simulations, the main differences occur in the region below the hub at the runner outlet. While the steady-state simulations overestimate the efficiency due to the assumption of axiperiodic flow in the runner and the circumferential averaging of the flow field at the mixing plane interface, the unsteady simulations give good predictions of the experimental results at best efficiency point (error of 1.16%) with larger errors at part load (10.67%) and high load (2.72%). Through the use of Fourier decomposition, the pressure fluctuations in the turbine are analysed, and the main rotor-stator interaction frequencies are predicted correctly at all operating conditions. The main pressure oscillations occur at the frequencies which are multiples of the number of guide vanes and blades. Furthermore, the feasibility of simulations with oscillations in rotational speed is examined at best efficiency point, and the added stiffness due to the fluid loading is extracted. The results show that oscillations at the frequency which is examined are not prone to resonance and divergence, but further investigation of the mechanical properties of the turbines and possible oscillation frequencies is needed for a detailed picture of the dynamical behaviour.

Keywords: Hydropower, Francis Turbine, OpenFOAM, Mixing Plane, Sliding Grid, Turbulence Modelling, EARSM, Runner Oscillations

Preface

This work has been conducted as a Master's thesis in the scope of a degree in mechanical engineering at Ecole polytechnique fédérale de Lausanne (EPFL). It took place in the context of a student exchange program between Chalmers University of Technology in Göteborg and EPFL, and the regulations from both institutions were followed wherever possible. The work was supervised at Chalmers by Prof. Håkan Nilsson at the division of fluid mechanics, while the administrative supervision at EPFL was taken by Prof. François Avellan at the laboratory of hydraulic machines (LMH). The turbine model that was simulated is used in the Francis-99 workshop that will take place in Norway in December 2014, and it is planned to use the results from this thesis as a contribution to the workshop. The guidelines published by the workshop organisers were therefore closely followed wherever possible, in order to allow a meaningful comparison with other results and a useful contribution to the workshop. As OpenFOAM is widely used for CFD at the division of fluid mechanics at Chalmers, it was the software of choice for the present work. Due to the fact that the C++ - based OpenFOAM environment differs from classical commercial CFD software, a considerable amount of work was invested in the understanding and correct usage of the code. Given that OpenFOAM is an open-source project and under constant development, this work can also be seen as a validation case for certain features specifically designed for turbomachinery usage. Wherever necessary, personal additions to OpenFOAM were made in order to achieve specific goals of the thesis work.

Acknowledgements

First of all I would like to express my gratitude to my supervisors, Prof. Håkan Nilsson and Prof. François Avellan, for accepting the responsibility for this thesis and supporting me throughout the course of this work. In particular, I would like to thank Håkan and the whole division of fluid dynamics at Chalmers for creating such a stimulating and friendly working atmosphere, for all the inspiring scientific discussions and the nice chats in between, which made it a pleasure to work at the division during the whole duration of my stay. Special thanks go to Ardalan Javadi, who supported me with his great experience in turbomachinery simulations and contributed with a lot of tips and details. My thanks go also to the Swedish national infrastructure for computing (SNIC) and the Chalmers centre for computational science and engineering (C^3SE) for providing the computational resources for this thesis, as well as valuable support for the computations. Furthermore, I appreciate the relentless effort made by Martin Beaudoin and Prof. Hrvoje Jasak for the continuous improvement of OpenFOAM, as well as their open-mindedness to discussions and specific issues regarding this thesis. In addition, I would like to thank Prof. Thomas Gmür and Dr. Matteo Galli from SGM, and the international offices at EPFL and Chalmers (in particular Eliane Reuille and Per-Anders Träff) for their support with all the administrative issues of this exchange.

Finally, I would like to thank my friends and family who supported me throughout my studies, and encouraged me to take the opportunity and launch myself into this interesting and challenging exchange in Sweden.

Nomenclature

Variable	Symbol	SI units [other]
Diameter	D	m
Density	ρ	kg/m^3
Pressure	p	Pa $[bar]$
Gravitational acceleration	g	m/s^2
Volumetric discharge	Q	m^3/s
Specific hydraulic energy	E, gH	J/kg
Hydrostatic head	H	m
Angular velocity	ω	s^{-1}
Rotational speed	N	rpm
Rotational frequency	n	s^{-1}
Absolute flow velocity	C	m/s
Tangential velocity component	Cu	m/s
Meridional velocity component	Cm	m/s
Blade rotation velocity	U	m/s
Relative flow velocity	W	m/s
Vorticity	Ω	s^{-1}

Indices, exponents and symbols	Meaning
$\dot{}$	First time derivative
$\ddot{}$	Second time derivative
$<>$	Time average
$\overrightarrow{v}$	Vector
v_i	Vector in index notation
$\mathbf{T}$	Tensor
T_{ij}	Tensor in index notation
$\vert \quad \vert$	Absolute value
$\Vert \quad \Vert$	Norm of a vector or tensor
x	X component of a vector field
y	Y component of a vector field
z	Z component of a vector field
R	Radial component of a vector field
θ	Tangential component of a vector field
I	High specific energy reference section of the turbine
$\bar{I}$	Low specific energy reference section of the turbine

Abbreviation	Meaning
RANS	Reynolds-averaged Navies-Stokes
URANS	Unsteady Reynolds-averaged Navies-Stokes
CFD	Computational fluid dynamics
GGI	General grid interface
MRF	Multiple rotating frames of reference
IEC	International Electrotechnical Commission
EPFL	École polytechnique fédérale de Lausanne

Contents

1 Introduction

With the appearance of renewable energy sources which depend strongly on weather conditions and can destabilise the balance between demand and supply, the need for flexible and fast-reacting equilibration of the electric power grid has arisen. Hydropower plants are well suited for this purpose as they are able to change operating point within a short time frame if the supply by solar and wind power is insufficient [1, 2]. On the other hand, excess energy from renewable sources can be stored in dams and then reconverted into electricity through water turbines. In mountainous regions in northern Europe, high head Francis turbines are often used to complete this task. However, hydro-turbines are traditionally designed for steady operation at a single operating point where the efficiency is maximised. This point is characterised by a stable flow with minimal swirl at the turbine outlet, resulting in dynamically favourable operating conditions with little flow instabilities and runner vibrations. In contrast, off-design operating points which are necessary for grid stabilisation lead to more complex flow through the turbine, in particular with the creation of swirl at the runner outlet [3]. Such unsteady flow features can lead to fluid-structure interaction phenomena which create oscillating forces on the runner [4, 5]. Investigating the performance as well as the flow field both at design and off-design conditions is therefore needed if the turbine is to be used in a modern electricity production framework. Flow features and their origin must be understood in order to maximise the efficiency, deliver the requested power and avoid operating the turbine in unstable conditions. Predicting correctly the pressure and velocity field as well as the performance of the turbine is therefore of great interest. In order to achieve accurate predictions of the flow, the use and comparison of advanced turbulence models is inevitable. While for research purposes a detailed knowledge of the unsteady flow is needed, simpler steady-state simulations can be sufficient for design and performance optimisation applications [6]. The complexity of the problem can be adapted depending on the specific needs of the application, by means such as geometry simplifications and symmetry assumptions. All of these tools need to be validated by comparison with experimental measurements and other more advanced numerical simulations, allowing to choose the appropriate tool for a specific application that produces the desired results and accuracy without overly costly and complex simulations.

1.1 Context, previous work and relevant literature

The results from this work will be the base of a contribution to the first Francis-99 workshop, which will be held at NTNU in Trondheim in December 2014. This series of workshops is aimed at using a scale model of the high-head Francis turbine installed at the Tokke power plant in Norway as a reference case for numerical and experimental methods related to Francis turbines. The focus of the first workshop is on steady turbine operation at both the best efficiency point and off-design conditions, both of which have been examined extensively at NTNU in a series of experiments [7, 8]. Experimental data for the workshop was obtained from the test rig at NTNU, using a number of stationary and moving pressure probes across the entire turbine. Trivedi *et al.* [7] performed URANS simulations of the complete turbine at the three proposed operating points. Different turbulence models were used, and good agreement with experimental data was obtained. In view of the upcoming workshop, further experiments with velocity measurements at the runner outlet were conducted [8]. All this data serves as a guideline for the simulations throughout the work and forms the basis for the evaluation of the results.

The OpenFOAM software and the included tools for turbomachinery simulations have been successfully validated and applied on complex hydro-power simulation cases by Nilsson [9], Petit [10] and Javadi [11]. Tools for steady-state turbomachinery simulations were developed and tested by Page *et al.* [12]. Petit *et al.* [13] performed a case study that showed the validity of OpenFOAM for unsteady sliding grid simulations of swirling flows. Zhang and Zhang [14] used OpenFOAM on high head Francis turbines, and included a model for cavitation. Recent work on Francis turbines at off-design conditions using commercial software was performed by Nicolet *et al.* [5] for part load, by Shingai *et al.* [3] for high load operation, and finally by Trivedi *et al.* [7] in view of the upcoming workshop. Susan-Resiga *et al.* [15] also included efforts to reduce the computational effort by the use of symmetry assumptions. The use of different turbulence models for RANS simulations of Francis turbines was investigated and compared to experiments at best efficiency point by Maruzewski *et al.* [16], while Wu *et al.* [17] validated their turbulence model in various operating conditions.

1.2 Aim and scope of the work

The aim of this thesis is to obtain an accurate prediction of the flow field and turbine performance with OpenFOAM at the proposed operating points. Steady-state RANS simulations produce a computationally cheap solution of the problem. Unsteady RANS simulations are aimed to provide more complete information about the performance of the turbine and time-dependent phenomena in the flow field, but need considerably larger computational resources. The comparison with experimental and numerical data by other authors allows an evaluation of the results from these two types of simulations.

In addition to the simulations at fixed operating conditions, unsteady simulations with variations in rotational speed are used to investigate the behaviour of the turbine under certain basic types of runner oscillations. Assessing the effect of such oscillations on the flow field is important to evaluate the stability of operating points and predict the behaviour of the turbine if vibrations arise. A further path of advancement is the implementation of more advanced turbulence models which are not yet implemented in the current versions of OpenFOAM. Most classical turbulence models are included in current distributions and have been extensively validated [9, 13, 18], but more complex and recently developed models are constantly appearing, and using them on turbomachinery cases opens up interesting perspectives for future simulations and projects. While new models are often validated on simple geometries and well-established flow cases, there is in general very little known about their performance in complex flow cases and rotating geometries such as a complete Francis turbine.

Summing up, the aim of the present work is twofold: The main goal is to produce a meaningful contribution to the Francis-99 workshop by performing steady and unsteady simulations at different operating points. The second goal is to simulate basic runner oscillations, and to compare recently developed and newly implemented turbulence models to the well-established and validated models.

2 Problem description and theoretical background

2.1 Description of the turbine

The Francis-99 turbine is a high-head Francis turbine with 15 full-length runner blades and 15 splitter blades, with a distributor consisting of 14 stay vanes and 28 guide vanes. The prototype has a runner outlet diameter $D = 1.779m$, a rated head of $H = 377m$ and a rated output power of 110MW. The model turbine which is the subject of this thesis has a runner outlet diameter $D = 0.349m$ and a rated head of $H = 12m$ [8]. A cut view of the entire turbine geometry with all the components is shown in Figure 2.1. A particularity of the turbine is the long and thin draft tube. The distance between the runner outlet and the elbow is very large, and the diffuser is particularly long. The turbine is limited by the inlet section I at the inlet of the spiral casing, and the outlet section $\bar{I}$ at the draft tube outlet.

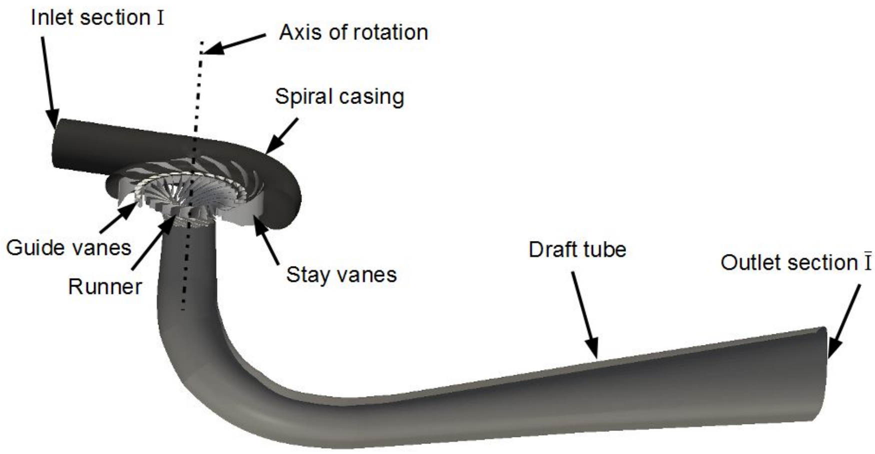

Figure 2.1: *Cut view of the entire turbine geometry.*

2.2 Definitions

Quantities such as power, efficiency and non-dimensional factors are defined in the norms of the International Electrotechnical Commission [19]. Wherever possible, these internationally standardised and accepted definitions are used in order to avoid any confusion between the various conventions. The Francis-99 committee uses however slightly different definitions in some cases.

2.2.1 Coordinate system

The coordinate system for the simulations is given by the supplied geometry. A right-handed Cartesian coordinate system is used (see Figure 2.2), with the z axis located on the runner axis. The origin of the system is located in the mean plane of the guide vane passage. The x axis is parallel to the spiral casing inlet tube and oriented in the direction of the draft tube. Finally, the y axis is perpendicular to both the rotation axis and the draft tube and lies in the plane defined by the guide vane passage.

2.2.2 Efficiency

The IEC standards for model testing [19] provide definitions of the different efficiencies of hydroturbines. First of all, the specific hydraulic energy at an arbitrary section i in the flow is defined as

$$gH_i = \frac{p_i}{\rho} + \frac{C_i^2}{2} + gz_i = \frac{p_i}{\rho} + \frac{Q^2}{2A_i^2} + gz_i, \tag{2.1}$$

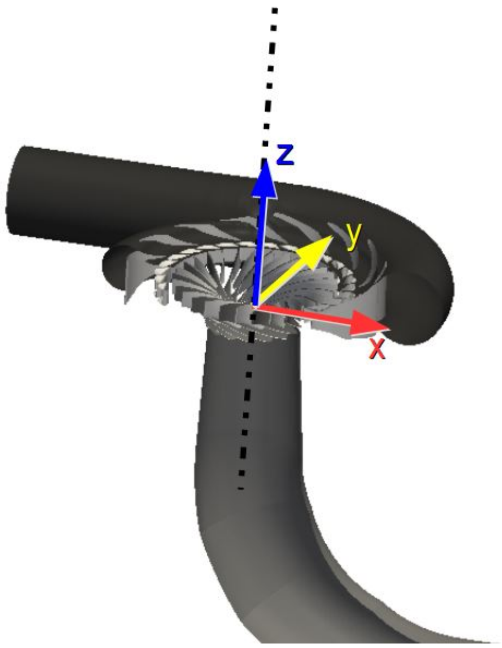

Figure 2.2: *View of the coordinate system.*

where z_i is the elevation with respect to an arbitrarily chosen reference level. Using this definition to calculate the difference between the turbine inlet section I and the outlet section $\bar{I}$ (see Figure 2.1), the available specific energy at the turbine is

$$E = gH_I - gH_{\bar{I}}. \tag{2.2}$$

The hydraulic power which is available at the turbine is therefore calculated as

$$P_h = \rho \cdot Q \cdot E. \tag{2.3}$$

If leakage losses due to a clearance in the runner are considered, the actual flow Q_t going through the turbine runner is given by

$$Q_t = Q \cdot \eta_q, \tag{2.4}$$

where η_q is the volumetric efficiency. The specific energy which is actually transferred to the turbine is

$$E_t = E \cdot \eta_e, \tag{2.5}$$

where η_e is the energetic efficiency [1]. The mechanical power experienced by the turbine shaft at the runner is thus

$$P_t = \rho \cdot Q_t \cdot E_t = T_m \cdot \omega, \tag{2.6}$$

with ω being the angular speed of the turbine runner and T_m the torque transmitted from the runner to the shaft. The hydraulic efficiency of the turbine is then

$$\eta_h = \frac{P_t}{P_h} = \frac{\rho \cdot Q_t \cdot E_t}{\rho \cdot Q \cdot E} = \eta_q \cdot \eta_e. \tag{2.7}$$

Note that η_e is not defined in the IEC norm and is simply included in the hydraulic efficiency η_h together with the volumetric efficiency η_q. The energetic efficiency η_e is however useful to obtain a coherent nomenclature for all contributions to η_h and get a complete picture of the physical mechanisms that take place within the turbine. Volumetric losses are neglected during the simulations as no clearance is modelled in the geometry, therefore we assume $Q_t = Q$ and $\eta_q = 1$, and thus $\eta_h = \eta_e$. This assumption is widely used for simulations of Francis turbines and has been confirmed in comparison with experimental measurements by Maruzewski *et al.*

[16]. Introducing the mechanical losses in the bearings and other friction losses, the mechanical power of the turbine is given by

$$P = \omega \cdot T = \omega \cdot (T_m - T_{LM}). \tag{2.8}$$

The mechanical efficiency η_m is then defined as

$$\eta_m = \frac{P}{P_t} = \frac{T_m - T_{LM}}{\rho \cdot Q_t \cdot E_t}. \tag{2.9}$$

Note that the mechanical efficiency is of minor interest for CFD simulations, but can be calculated from the hydraulic quantities if experimental values of the friction torque are available. This is of importance for experimental measurements, as the torque is in general measured at a position of the shaft where mechanical losses can not be eliminated. The overall turbine efficiency η can finally be calculated by the expression

$$\eta = \frac{P}{P_h} = \frac{T \cdot \omega}{\rho \cdot Q \cdot E} = \frac{T \cdot \omega}{\rho \cdot Q \cdot (gH_I - gH_{\bar{I}})}. \tag{2.10}$$

Further aspects such as the efficiency of the electrical machine will not be treated as they would go beyond the scope of this work. Note that the Francis-99 workshop committee [8] uses a different definition of the available specific energy (equations 2.1 and 2.2), where the available specific energy is defined as consisting only of the difference in total pressure between the inlet and outlet of the turbine

$$\Delta p_0 = p_{0,I} - p_{0,\bar{I}} = p_I - p_{\bar{I}} + \frac{\rho Q^2}{2} \cdot \left(\frac{1}{A_I^2} - \frac{1}{A_{\bar{I}}^2}\right). \tag{2.11}$$

This corresponds to neglecting the potential energy term $g \cdot z$ in equation 2.1. Depending on the operating conditions and turbine geometry, this term is however not negligible. In the following sections, a distinction will therefore be made between the two definitions, with $\eta_{h,IEC}$ denoting the hydraulic efficiency according to the IEC norm, while the definition used by the Francis-99 committee will be called $\eta_{h,F99}$ and is given by

$$\eta_{h,F99} = \frac{P_t}{\rho Q_t \Delta p_0}. \tag{2.12}$$

2.2.3 Dimensionless parameters

If the results are to be scaled and compared between turbines of different sizes or geometries, the use of non-dimensional parameters allows a more general representation of the operating conditions than dimensional quantities. Different conventions and definitions exist for a non-dimensional description of hydro-turbines, but the definitions in the IEC standards [19] are used in the present work. If a reference radius R is chosen, the head of the turbine can be normalised using the reference specific energy constructed from the blade speed $u = \omega R$, which gives the definition of the specific energy coefficient

$$\Psi = \frac{2E}{U^2} = \frac{2E}{\omega^2 R^2}. \tag{2.13}$$

Note that the factor 2 is omitted by some authors, but is kept in the IEC standards and maintains the physical meaning of the reference specific energy. Similarly, the discharge is normalised by a reference section and a reference discharge constructed from the blade velocity, yielding the discharge coefficient

$$\varphi = \frac{Q}{UA} = \frac{Q}{\pi U R^2} = \frac{Q}{\pi \omega R^3}. \tag{2.14}$$

Using these non dimensional numbers, the specific speed of the turbine can be defined as

$$\nu = \frac{\omega}{\pi^{\frac{1}{2}} 2^{\frac{3}{4}}} \frac{Q^{\frac{1}{2}}}{E^{\frac{3}{4}}} = \frac{\varphi^{\frac{1}{2}}}{\Psi^{\frac{3}{4}}}. \tag{2.15}$$

In the following calculations, the reference radius R is the radius of the runner outlet $R_{ref} = 0.1745m$. The coefficients Ψ and φ are commonly used to represent the non-dimensional hill chart [1]. As both of these parameters use the rotational speed as a reference they are mainly suited for the representation of steady-state operation. The IEC defines dimensionless numbers that are better suited for the description of transient phenomena. The discharge factor is

$$Q_{ED} = \frac{Q}{D^2\sqrt{E}}, \tag{2.16}$$

while the speed factor is given by

$$n_{ED} = \frac{nD}{\sqrt{E}}. \tag{2.17}$$

These dimensionless numbers present the advantage of being normalised by a quantity which is independent of the speed of rotation. However, using the available specific energy as a reference can be problematic in CFD: If the predicted losses in the machine are higher than in reality, this will modify the complete non-dimensional operating point. If on the other hand Ψ and φ are used, only the specific energy coefficient Ψ is affected.

2.3 Operating points

Three operating points are specified by the organisers of the workshop [8] and have been investigated experimentally and numerically [7]: One at best efficiency point, one at lower part load ($Q_{ED}/Q_{ED,BEP} = 0.34$) and one at high load ($Q_{ED}/Q_{ED,BEP} = 1.09$). Table 2.1 shows the flow conditions for all three operating points. Note that in table 2.1, the hydraulic efficiency as calculated by the workshop committee (equation 2.12) is given rather than the one defined by the IEC (equation 2.7). During the experimental velocity measurements, problems with the test rig appeared when experiments were performed at the given operating points for best efficiency point and high load [8]. The operating conditions were therefore slightly changed in a way that keeps the non-dimensional factors constant. The two new operating points are presented in table 2.2. All steady-state simulations are conducted at both the old and the new operating conditions in order to allow a proper comparison with the experimental data. Due to the large computational effort, the unsteady simulations are only performed at the original operating points.

Parameter	Part load	BEP	High load
Net head $[m]$	12.29	11.91	11.84
Flow rate $[\frac{m^3}{s}]$	0.071	0.203	0.221
Runner rotational speed $[rpm]$	406.2	335.4	369.6
Efficiency $\eta_{h,F99}[\%]$	71.69	92.61	90.66
Torque $[Nm]$	137.52	619.56	597.99
Friction torque $[Nm]$	6.54	8.85	7.63
Differential pressure $[kPa]$	120.39	114.98	114.03
Inlet pressure $[kPa]$	219.93	216.54	210.01
Outlet pressure $[kPa]$ [1]	99.54	101.56	95.98
Density $[\frac{kg}{m^3}]$	999.23	999.19	999.20
Kinematic viscosity $[\frac{m^2}{s}]$	$9.57 \cdot 10^{-7}$	$9.57 \cdot 10^{-7}$	$9.57 \cdot 10^{-7}$
$\Psi[-]$	4.381	6.228	5.098
$\varphi[-]$	0.099	0.346	0.342
$\nu[-]$	0.104	0.149	0.172
$Q_{ED}[-]$	0.053	0.154	0.168
$n_{ED}[-]$	0.215	0.180	0.199

Table 2.1: Physical parameters for the three original operating points [8].

2.4 Oscillations in rotational speed

A detailed and realistic prediction of the types of oscillations that can arise and whether they are dampened or amplified would need comprehensive knowledge of the electrical machine and the mechanical properties of

[1] Calculated from inlet and differential pressure

Parameter	BEP	High load
Net head $[m]$	12.77	12.61
Flow rate $[\frac{m^3}{s}]$	0.21	0.23
Runner rotational speed $[rpm]$	344.4	380.4
Efficiency $\eta_{h,F99}[\%]$	92.4	91.0
$\Psi[-]$	6.333	5.126
$\varphi[-]$	0.349	0.346
$\nu[-]$	0.148	0.173
$Q_{ED}[-]$	0.154	0.168
$n_{ED}[-]$	0.180	0.199

Table 2.2: Physical parameters for the two new operating points [8].

the turbine. Some basic oscillations can however be simulated with a simple model. Starting from unsteady simulations with constant rotational speed, the appearing torque oscillations can be extracted and used as possible vibration frequencies. If only a simple sinusoidal oscillation is considered, the angle of the runner with respect to the equilibrium position is expressed as

$$\tilde{\theta}(t) = \hat{\theta}\sin(\omega t), \tag{2.18}$$

where $\hat{\theta}$ is the amplitude of the oscillation and ω is the pulsation. By derivation of this expression, the instantaneous oscillation velocity is obtained as

$$\dot{\tilde{\theta}}(t) = \hat{\theta}\omega\cos(\omega t) = \hat{\theta}\omega\sin(\omega t + \frac{\pi}{2}), \tag{2.19}$$

or expressed in terms of rotation frequency

$$\tilde{n}(t) = \frac{\hat{\theta}\omega}{2\pi}\sin(\omega t + \frac{\pi}{2}) = \hat{n}\sin(\omega t + \frac{\pi}{2}), \tag{2.20}$$

where

$$\hat{n} = \frac{\hat{\theta}\omega}{2\pi} \tag{2.21}$$

is the amplitude of the runner speed oscillation. As this expression gives the movement around an equilibrium position which is moving at the rotational speed of the runner, the instantaneous rotational speed becomes

$$n(t) = n_0 + \tilde{n}(t) = n_0 + \hat{n}\sin(\omega t + \frac{\pi}{2}) = n_0 + \hat{n}\sin(\omega(t + t_0)), \tag{2.22}$$

where

$$t_0 = \frac{\pi/2}{\omega} \tag{2.23}$$

is the phase shift between the runner oscillation and the oscillation in rotational speed. When the turbine is oscillating, the fluid forces acting on the runner will lead to an additional torque $\tilde{T}(t)$, which can be decomposed into components in phase with the displacement, velocity and acceleration of the runner movement respectively to obtain the coefficients of added inertia I', added damping c' and added stiffness k' [20]. The expression of the torque is then

$$T(t) = T_0 + \tilde{T}(t) = T_0 + I'\frac{d^2\theta}{dt^2} + c'\frac{d\theta}{dt} + k'\theta. \tag{2.24}$$

With the assumed basic oscillation (equation 2.18), the expression of the torque oscillation $\tilde{T}$ becomes

$$\tilde{T}(t) = -I'\hat{\theta}\omega^2\sin(\omega t) + c'\hat{\theta}\omega\cos(\omega t) + k'\hat{\theta}\sin(\omega t). \tag{2.25}$$

As any of these coefficients can be positive or negative, it is impossible to distinguish experimentally between added inertia and added stiffness [20]. Therefore, only the components in phase and out of phase are distinguished:

$$\tilde{T}(t) = (k' - I'\omega^2)\hat{\theta}\sin(\omega t) + c'\hat{\theta}\omega\sin(\omega t + \frac{\pi}{2}) = C_i\sin(\omega t) + C_o\sin(\omega t + \frac{\pi}{2}) \tag{2.26}$$

where the coefficients of forces in phase and out of phase are respectively

$$C_i = (k' - I'\omega^2)\hat{\theta} \tag{2.27}$$

and

$$C_o = c'\hat{\theta}\omega. \tag{2.28}$$

This approach includes various simplifications and hypotheses. All components of the turbine are assumed to be completely rigid, dynamic phenomena such as deformation of the runner blades are not modelled. Furthermore, the water is considered incompressible, while in practice hydroacoustic effects and the whole hydraulic installation can influence the behaviour of the turbine [2, 21]. A more detailed investigation of runner oscillations should also include interaction with the power grid, which needs knowledge of the generator as well as the inertial and mechanical properties of the turbine [22].

2.5 Calculation of turbulence inlet conditions

Inlet boundary conditions for the turbulent quantities are calculated using the equations proposed by Gyllenram and Nilsson [23]. The turbulent kinetic energy k at the inlet is

$$k = \frac{3}{2}(C \cdot I)^2, \tag{2.29}$$

where I is the turbulence intensity, for which a value of $I = 10\%$ was chosen. The characteristic velocity C is calculated from the discharge Q and the inlet cross-section A_I as

$$C = \frac{Q}{A_I}. \tag{2.30}$$

Using a typical value of the ratio between eddy viscosity and fluid viscosity $\frac{\nu_t}{\nu} = 10$ and the relation

$$\nu_t = C_\mu \frac{k^2}{\varepsilon\nu}, \tag{2.31}$$

the boundary condition for the turbulent dissipation rate ε can be calculated as

$$\varepsilon = C_\mu \cdot \frac{k^2}{10\nu}. \tag{2.32}$$

Similarly, the specific rate of dissipation ω is calculated by

$$\nu_t = \frac{k}{\omega}, \tag{2.33}$$

leading to the final result

$$\omega = \frac{k}{10 \cdot \nu}. \tag{2.34}$$

3 Method and tools

In order to investigate the performance of the turbine at the given operating conditions, two types of simulations are conducted, which use different methods to treat the runner rotation. For steady-state RANS simulations assuming axi-periodic geometry, a mixing plane interface is used which computes a circumferential average of the physical quantities at the interface between the moving and stationary parts. For unsteady simulations of the entire turbine geometry, a moving mesh with a general grid interface (GGI) is used, allowing a more realistic modelling of wake propagation and rotor-stator interaction. The frozen rotor approach is not considered, as it represents wakes in an unphysical way, and with the mixing plane a better alternative for simplified and computationally cheap simulations is available [10].

3.1 Software

The open-source CFD code OpenFOAM is used for all the simulations in the scope of the present work. It has the advantage that the source code is fully accessible for the user, allowing personal modifications and developments, while its capabilities are comparable to commercial codes [9]. Several different development paths of OpenFOAM exist. In the present work, foam-extend-3.0-turbo is used, which is based on foam-extend-3.0 and has been adapted at Hydro Québec for turbomachinery applications. In this version, an improved version of the mixing plane is implemented, where issues of previous versions have been sorted out [1].

3.2 Steady-state mixing plane simulations

For the steady-state simulations, the computational domain is simplified by assuming axi-periodic flow. Therefore only one blade passage and one guide-vane passage need to be modelled. In addition, the spiral casing and the stay vanes are not simulated, and a boundary condition is set at the guide vane inlet instead (see Section 3.2.1). The geometry resulting from these simplifications is presented in Figure 3.1. As it will be shown in Section 3.5, a substantial reduction of the mesh size can be achieved without affecting the mesh quality. A further simplification is that the runner mesh remains stationary, and multiple rotating frames of reference (MRF, see Section 3.2.2) are used for the stationary and moving parts in order to mimic the behaviour of a rotating runner. Due to the sudden change of frames of reference, the wakes of the blades are not transported correctly through the interface between the rotating and the stationary zone [10]. The handling of the interface is therefore of crucial importance, and in the present case a mixing plane approach is chosen. The mixing plane interface is described in more detail in Section 3.2.3.

3.2.1 Set-up and boundary conditions

The inlet boundary is located just before the guide vanes, where the constant radial and tangential velocity components are specified from the flow rate and the trailing edge stay vane angle respectively. For the turbulent quantities, the inlet boundaries are computed using the equations presented in Section 2.5. The resulting values for the different operating points are summed up in Table 3.1. As only one guide-vane and blade passage is modelled, a periodic boundary condition is applied on the patches in the fluid region between the blade passages. A cyclic GGI is used both at the leading and trailing edges of the guide-vanes, which allows the use of non-conformal meshes at the periodic boundary. The cyclic GGI is based on the standard GGI (see Section 3.3.2), but adapted to create a periodic boundary condition between two patches which are not at the same location [24]. The inlet and outlet boundary conditions for all physical quantities are summed up in Table 3.2.

3.2.2 MRF solver

In order to model the behaviour of the rotating runner, a solver which uses multiple rotating frames of reference (MRF) is employed. The different mesh regions are not physically rotating, but for each of the rotating and stationary regions, a separate reference frame is defined and a rotational velocity can be specified. The resulting Coriolis and centrifugal forces are then added to the Navier-Stokes equations. A description of the MRF solver is given by Petit *et al.* [25].

[1] Martin Beaudoin, personal communication, April 2014

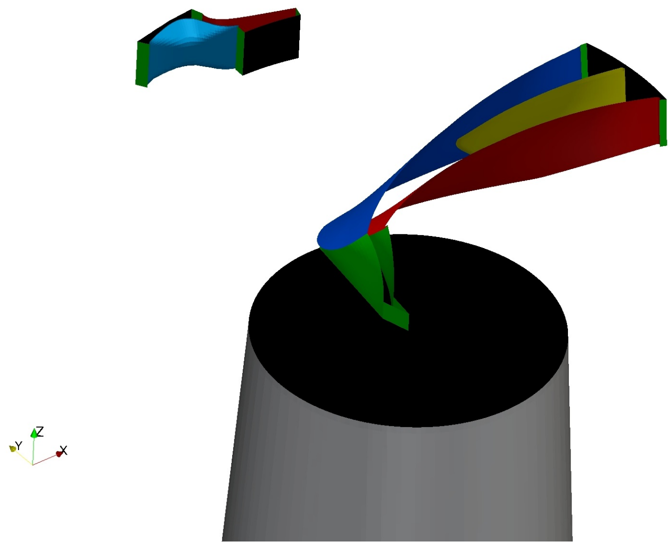

Figure 3.1: *Computational domain for the mixing plane simulations with one guide vane passage, one runner blade passage and the draft tube. Note that the entire draft tube is included in the simulations, but only a partial view is shown here.*

Operating point	C_R $[m/s]$	C_θ $[m/s]$	k $[m^2/s^2]$	ε $[m^2/s^3]$	ω $[1/s]$
Best efficiency point - original	-1.428	-2.142	0.099	92.94	10387.90
Best efficiency point - new	-1.477	-2.216	0.106	106.44	11116.66
Part load	-0.500	-0.749	0.012	1.39	1270.73
High load - original	-1.555	-2.332	0.118	130.56	12311.77
High load - new	-1.618	-2.427	0.128	153.16	13334.95

Table 3.1: Inlet velocity boundary conditions for steady-state simulations at the original and additional operating points.

3.2.3 Mixing plane interface

The mixing plane interface is used to compute a circumferential average of all quantities, thus eliminating the wakes rather than representing them in an unphysical way. This procedure was already proposed by Denton [26], and similar techniques have been applied by Brandvik *et al.* [27] as well as by Pascoa *et al.* [28] on compressible flows in gas turbines. The OpenFOAM implementation was developed by Beaudoin and Jasak [24], and validated by Page *et al.* [12]. The circumferential average is computed by discretising the two patches into bands or "ribbons". A coordinate system is defined in order to chose the directions of discretisation and averaging, which in the present case is cylindrical and oriented along the runner axis. While for the cylindrical runner inlet surface the discretisation is done along the z axis, the circular runner outlet is discretised in the radial direction. In both cases, the averaging is done in the tangential direction, leading to the desired circumferential average. Several different schemes are available in OpenFOAM to link the physical quantities on both sides of the interface. The basic "areaAveraging" scheme is based solely on a geometrical averaging. With a more recent scheme for the velocity field ("fluxAveragingAdjustMassFlow"), the values are weighted by the mass flux across the faces. The velocity field is then adjusted in order to maintain a continuous mass flux through the interface, which is otherwise not guaranteed due to the averaging process. The scheme for pressure is "zeroGradientAreaAveragingMix", which consists of a zero-gradient boundary condition on each side of the patch. The pressure fields on either side of the interface are then coupled by fixing the same mean value for both patches. For all other quantities, the default "areaAveraging" scheme is used. A detailed description of the mixing plane implementation in OpenFOAM is given by Page *et al.* [12].

Field	Inlet boundary condition	Outlet boundary condition
C	Fixed value (see Table 3.1)	Zero gradient
p	Zero gradient	Fixed value (0 Pa)
k	Fixed value (see Table 3.1)	Zero gradient
ε	Fixed value (see Table 3.1)	Zero gradient
ω	Fixed value (see Table 3.1)	Zero gradient

Table 3.2: Boundary conditions for steady-state simulations.

3.2.4 Numerical method

The solver uses the SIMPLE algorithm for pressure-velocity coupling. For all variables, a stabilised bi-conjugate gradient method (BiCGStab) is used. The preconditioner is the diagonal incomplete LU decomposition. A tolerance of 10^{-5} on the residuals is used for all variables, except for the pressure where a stricter tolerance (10^{-6}) is applied. The solver settings are summed up in Table 3.3, while the relaxation factors are listed in Table 3.4. The number of non-orthogonal correctors for the SIMPLE algorithm is fixed at 2. For the discretisation of the convection term, a second order linear upwind scheme is used [29]. The flow field is initialised with a potential flow solver to accelerate convergence.

Variable	Solver	Preconditioner	Absolute tolerance	Relative tolerance
p	BiCGStab	DILU	10^{-6}	0.01
U	BiCGStab	DILU	10^{-5}	0.1
k	BiCGStab	DILU	10^{-5}	0.1
ε	BiCGStab	DILU	10^{-5}	0.1
ω	BiCGStab	DILU	10^{-5}	0.1

Table 3.3: Solver settings for steady-state simulations. The absolute tolerance limits the magnitude of the residuals, while the relative tolerance defines the ratio between the initial and the final residual.

Variable	Relaxation factor
p	0.3
U	0.7
k	0.7
ε	0.7
ω	0.7

Table 3.4: Relaxation factors for steady-state simulations.

3.3 Unsteady simulations with constant rotational speed

The computational domain for the URANS simulations consists of the entire turbine geometry, including the spiral casing with the stay-vane passage and the complete runner (see Figure 2.1). As the runner mesh is physically rotating, a general grid interface (see Section 3.3.2) is placed between the stationary and rotating regions, allowing the combination of non-conformal meshes at the interface.

3.3.1 Set-up and boundary conditions

As the entire spiral casing is modelled for the unsteady simulations, a fixed flow rate is applied at the inlet, while the condition on pressure is zero gradient. The draft tube outlet boundary condition is a uniform fixed pressure with zero velocity gradient. The boundary conditions for all variables are shown in Table 3.5. Inlet boundary conditions for turbulent quantities are calculated using the equations presented in Section 2.5. Table 3.6 shows the values for all three operating points.

Field	Inlet boundary condition	Outlet boundary condition
C	Fixed flow rate	Zero gradient
p	Zero gradient	Fixed value (0 Pa)
k	Fixed value (see Table 3.6)	Zero gradient
ε	Fixed value (see Table 3.6)	Zero gradient
ω	Fixed value (see Table 3.6)	Zero gradient

Table 3.5: Boundary conditions for unsteady simulations.

Operating point	k	ε	ω
Best Efficiency Point $[m/s]$	0.0812	62.029	8486.32
Part load $[m/s]$	0.0099	0.928	10058.01
High load $[m/s]$	0.0963	87.132	1038.11

Table 3.6: Turbulent inlet boundary conditions for unsteady simulations.

3.3.2 General grid interface interface (GGI)

The interface between the stationary and rotating parts is treated using a general grid interface. The values on the boundary patch are interpolated and then transmitted to the neighbouring patch. This allows to use non-conformal meshes at the interface, which simplifies the mesh generation process and allows to choose the time step freely. However, some care must be taken during the mesh generation around the interface as large differences in the flow-wise grid size around the GGI can cause distortions of the solution and form a numerical obstacle for the flow. A detailed description of the algorithm used for the GGI in OpenFOAM is given by Beaudoin and Jasak [24].

3.3.3 Numerical method

For the unsteady simulations, a solver is employed which uses the SIMPLE algorithm for pressure-velocity coupling and is adapted for transient simulations with dynamic mesh motion. A conjugate gradient solver with a diagonal incomplete Cholesky preconditioner is used for pressure. All the other variables are solved with a bi-conjugate gradient method and a diagonal incomplete LU preconditioner. The tolerance on the residuals is set to 10^{-5} for all variables. Table 3.7 shows an overview of the solver settings that are used, and Table 3.8 shows the relaxation factors. A second-order linear upwind scheme [29] is used for the discretisation of the convection term. The number of correctors is fixed at 1, while the number of non-orthogonal correctors is 2 and the number of outer correctors is 4. This means that after every time the velocity is solved, the pressure is solved 3 times, and this procedure is repeated 4 times for every time step. Flow rate and rotational speed are ramped up, and the simulations are then run for three complete runner rotations. After that, the scheme for the convection term are changed from upwind to linear upwind, the relaxation factors increased to their final values and the simulations run for another 2 complete runner rotations. The time step is chosen in order to obtain a runner rotation of 0.25° per time step.

Field	Solver	Preconditioner	Absolute tolerance	Relative tolerance
p	PCG	DIC	10^{-5}	0.002
U	PBiCG	DILU	10^{-5}	0.1
k	PBiCG	DILU	10^{-5}	0.1
ε	PBiCG	DILU	10^{-5}	0.1

Table 3.7: Solver settings for unsteady simulations. The absolute tolerance limits the magnitude of the residuals, while the relative tolerance defines the ratio between the initial and the final residual.

3.4 Unsteady simulations with variations in rotational speed

For the unsteady simulations with oscillations of the rotational speed, the case set-up, the mesh and the numerical methods are identical to the unsteady simulations with constant rotational speed. In order to obtain

Variable	Relaxation factor
p	0.3
U	0.7
k	0.7
ε	0.7
ω	0.7

Table 3.8: Relaxation factors for unsteady simulations.

a good resolution of the torque and pressure fluctuations, the time step is chosen to be $\Delta t = \frac{1}{50}T_{osc}$, where T_{osc} is the oscillation frequency of the runner. The oscillation frequency of the runner is chosen based on the results from unsteady simulations with constant rotational speed (see Section 4.3.1).

3.5 Mesh generation

The mesh generation is done in ANSYS ICEM. Each component of the turbine is meshed separately, the resulting mesh exported and then assembled in OpenFOAM. The original hexahedral block-structured mesh is supplied by the workshop committee. Quality improvements are made, and separate meshes are created for the steady and unsteady simulations. The original mesh is described in Appendix C.1.

3.5.1 Mesh for mixing plane simulations

As only one blade passage is used for the mixing plane simulations, the number of cells is lower than for the original mesh. Because the original O-grid in the region below the hub cannot be split to cover only one blade passage, it is replaced by a radial mesh that goes from the trailing edges of the blades to the axis of rotation (see Figure 3.2). This kind of mesh is not optimal as the cells near the axis of rotation have a very unfavourable aspect ratio, but it is the simplest way to mesh this region. The number of cells for all 3 operating points is shown in Table 3.9.

Part	Number of cells		
	BEP	High load	Part load
Guide vane passage	25143	25491	22939
Runner	351860	335218	
Draft tube	3570944		
Total	3947947	3931653	3929101

Table 3.9: Number of cells in the mixing plane mesh.

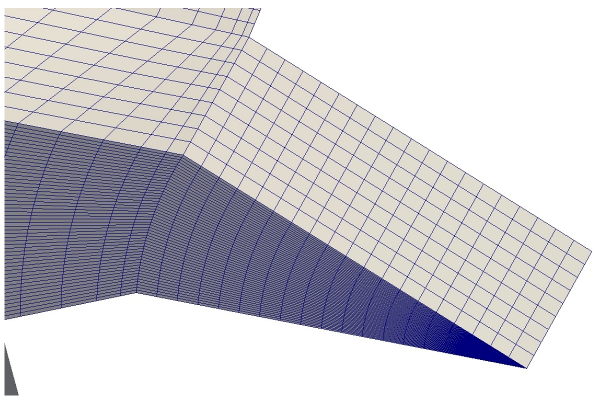

Figure 3.2: *Radial mesh near the rotation axis at the runner outlet.*

The quality of the mesh is assessed for each operating point using the available utilities for this purpose in OpenFOAM. At best efficiency point, a refined mesh is used for the runner and guide vane passage, while for

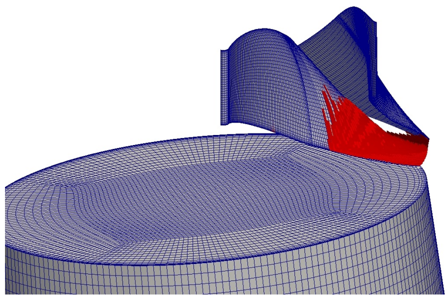

(a) *Severely non-orthogonal faces in the runner mesh.*

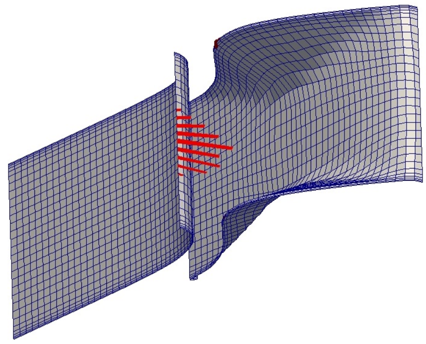

(b) *Severely non-orthogonal faces in the guide vane passage of the mesh for best efficiency point.*

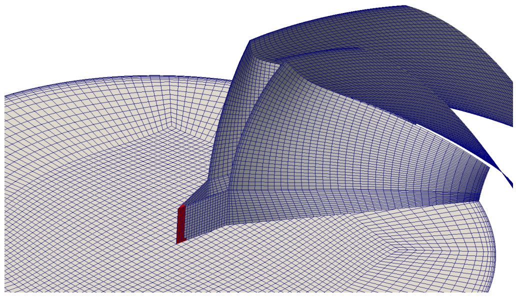

(c) *Underdetermined cells in the runner mesh in the radial mesh near the axis of rotation.*

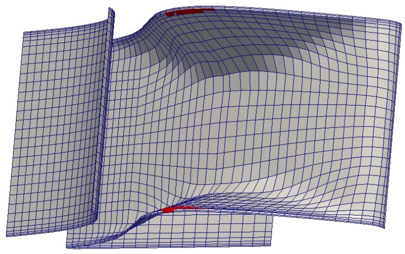

(d) *Severely non-orthogonal faces in the guide vane passage of the mesh for high load.*

Figure 3.3: *Quality issues in the mesh for steady-state mixing plane simulations.*

the other operating points no refinement is done. Detailed information about the refinement and a comparison between the original and refined mesh are given in Appendix C.2. Of a total of 3947947 cells and 11936731 faces in the mesh for best efficiency point, 18775 faces are severely non-orthogonal, which means that their non-orthogonality is above the defined threshold of 70. With an average non-orthogonality of 15.59 and the maximum being at 80.38, this is however no reason for concern. The problematic faces are shown in figures 3.3a and 3.3b. All of the non-orthogonal faces are situated near the pressure side of the runner blade and in the guide vane passage. In addition, 2227 cells with a small determinant are detected, which are all located below the hub near the axis of rotation where a radial mesh is used (see Figure 3.3c). This problem should be avoided in future simulations by using a modified topology similar to the one used for unsteady simulations (see Section 3.5.2). The mesh for part load has 3929101 cells and 11879634 faces, and does not contain any severely non-orthogonal faces in the guide vane passage. The total number of non-orthogonal faces is therefore lower with 8387. The high load mesh with 3931653 cells and 11887436 faces contains a small number of non-orthogonal faces in the distributor (Figure 3.3d) with an identical runner mesh, and the resulting total number is 8468.

3.5.2 Mesh for unsteady simulations

The mesh for unsteady simulations consist also of three separate part: the spiral casing including the distributor, the runner, and the draft tube. For the spiral casing and distributor, the mesh supplied by the workshop organisers remains unchanged. To obtain the runner mesh, only one blade passage is used for the mesh generation. Minor modifications are made in the region near the blade surface to reduce the number of skewed cells and at the runner inlet (see Appendix C.1), but the topology remains unchanged. The optimised Section is then copied and rotated periodically in order to obtain the full 360° runner mesh.

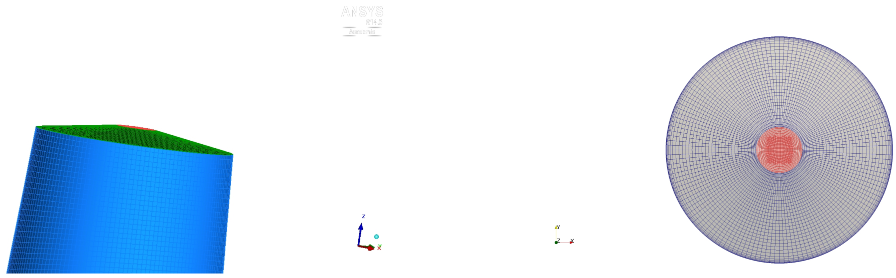

(a) *Modified draft tube inlet geometry for unsteady simulations.*

(b) *Modified draft tube inlet mesh for unsteady simulations.*

Figure 3.4: *Modified draft tube inlet topology for unsteady simulations.*

Part	Number of cells		
	BEP	High load	Part load
Spiral casing	3438563	3581240	3441063
Runner	4598970		
Draft tube	4177152		
Total	12214685	12357362	12709257

Table 3.10: Number of cells in the mesh for unsteady simulations.

Topology modification

To obtain a good mesh quality below the hub, the topology near the runner outlet is modified. The flat circular runner outlet and draft tube inlet are replaced with conical surfaces which connect the circular edges of the shroud and the hub (Figure 3.4a). In the draft tube mesh, an additional O-grid is added in the centre over the whole length of the draft tube (Figure 3.4b). A detailed view of the new O-grid is shown in Figure 3.5. With this modified topology, issues in mesh quality between the hub and the runner outlet are avoided. The resulting number of cells in the mesh for each operating point is shown in Table 3.10.

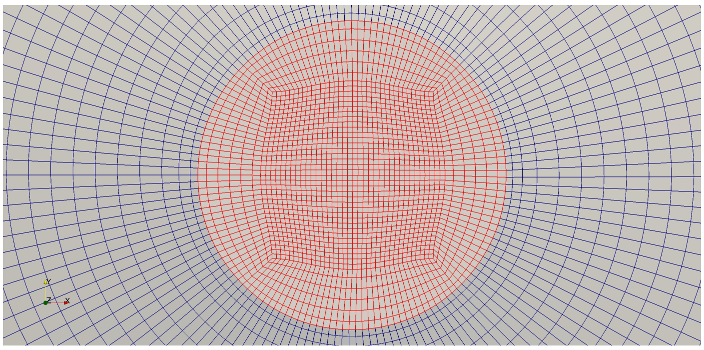

Figure 3.5: *Detailed view of the modified draft tube inlet mesh for unsteady simulations.*

Mesh quality

Several quality issues are present in the spiral casing mesh that was supplied by the workshop organisers. In Figure 3.6a, the mesh in the guide-vane and stay vane passage is shown.Very coarse regions are located near the leading edges of the stay vanes and in the stay vane passage. Furthermore, a thin line with very fine resolution in the flow direction is present originating at the leading edge of each stay vane. This comes from the refined boundary layer mesh which is used near the wall, and then crosses the entire domain due to the structure of the blocking. These strong jumps in flow-wise resolution can lead to numerical instability and bad convergence behaviour, and should therefore be avoided wherever possible. On the other hand, the mesh on the surfaces near the trailing edge of the stay vanes is not refined. Correcting these issues would need large modifications of the blocking topology and would go beyond the scope of this thesis. In an eventual continuation of the work,

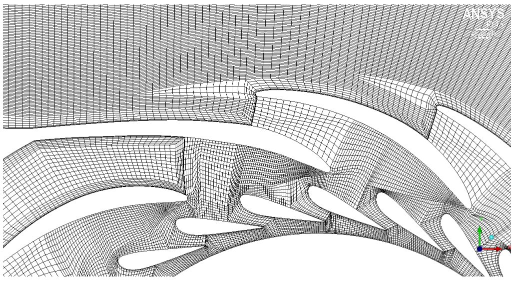

(a) *Detailed view of the mesh in the spiral casing and stay vane cascade.*

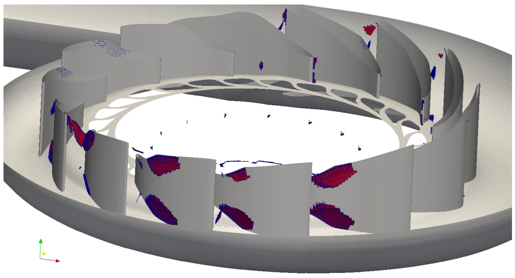

(b) *Severely non-orthogonal faces in the spiral casing and stay vane cascade in the mesh for unsteady simulations at best efficiency point.*

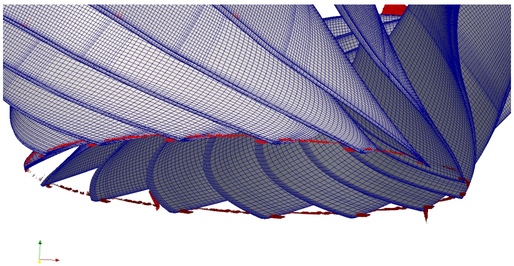

(c) *Severely non-orthogonal faces around the trailing edges of the blades and the runner outlet in the mesh for unsteady simulations.*

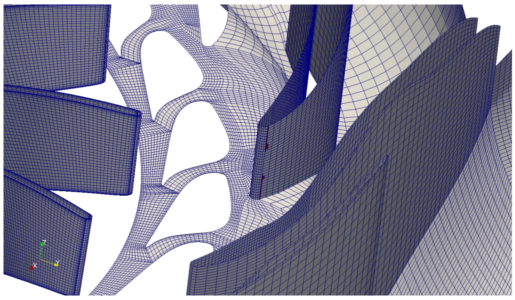

(d) *Skewed cells at the trailing edge of the stay vanes in the mesh for unsteady simulations at best efficiency point.*

Figure 3.6: *Quality issues in the mesh for unsteady simulations.*

these issues should however be taken into account, ideally by re-meshing the spiral casing completely. The overall quality of the full 3D mesh for unsteady simulations was also assessed using the built-in OpenFOAM utilities. For a total of 12214685 cells and 37130853 faces, 11729 severely non-orthogonal faces are detected. The maximum non-orthogonality is at 79.81, while the average is at 23.99. Figure 3.6b shows the location of the severely non-orthogonal faces in the spiral casing and the stay vane passage. Most of the cells are located on the surface of the stay vanes. In the runner mesh (Figure 3.6c), the problematic cells are located between the trailing edges of the blades and the runner outlet. The number of skewed cells is 31 with a maximum skewness of 4.357, the threshold being at 4. These cells are mainly located at the trailing edge of the last stay vane, as it is shown in Figure 3.6d. The mesh for part load has 12709257 cells and 37138801 faces. 8497 of these faces are above the threshold for non-orthogonality, with the maximum being at 81.16 and the average at 23.91. Furthermore, the mesh contains also 37 highly skewed cells with a maximum skewness of 4.18, which is lower than for best efficiency point. For high load operation, the mesh consists of 12357362 cells with 37563638 faces. The number of severely non-orthogonal faces is only 9055, with a maximum of 79.10 and an average non-orthogonality of 24.02. There are also 37 highly skewed cells, and the maximum skewness is identical to part load with 4.18. The problematic cells in the part load and high load meshes are located in the same areas as in the mesh for best efficiency point. Despite the mentioned issues, the overall quality of the mesh appears to be sufficient to obtain the desired results. Correcting the current issues would require a considerable effort and ideally a complete re-meshing of the entire geometry. As the main focus of the present work is on turbulence models and the simulation methodology rather than mesh optimisation, no further modifications are made.

3.6 Turbulence modelling

Due to the expected swirling flow at the runner outlet at off-design operation, accurate turbulence modelling is of great importance if the flow field and the performance of the turbine are to be predicted accurately. This unsteady flow can not be modelled completely by steady-state simulations, but appropriate turbulence models could allow a good prediction of the mean flow and the losses in this crucial region. In order to explore the possibilities in this area, several different turbulence models are used. In addition to the common two-equation models which are already implemented in OpenFOAM and have been validated extensively (e.g. by Petit [10], by Petit *et al.* [13] and by Nilsson [9, 18]), more advanced alternatives are considered and implemented. Two new models are implemented and tested, in order to compare their performance with the existing models. While the linear explicit algebraic Reynolds stress model is used for steady-state simulations, the k-ω SSTF is employed for unsteady simulations. In Appendix E, the values of the coefficients for all turbulence models are listed.

3.6.1 Classical two-equation models

For the mixing plane simulations, the models that are used are the standard $k-\varepsilon$, RNG $k-\varepsilon$, Realizable $k-\varepsilon$ and $k-\omega$ SST. For the unsteady simulations, the standard $k-\varepsilon$ model is chosen. As boundary conditions at the wall, standard ν_t-wall functions for high-Reynolds number models are used for all models. For future simulations with an optimised and more refined mesh, the use of more advanced methods for the modelling of the near-wall region should be examined.

3.6.2 Explicit algebraic Reynolds stress model (EARSM)

As an alternative to classical eddy-viscosity models, a linear explicit algebraic Reynolds stress model (EARSM) proposed by Wallin ([30], paper 6) is implemented and tested. Wallin and Johansson [31] validated the model and found better agreement for rotating flows than with classical eddy-viscosity models, which makes it interesting for turbomachinery applications. Good performance of the model with rotating flows in pipes suggests that it should perform well in modelling swirling flow in the draft tube, especially at off-design conditions. Wallin proposes three different versions of his model, with different levels of complexity. In the following presentation Wallin's formulation is closely followed, with some adaptations for the incompressible case. The linear EARSM is implemented on the basis of the standard k-ω model available in OpenFOAM. It is identical to the k-ω model, with the exception that the eddy viscosity is calculated in a different manner, but the anisotropy of the Reynolds stress tensor is not considered. In the original k-ω model, the eddy viscosity is simply given by

$$\nu_t = \frac{k}{\omega}. \tag{3.1}$$

In the EARSM, first of all the non-dimensional tensors S and Ω need to be defined, which are given by

$$S_{ij} = \tau S^*_{ij} \tag{3.2}$$

and

$$\Omega_{ij} = \tau \Omega^*_{ij} \tag{3.3}$$

respectively. The dimensional tensors S^* and Ω^* are

$$S^*_{ij} = \frac{1}{2}(\frac{\partial U_i}{\partial x_j} + \frac{\partial U_j}{\partial x_i}) \tag{3.4}$$

and

$$\Omega^*_{ij} = \frac{1}{2}(\frac{\partial U_i}{\partial x_j} - \frac{\partial U_j}{\partial x_i}). \tag{3.5}$$

Note that this simplified expression for the tensor $\mathbf{S}$ is only valid for incompressible flow, and differs therefore from the definition in Wallin's thesis. τ is the turbulent time scale, which is limited by the Kolmogorov time scale as

$$\tau = max(\frac{k}{\varepsilon}, C_\tau \sqrt{\frac{\nu}{\varepsilon}}). \tag{3.6}$$

The two tensors have the invariants

$$\mathbf{II}_S = tr\mathbf{S}^2, \tag{3.7}$$

$$\mathbf{II}_\Omega = tr\mathbf{\Omega}^2 \tag{3.8}$$

and

$$\mathbf{IV} = tr\mathbf{S\Omega}^2. \tag{3.9}$$

With these invariants, two coefficients can be calculated:

$$P_1 = (\frac{C_1'^2}{27} + \frac{9}{20}\mathbf{II}_S - \frac{2}{3}\mathbf{II}_\Omega)C_1' \tag{3.10}$$

$$P_2 = P_1^2 - (\frac{C_1'^2}{9} + \frac{9}{10}\mathbf{II}_S + \frac{2}{3}\mathbf{II}_\Omega)^3. \tag{3.11}$$

These two coefficients allow us to calculate N as

$$N = \begin{cases} \frac{C_1'}{3} + (P_1 + \sqrt{P_2})^{1/3} + (P_1 - \sqrt{P_2})^{1/3} & P_2 \geq 0 \\ \frac{C_1'}{3} + 2(P_1^2 - P_2)^{1/6}\cos(\frac{1}{3}\arccos(\frac{P_1}{\sqrt{P_1^2 - P_2}})) & P_2 < 0 \end{cases}. \tag{3.12}$$

Using N, the common denominator Q is expressed as follows:

$$Q = \frac{5}{6}(N^2 - 2\mathbf{II}_\Omega)(2N^2 - \mathbf{II}_\Omega) \tag{3.13}$$

which in turn is used to calculate the β - coefficients:

$$\beta_1 = -\frac{N(2N^2 - 7\mathbf{II}_\Omega)}{Q} \tag{3.14}$$

$$\beta_3 = -\frac{12N^{-1} - \mathbf{IV}}{Q} \tag{3.15}$$

$$\beta_4 = -\frac{2(N^2 - 2\mathbf{II}_\Omega)}{Q} \tag{3.16}$$

$$\beta_6 = -\frac{6N}{Q} \tag{3.17}$$

$$\beta_9 = \frac{6}{Q} \tag{3.18}$$

Finally, the new eddy viscosity can be calculated using these coefficients as

$$\nu_t = -\frac{1}{2}(\beta_1 + \mathbf{II}_\Omega\beta_6)k\tau. \tag{3.19}$$

Note that contrary to the model constants which are commonly used in other turbulence models, the β-coefficients are scalar fields which depend on the velocity field. Therefore they need to be recalculated at every iteration for every location in the flow field. As proposed by Wallin, the values for the model constants are $C_\tau = 6.0$ and $C_1' = 1.8$. If only these modifications are included, the linear EARSM is obtained, which is actually an eddy viscosity model. For the complete EARSM, an additional term must be added to the Reynolds stress tensor, which then becomes

$$R_{ij} = \overline{u_i u_j} = \frac{2}{3}k\delta_{ij} - 2\nu_t S_{ij}^* + k a_{ij}^{(ex)}. \tag{3.20}$$

The extra anisotropy $a_{ij}^{(ex)}$ is calculated as

$$a_{ij}^{(ex)} = \beta_3(\mathbf{\Omega}^2 - \frac{1}{3}\mathbf{II}_\Omega\mathbf{I}) + \beta_4(\mathbf{S\Omega} - \mathbf{\Omega S}) + \beta_6(\mathbf{S\Omega}^2 + \mathbf{\Omega}^2\mathbf{S} - \mathbf{II}_\Omega\mathbf{S} - \frac{2}{3}\mathbf{IV}\ \mathbf{I}) + \beta_9(\mathbf{\Omega S\Omega}^2 - \mathbf{\Omega}^2\mathbf{S\Omega}). \tag{3.21}$$

The additional term creates some difficulties regarding the implementation of the complete EARSM model in OpenFOAM. The Reynolds stress tensor is no longer symmetric, which means that the solvers need to be modified in order to allow a non-symmetric tensor. This complication is acceptable for personal use of the model, but should be avoided on the long term as it would mean that particular solvers can only be used with a specific type of turbulence model. Due to the limited time and complex implementation, the complete EARSM is not fully implemented and thus not used for simulations in the scope of the present work.

3.6.3 k-ω SSTF

The k-ω SSTF model is a modified version of the k-ω SST model, where a filter is applied to the modelled length scales and the turbulent viscosity is calculated differently. This model has been validated on the Dellenback abrupt expansion test case by Gyllenram and Nilsson [32]. In the present work it is used for unsteady sliding-grid simulations as an alternative to the standard k-ε model, as it is thought to resolve more accurately the unsteady features of the flow field. The implementation in OpenFOAM has been described by Nilsson [33]. In the original k-ω SST model, the eddy viscosity is given by

$$\nu_t = \frac{a_1 \cdot k}{max(a_1 \cdot \omega, F_2 \cdot \sqrt{2} \cdot \|\mathbf{S}^*\|)}. \tag{3.22}$$

In the k-ω SSTF model, the modelled length scale L_t is calculated first as

$$L_t = \frac{\sqrt{k}}{\beta^* \omega}, \tag{3.23}$$

as well as its upper limit l_t which is given by

$$l_t = \alpha \cdot max((\Delta)^{1/3}, \|\overrightarrow{U}\|\Delta t), \tag{3.24}$$

where Δt is the time step and Δ the local mesh spacing. The turbulent viscosity is then calculated as

$$\nu_t = min((\frac{l_t}{L_t})^{4/3}, 1) \cdot (\frac{a_1 \cdot k}{max(a_1 \cdot \omega, F_2 \cdot \sqrt{2})}). \tag{3.25}$$

The blending function F_2 is identical to the k-ω SST model and is therefore not discussed any further.

3.7 Computational resources and decomposition

The simulations are performed on a cluster of 268 nodes which consist each of 8 Xeon E5520 2.72GHz processors. Mixing plane simulations are performed using 8 to 32 cores, while the unsteady simulations are run on 128 cores. In order to run the simulations in parallel, the domain is decomposed in OpenFOAM using the "metis" algorithm.

3.8 Analysis of the results

Wherever possible, built-in functionalities of OpenFOAM are used for the post-processing. The vortices and coherent structures are identified using the vorticity and the second invariant of the velocity gradient (q-criterion defined by Hunt *et al.* [34]), which are both obtained directly in OpenFOAM. The results are visualised using Paraview. In order to obtain velocity profiles and pressure evolution at specific points (Section 3.8.2), sampling utilities in OpenFOAM are used and the resulting data is processed and plotted with Matlab.

3.8.1 Efficiency calculation

The turbine efficiency is calculated using the "turboPerformance" function object in OpenFOAM. In the source code, the efficiency is defined as

$$\eta = \frac{P}{P_{fluid}}, \tag{3.26}$$

where P is the mechanical power at the shaft given by

$$P = T \cdot \omega \tag{3.27}$$

and P_{fluid} is the available fluid power, which is numerically calculated by summing over all faces i and j on the inlet and outlet patches, yielding the expression

$$P_{fluid} = \rho\left(\sum_{i=1}^{n_{faces}} Q_i \cdot p_{0,I,i} - \sum_{j=1}^{n_{faces}} Q_j \cdot p_{0,\bar{I},j}\right). \tag{3.28}$$

The total pressure p_0 is defined as

$$p_{0,i} = \frac{p_i}{\rho} + \frac{C_i^2}{2}. \tag{3.29}$$

Therefore we have

$$P_{fluid} = \rho(Q \cdot p_{0,I} - Q \cdot p_{0,\bar{I}}) = \rho \cdot Q \cdot \Delta p_0. \tag{3.30}$$

The calculated efficiency is then

$$\eta = \frac{T \cdot \omega}{\rho \cdot Q \cdot \Delta p_0}. \tag{3.31}$$

This definition of the efficiency does not take into account the gravitational term in the IEC definition of the available specific energy (equations 2.1 and 2.2), and corresponds thus to the definition given by the Francis-99 committee (equation 2.11). In order to increase the generality of the results and comply with the IEC standards, the gravitational term is added separately to the available specific energy. The additional fluid power term $P_{g\Delta z}$ is calculated as

$$P_{g\Delta z} = \rho \cdot Q \cdot g(z_I - z_{\bar{I}}). \tag{3.32}$$

With a gravitational acceleration $g = 9.821 m/s^2$ [8] and a difference in elevation of $\Delta z = 0.6428m$ between the inlet and outlet section, the resulting potential energy terms for each operating point are summed up in Table 3.11. Note that for the elevation z of the inlet and outlet section, the mean values of the sections are used.

Operating point	$P_{g\Delta z}[W]$
Best Efficiency Point - original	1280.52
Best Efficiency Point - new	1324.68
Part load	447.89
High load - original	1394.08
High load - new	1450.85

Table 3.11: Potential energy term at each of the three original and two additional operating points.

3.8.2 Comparison with experimental data

The obtained results are compared with the experimental measurements and simulated results which are available for the Francis-99 turbine. Data published by Trivedi *et al.* [7] is reconstructed from graphs in the paper. Comparing their time-averaged values to the mixing plane results is a good measure for the validity and accuracy of steady-state mixing plane simulations. As mentioned in Section 2.3, the operating conditions used for the experimental velocity measurements differ from the ones that were originally proposed. For the mixing plane simulations, the comparison with experimental data is therefore not done at the same operating conditions for velocity profiles (which are based on the modified operating points) and all the other quantities such as pressure distribution and efficiency (which are based on the original operating points). The remaining results for all operating conditions are however shown in Appendix A.

Pressure probes

The comparison of the results with experimental measurements is done using pressure probes which are placed at the locations of the pressure sensor in the model turbine (see Figure 3.7). The coordinates are shown in Table 3.12. As the probes are located in different blade and guide vane passages, not all locations are included in the computational domain of the mixing plane simulations. The probes located in the vane-less space and on the blades are therefore rotated to the corresponding position in the modelled blade and guide vane passage. As the reference pressure at the outlet in the simulations is $0kPa$, the simulated curves are shown with an offset equal to the outlet pressure of the experiment to allow a meaningful comparison of the different results. This offset is $p_{\bar{I}} = 101.562kPa$ for best efficiency point, $p_{\bar{I}} = 99.536kPa$ for part load and $p_{\bar{I}} = 95.977kPa$ for high load [8].

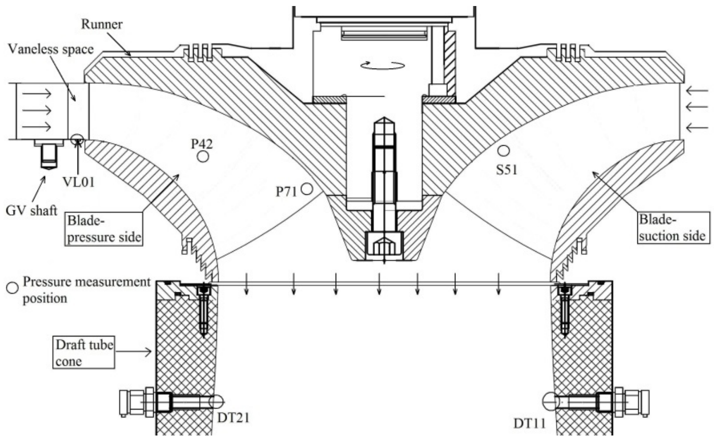

Figure 3.7: *Location of the pressure probes in the guide vane cascade, runner and draft tube (illustration taken from the workshop website [8] with kind permission of Prof. M.Cervantes).*

Sensor	VL01	P42	S51	P71	DT11	DT21
x [m]	0.2623	$7.16 \cdot 10^{-5}$	−0.0800	−0.0666	−0.0904	−0.0904
y [m]	0.1935	0.1794	0.0838	0.0423	0.1566	−0.1566
z [m]	−0.0296	−0.0529	−0.0509	−0.0860	−0.3058	−0.3058

Table 3.12: Location of the pressure probes in the turbine [8].

Velocity profiles

Velocity measurements were done using a laser Doppler anemometer (LDA) along two lines in the runner outlet cone[8]. In the simulated results, velocity profiles are created along the same lines. For unsteady simulations, the flow field is averaged over one runner revolution. The locations of the two lines are presented in Table 3.13 and drawn as black lines in the pressure contours in Chapter 4. All the velocity profiles are normalised by the reference radius R_{ref} and the circumferential velocity $U_{ref} = R_{ref} \cdot \omega$. Note that while pressure and efficiency measurements were available from the start of the work, velocity measurements were obtained only after the completion of the simulations.

Line	Line 1		Line 2	
	Start point	End point	Start point	End point
x [m]	−0.1789	0.1789	−0.1965	0.1965
y [m]	0	0	0	0
z [m]	−0.2434	−0.2434	−0.5614	−0.5614

Table 3.13: Location of the measurement lines used for velocity profiles [8].

4 Results and discussion

4.1 Steady-state mixing plane simulations

Mixing plane results are obtained at all three original operating points and at the two new operating points. At best efficiency point and at part load all turbulence models produce satisfying results, but at high load operation only the standard k-ε, RNG k-ε and Realizable k-ε produce a converged solution for both the original and the new operating point. The linear EARSM gives a converged solution at the new operating point while diverging at the original conditions, and the k-ω SST model diverges at both operating points. At best efficiency point, the recently developed more advanced mixing plane schemes are used (see Section 3.2.3 and Appendix D.2), while at off-design conditions the basic area-averaging scheme is chosen as it is more stable.

Figures 4.1 shows the hydraulic efficiency as defined by the workshop committee as a function of the discharge for all the turbulence models that are used, while Figure 4.2 shows the same data but with the efficiency as defined by the IEC. In Figure 4.1, the simulated efficiency values are compared to the experimental results as published by the workshop committee. The graph shows a considerable over-prediction of the efficiency for all operating points. Furthermore, large differences exist between the different turbulence models. Possible reasons for these differences and more details for each operating point are discussed in the following sections. While some quantitative differences occur depending on the turbulence model that is used, the general flow features remain qualitatively identical for all models. The qualitative analysis for each operating point is therefore done using the results for the standard k-ε model as a basis, before the quantitative differences between the models are discussed.

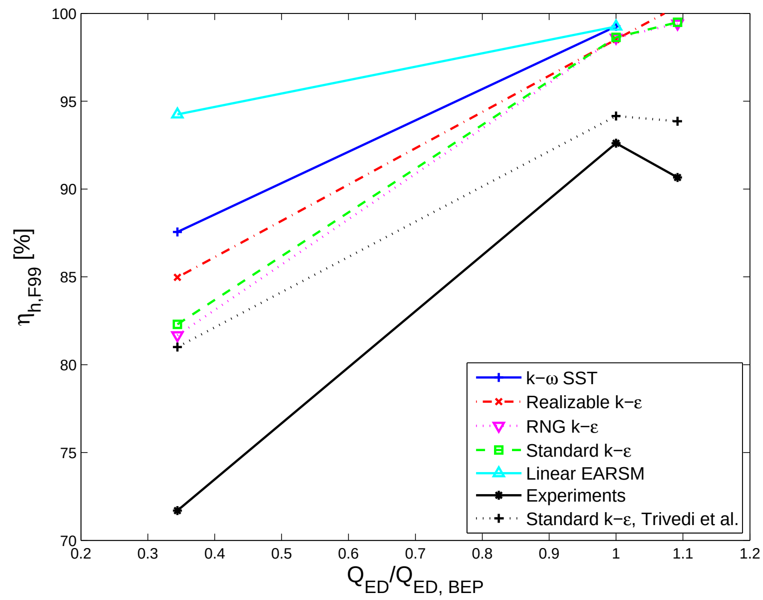

Figure 4.1: *Hydraulic efficiency (without the gravitational term) depending on the discharge for different turbulence models compared to the experimental values provided by the workshop committee [8] and unsteady simulations by Trivedi et al. [7].*

4.1.1 Best efficiency point

Overview and qualitative analysis

The best efficiency point simulations show the expected smooth flow pattern in the guide vane passage (Figure 4.3a). At the outlet, there is a confined zone on the rotation axis (see Figures 4.3b and 4.3c) below the hub with relatively strong counter-clockwise swirl (i.e. against the runner rotation) and low axial velocity (Figure 4.3d). This differs somewhat from the expected behaviour without swirl, and is usually present for high load operation only [35]. This swirling motion is also observed on the streamlines in the draft tube (Figure 4.4). The swirl

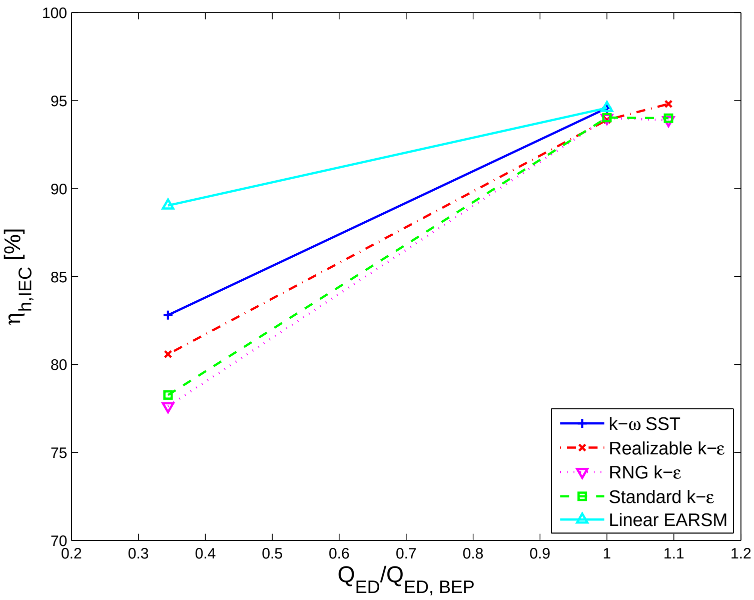

Figure 4.2: *Hydraulic efficiency as defined by the IEC standards depending on the discharge for different turbulence models.*

decreases constantly towards the draft tube wall, until it sharply increases in the opposite direction, meaning with the runner movement (Figure 4.3c). While the rotation gets dampened out as the flow continues through the draft tube, resulting in a flattening of the tangential velocity profile, the recirculation region becomes even more pronounced. It then disappears when the flow reaches the elbow in the draft tube (see Figure 4.3b). The contours of axial vorticity (Figure 4.3c) confirm the strong swirl just below the hub on the rotation axis, while almost no vorticity is observed in the outer regions of the runner outlet except for the near-wall region where strong shear stresses are present. In the guide vane cascade (see Figure 4.3a), the smooth flow pattern expected for best efficiency point is observed. There is no premature separation on the guide vanes, and no unusual perturbations are observed. The static pressure distribution on the blade pressure side (Figure 4.5) shows that half of the pressure energy is converted into torque and kinetic energy after one third of the blade length.

The Iso-surfaces of the q-criterion on Figure 4.6a show that there is separation just behind the leading edge of both the full-length blade and the splitter. This is surprising at design point, and can be an indication that the flow angles at the inlet boundary are not chosen correctly. Near the runner outlet, the wakes of the 15 runner blades are clearly visible in the pressure distribution (see Figure 4.6b), while the splitter wake can be identified on the pressure contours close to the trailing edge of the splitter (Figure 4.7). At the wall near the runner outlet (Figure 4.6b), small perturbations are observed which are partly originating from the splitter blade wake and partly from the separation on the leading edge. These perturbations are also observed on the q-criterion contours (Figure 4.8). Furthermore, the flow structures originating from the separation at the leading edge are convected downstream through the blade channel and remain close to the suction side of the blades. The separation point at the trailing edge of the blades is also visible on Figure 4.8.

Comparison with experimental data

Pressure distribution Figure 4.9 shows the pressure at each sensor, simulated with five different turbulence models. While there is some difference compared to the experimental measurements, the mixing plane results show a very good agreement with the unsteady simulations conducted by Trivedi *et al.* [7]. The quality of the mixing plane prediction seems to be just as good as the unsteady simulations, but both fail to exactly predict the experimental result. This is an indication that some phenomena taking place in the experiment can not be fully controlled or are not included in the simulations, independently of the accuracy and complexity of the numerical model. As the main difference in the trend occurs between the runner blades and the draft tube, possible causes could be cavitation phenomena or instabilities at the trailing edge of the blades which are not captured by RANS and URANS simulations.

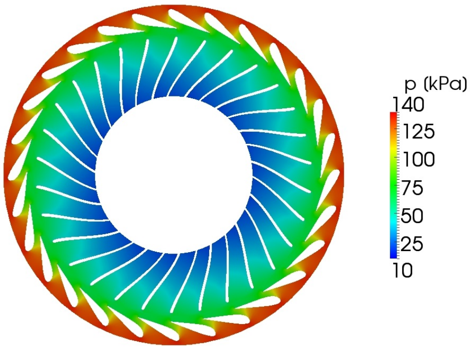

(a) *Pressure distribution in the guide vane passage and runner (cutting-plane $z = 0$) at best efficiency point.*

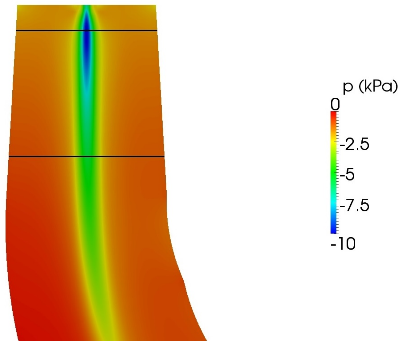

(b) *Pressure distribution in the symmetry plane ($y = 0$) of the runner outlet cone at best efficiency point. The black lines indicate the position of the velocity measurement lines.*

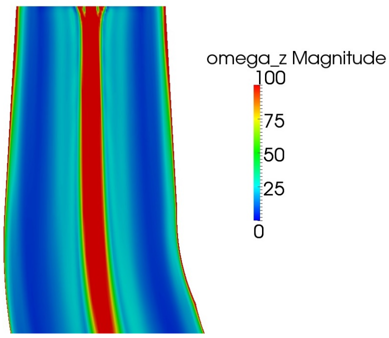

(c) *Distribution of axial vorticity in the symmetry plane ($y = 0$) of the runner outlet cone at best efficiency point.*

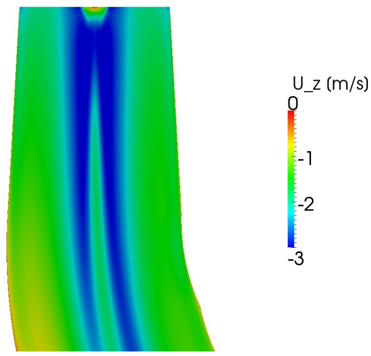

(d) *Distribution of axial velocity in the symmetry plane ($y = 0$) of the runner outlet cone at best efficiency point.*

Figure 4.3: *Contours of pressure, velocity and vorticity at best efficiency point.*

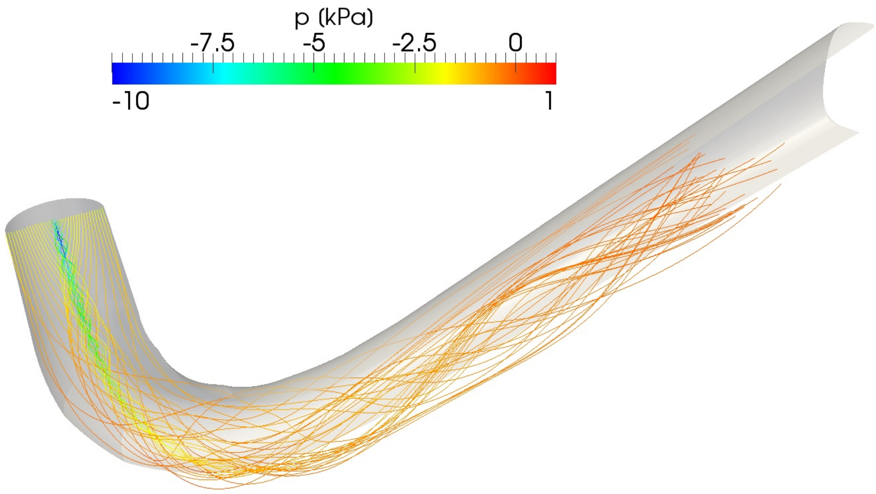

Figure 4.4: *Streamlines originating from a horizontal line at the runner outlet at best efficiency point.*

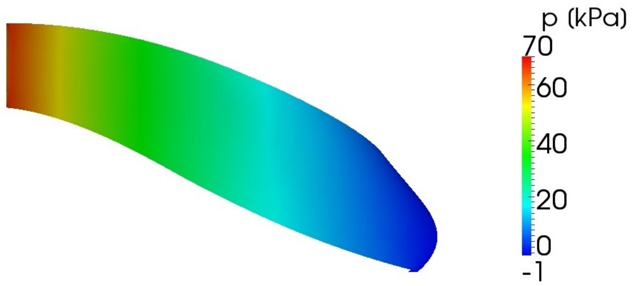

Figure 4.5: *Pressure distribution on the blade pressure side at best efficiency point.*

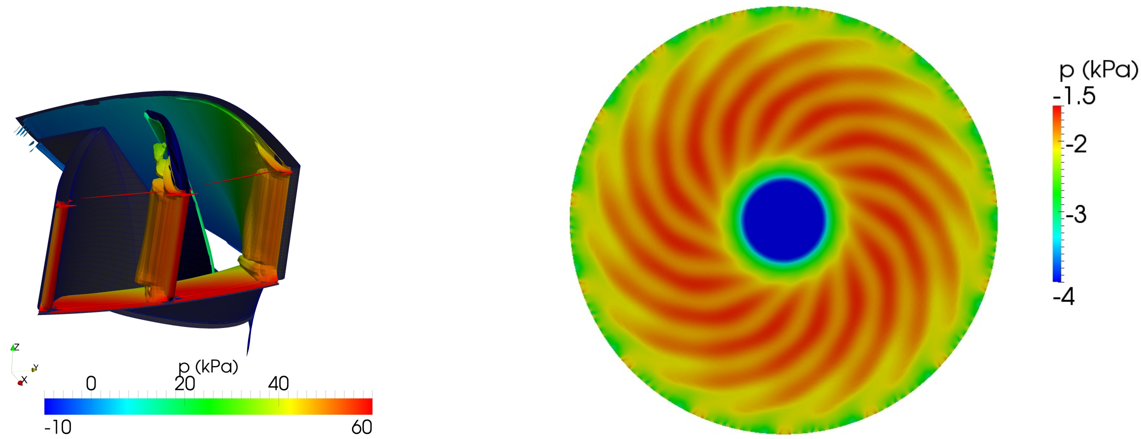

(a) *Iso-surface of q-criterion in the blade passage near the leading edge at best efficiency point, coloured by pressure.*

(b) *Pressure distribution near the runner outlet (cutting-plane $z = -0.175m$) for mixing plane simulations at best efficiency point using the standard k-ε model.*

Figure 4.6: *Blade wakes and coherent structures in the runner at best efficiency point.*

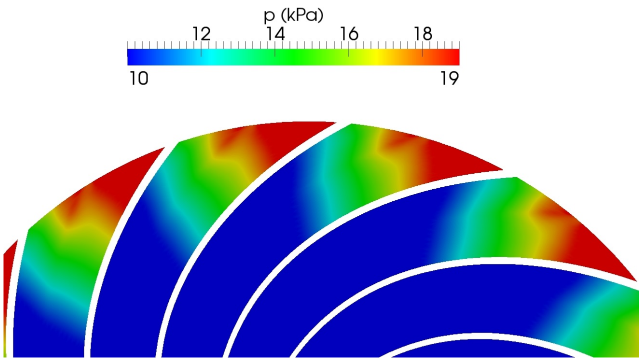

Figure 4.7: *Pressure distribution near the splitter blade trailing edge (cutting-plane $z = -0.09m$) for mixing plane simulations at best efficiency point using the standard k-ε model.*

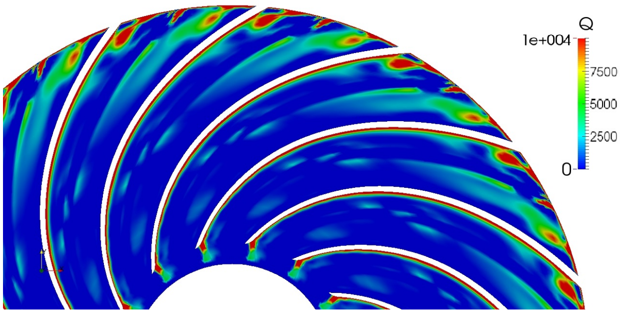

Figure 4.8: *Contours of q-criterion near the runner outlet and the trailing edge ($z = -0.09m$) at best efficiency point.*

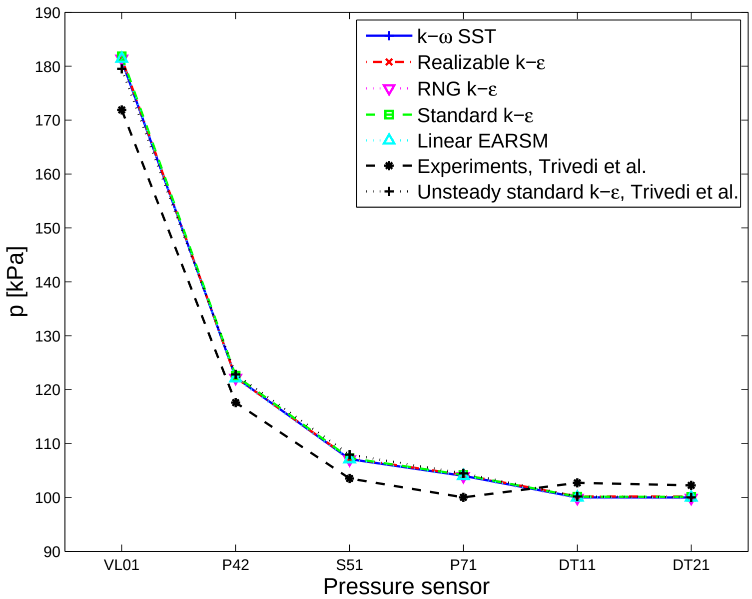

Figure 4.9: *Comparison of the pressure values at several locations with experimental and simulated results by Trivedi et al. [7] at best efficiency point.*

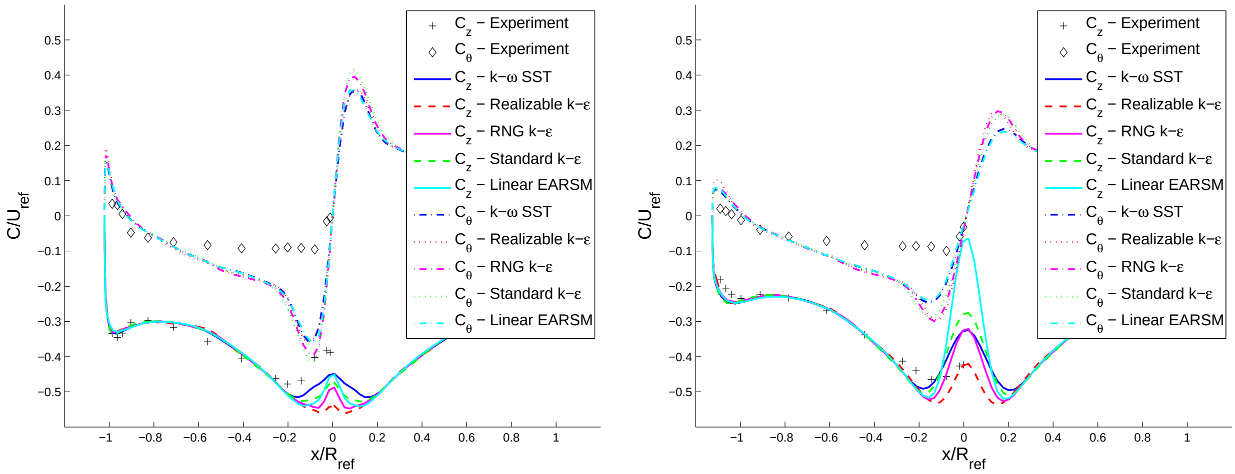

(a) *Velocity profiles at the runner outlet (line 1) for different turbulence models at best efficiency point (new operating point), compared with experimental results provided by the workshop committee [8].*

(b) *Velocity profiles at the runner outlet (line 2) for different turbulence models at best efficiency point (new operating point), compared with experimental results provided by the workshop committee [8].*

Figure 4.10: *Velocity profiles at the runner outlet at best efficiency point. C_z denotes the axial velocity component and C_θ the tangential velocity component. Velocities are normalised by the circumferential reference velocity U_{ref}, and the x axis by the runner outlet radius R_{ref}.*

Velocity profiles As the velocity measurements are conducted at different operating conditions than the original ones (see Section 2.3), these new operating points are used for the comparison of the velocity profiles. The velocity data for the original operating points can be found in Appendix A.1. Figure 4.10a shows the velocity profile at line 1 below the runner outlet. The shape of the axial velocity profile is well predicted, except for the size of the recirculation zone below the hub, which differs depending on the turbulence model that is used. While the results near the draft tube wall show good agreement with the experimental data regarding the tangential velocity, a difference can be observed close to the rotation axis. The measurements show a mostly swirl free flow with identical (but low) tangential velocity over the whole width of the draft tube, as it is expected for operation at best efficiency point. The mixing plane results on the other hand present a strong confined swirl in the counter-clockwise direction (opposed to the runner rotation) near the rotation axis. Figure 4.10b shows the velocity profiles at the second measurement line. Once again, the axial velocity corresponds very well to the measurements, while the swirl in the centre is stronger than in the experiments.

Efficiency Table 4.1 shows the hydraulic efficiency for all turbulence models. Contrary to the pressure distribution, the efficiency estimations show a large difference between the mixing plane simulations and experimental measurements or unsteady simulations. This can be caused by the fact that a large part of the losses occur in the spiral casing, in the complex interaction between guide vane wakes and runner blades, and below the runner outlet in the recirculation region. The spiral casing and the stay vane passage are not modelled, which removes a large part of these losses. Furthermore, the wakes of the guide vane passage and the runner blades are averaged out by the mixing plane interface, potentially reducing dissipation in these regions.

Turbulence model	Hydraulic efficiency (IEC) $\eta_{h,IEC}$ [%]	Hydraulic efficiency (F99) $\eta_{h,F99}$ [%]
Standard $k-\varepsilon$	94.0345	98.6320
RNG $k-\varepsilon$	94.0141	98.6152
Realizable $k-\varepsilon$	93.8984	98.5144
$k-\omega$ SST	94.5752	99.2575
Linear EARSM	94.5785	99.2540

Table 4.1: Efficiency values at best efficiency point for different turbulence models.

Influence of the turbulence model

While the choice of the turbulence model has only minor influence on the pressure distribution in the machine (see Figure 4.9), it influences the solution of the flow field in the swirling region at the outlet of the runner. The important difference between the models in the velocity profiles (Figures 4.10a and 4.10b) can partly explain the different efficiency prediction, as a large part of the losses is generated in this region. The prediction of the swirl at the runner outlet is largely identical for all models, but a strong difference appears regarding the axial velocity near the axis of rotation. Depending on the model that is chosen, the importance of the wake below the hub can vary considerably. This has an influence on the predicted losses and thus the head, as it is shown in Table 4.2. For the first measurement line (Figure 4.10a), all models underestimate the velocity gradient in this region, while at the second measurement line (Figure 4.10b) the RNG k-ε model seems to be the most appropriate to predict the experimental phenomena. It gives however the worst prediction for the wake zone at line 1. The profile at the second measurement line depends mainly on the length of the predicted recirculation zone, as the second line is located in the region where the wake starts to disappear (see Figure 4.3b). A slight difference in the predicted length of this zone can therefore create a big difference in the local velocity profile. Globally, k-ω SST and Realizable k-ε show the best overall agreement, with the first performing better near the hub while the latter predicts well the recirculation zone further down in the draft tube.

Turbulence model	$P[W]$	$H_{IEC}[m]$	$H_{F99}[m]$
Standard $k-\varepsilon$	25832.25	13.790	13.148
RNG $k-\varepsilon$	25802.55	13.778	13.135
Realizable $k-\varepsilon$	25661.10	13.719	13.076
$k-\omega$ SST	25672.65	13.627	12.984
Linear EARSM	25710.00	13.646	13.003

Table 4.2: Mechanical power and head with (H_{IEC}) and without (H_{F99}) the potential energy term at best efficiency point.

Draft tube

The performance of the draft tube can be evaluated from Figure 4.11 which shows the pressure distribution in the diffuser at best efficiency point. The pressure difference between the elbow and the draft tube outlet is approximately $1kPa$, which corresponds to $0.1m$ of pressure head. Compared to the overall head of the turbine, the contribution of the draft tube is therefore very low. The shape of the draft tube has however an important influence regarding the mixing plane simulations. Due to long straight part of the draft tube before the elbow, the runner wake remains largely symmetric and has almost disappeared when the flow reaches the elbow. If the elbow was located closer to the runner outlet, asymmetries might arise and perturb the mixing plane.

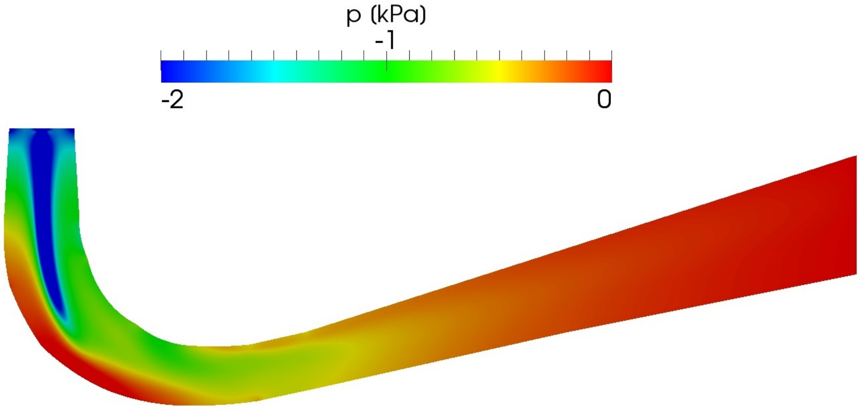

Figure 4.11: *Pressure distribution in the draft tube (cutting-plane $y = 0$) at best efficiency point.*

4.1.2 Part load

Overview and qualitative analysis

At part load, the expected strong swirl at the runner outlet is observed (Figure 4.12a) as described by Avellan [35] and by Dörfler *et al.* [36] for lower part load ($Q_{ED}/Q_{ED,BEP} = 1/3$). The swirling fluid is carried to the wall of the draft tube by the centrifugal force, which creates a large low pressure region in the centre (Figure 4.12b). In this low pressure region, back-flow with positive z velocity occurs (Figure 4.12c). This leads to the particular appearance of the streamlines (Figure 4.13), where the central part seems to be rotating in the opposite direction, while it is in fact rotating in the same direction but moving upwards. The axial velocity profile is somewhat flattened as the flow moves through the draft tube, while the swirling motion in the outer part remains nearly unaffected and starts to disappear only once the elbow is passed. The swirling zone is almost symmetric, with a slight shift to the negative x direction which is caused by the elbow. A small zone of positive axial vorticity just below the hub (see Figure 4.12a) is rotating in the opposite direction of the runner and the main swirl. This secondary flow is however quickly overpowered by the strong swirling motion and is only present in this confined recirculation zone. The contours of q-criterion in Figure 4.14 show the coherent structures in the region around the trailing edge of the blades. The most visible feature is the strong separation that takes place on the suction side of the blades, which is caused by the disadvantageous flow angles and pressure distributions at part load due to the modified flow rate and guide vane angle. On the splitter blade, the separation takes place close to the trailing edge. In the guide vane passage (Figure 4.12d), the effect of the modified relative angles between the stay vanes and guide vanes is visible. The stagnation point on the guide vane has moved from the leading edge to the high pressure side, and the high pressure side is at a almost uniform pressure. Due to the strong inclination of the guide vanes, the main pressure drop occurs in the very narrow and short channel between the leading and trailing edge of two consecutive guide vanes. In the runner, half of the pressure difference is converted into torque and kinetic energy after one fourth of the blade length (see Figure 4.15).

Comparison with experimental data

Pressure distribution The pressure evolution in the turbine (see Figure 4.16) shows good agreement with available experimental and numerical results. While the results almost perfectly match the unsteady simulations by Trivedi *et al.* [7], there still remains an important difference to the experimental measurements, even though the general trend is well predicted. Once again, both types of simulations fail to predict the experimental result exactly, which is an indication that some phenomena taking place in the experiment can not be fully controlled or are not included in the simulations.

Velocity profiles The velocity profiles (Figures 4.17a and 4.17b) show good agreement with the experimental results regarding both the axial and tangential velocity. At the first measurement line, a very strong swirl in the clockwise direction near the draft tube wall is observed, which decreases towards the centre where almost no swirl is present. The profile is then equilibrated to end up being almost linear at the second measurement line (Figure 4.17b), corresponding to a solid body rotation. Similarly, the profile of axial velocity, which shows a positive peak around $r/R_{ref} = 0.6$ and a negative peak near the wall, is flattened as the flow moves on in the draft tube. Note the very large region in the centre where the z velocity is positive, with only the swirling region near the wall having a negative z velocity. All of the flow is thus passing near the wall of the draft tube, while in the centre there is a large back-flow region stretching over two thirds of the draft tube width. This observation is consistent with the axial velocity contours (Figure 4.12c), where the red zone in the centre corresponds to an axial velocity in the upstream direction.

Efficiency The difference between simulations and experiment is much larger for the efficiency prediction than for the flow field, as it is shown in Table 4.3. Figure 4.1 shows a large drop in efficiency by 15% compared to best efficiency point for most turbulence models, while the experimental difference is around 20%. This is a further indication that a part of the error comes from the spiral casing. If the flow rate moves away from best efficiency point, the flow angles are no longer optimal and losses between the stay vanes and guide vane cascade increase. As this phenomena are not modelled in the mixing plane simulations, the gap between the numerical results and the experiments increases. Once again, a part of the error is expected to be due to the averaging at the mixing plane interface, which reduces the complexity of the wakes at the runner inlet and outlet, thus decreasing the dissipation in these regions.

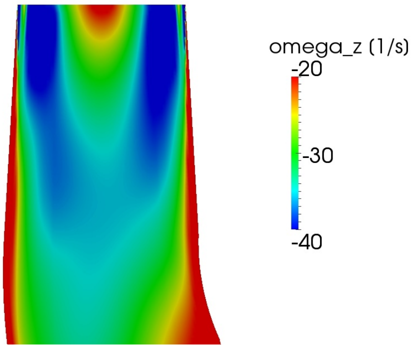

(a) *Distribution of axial vorticity in the symmetry plane ($y = 0$) of the runner outlet cone at part load operation.*

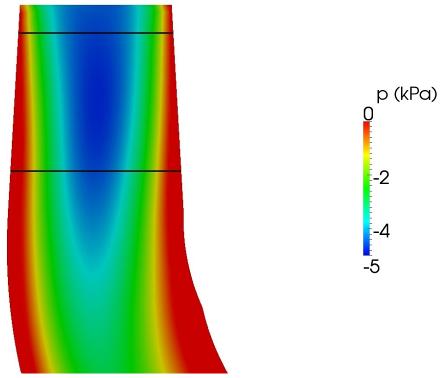

(b) *Pressure distribution in the symmetry plane ($y = 0$) of the runner outlet cone at part load operation. The black lines indicate the position of the velocity measurement lines.*

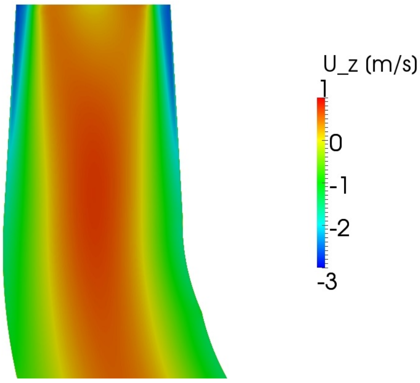

(c) *Distribution of axial velocity in the symmetry plane ($y = 0$) of the runner outlet cone at part load operation.*

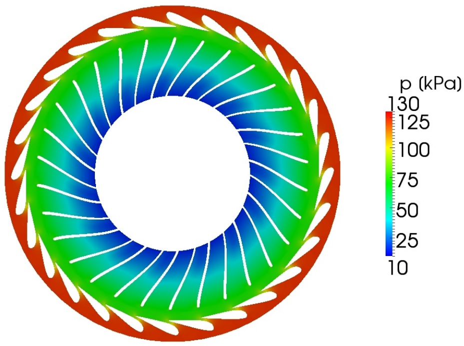

(d) *Pressure distribution in the guide vane passage and runner (cutting-plane $z = 0$) at part load operation.*

Figure 4.12: *Contours of pressure, velocity and vorticity at part load.*

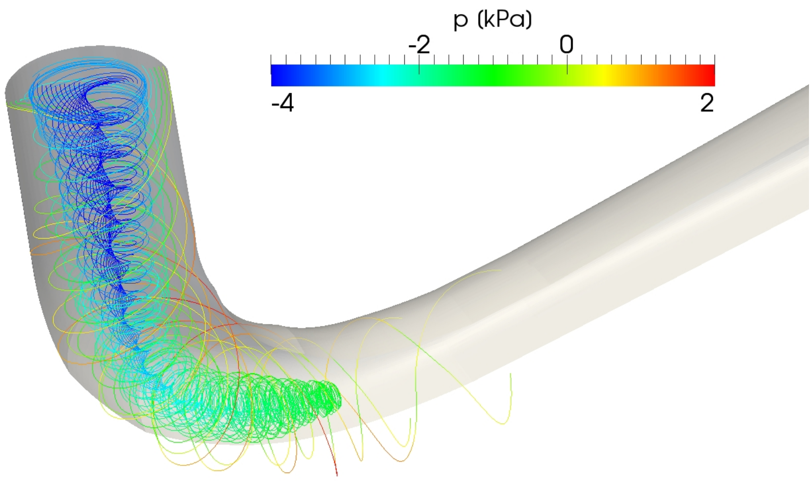

Figure 4.13: *Streamlines originating from a horizontal line at the runner outlet at part load operation.*

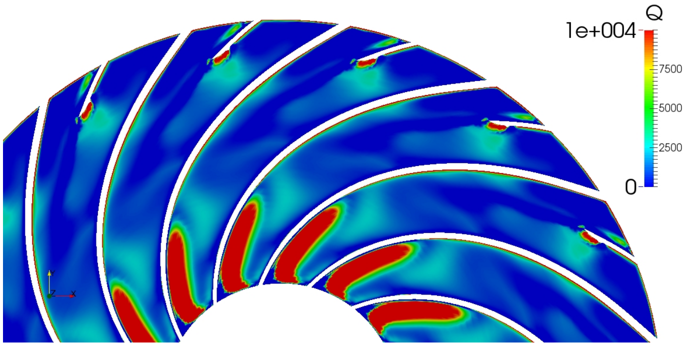

Figure 4.14: *Contours of q-criterion near the blade trailing edges ($z = -0.08m$) at part load.*

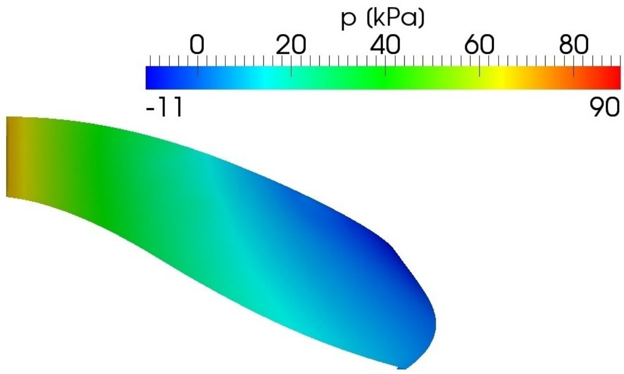

Figure 4.15: *Pressure distribution on the blade pressure side at part load operation.*

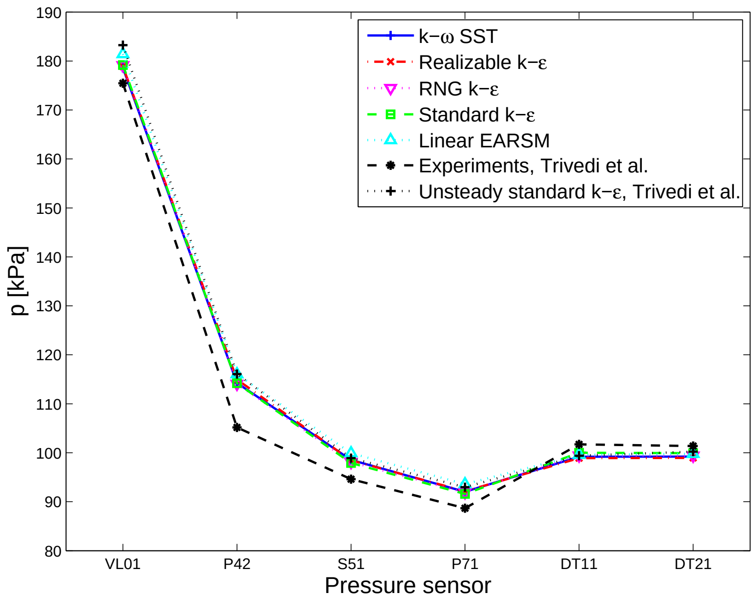

Figure 4.16: *Comparison of the pressure values at several locations with experimental and simulated results by Trivedi et al. [7] at part load.*

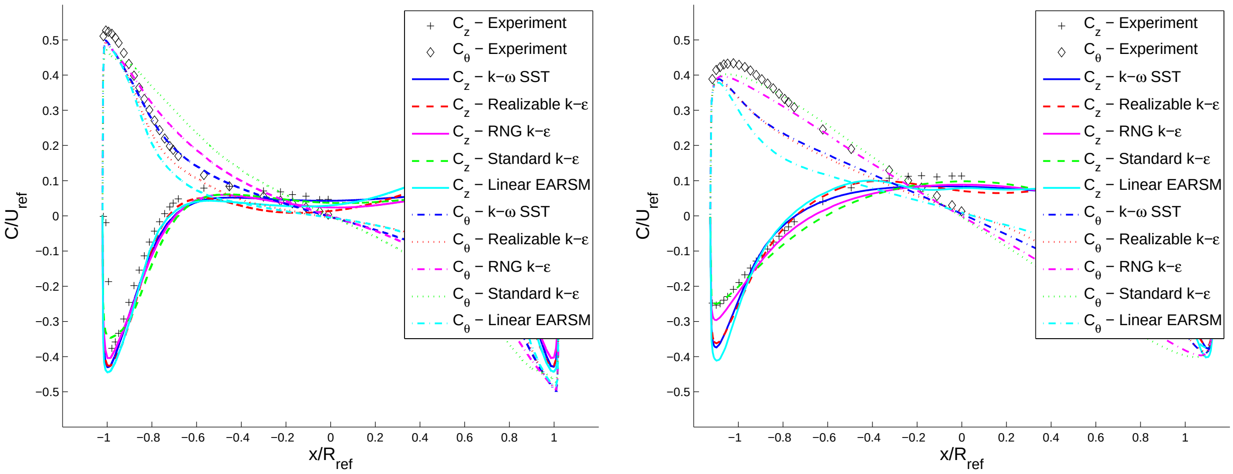

(a) *Velocity profiles at the runner outlet (line 1) for different turbulence models at part load operation, compared with experimental results provided by the workshop committee [8].*

(b) *Velocity profiles at the runner outlet (line 2) for different turbulence models at part load, compared with experimental results provided by the workshop committee [8].*

Figure 4.17: *Velocity profiles at the runner outlet at part load. C_z denotes the axial velocity component and C_θ the tangential velocity component. Velocities are normalised by the circumferential reference velocity U_{ref}, and the x axis by the runner outlet radius R_{ref}.*

Turbulence model	Hydraulic efficiency (IEC) $\eta_{h,IEC}$ [%]	Hydraulic efficiency (F99) $\eta_{h,F99}$ [%]
Standard $k-\varepsilon$	78.263	82.296
RNG $k-\varepsilon$	77.628	81.673
Realizable $k-\varepsilon$	80.586	84.973
$k-\omega$ SST	82.808	87.558
Linear EARSM	89.041	94.245

Table 4.3: Efficiency values at part load for different turbulence models.

Influence of the turbulence model

Similarly to the best efficiency point simulations, considerable differences exist depending on the choice of the turbulence model when it comes to predicting the velocity field, the efficiency or the head (Table 4.4), while it has almost no influence on the pressure distribution. The velocity profiles in Figure 4.17 show that the differences among the models are just as large as the difference to the experimental and unsteady results, meaning that the choice of the right turbulence model can have an impact which is just as important as the general case set-up and geometry simplifications. For the velocity profiles at the first measurement line, k-ω SST, Realizable k-ε or linear EARSM predict the swirling motion at the runner outlet most accurately. The other models give results which are qualitatively similar, but further away from the experimental data. However, the second measurement line shows that these three models largely over-predict the axial velocity in the near-wall region, while standard k-ε and RNG k-ε are much closer to the experimental data and predict correctly the shape of the axial profile as well as the swirl. There is therefore no clear optimal model, with some giving good agreement at the first measurement line while others are closer to the experiment at the second measurement line. Standard k-ε and RNG k-ε give the best prediction for efficiency and acceptable velocity profiles at both measurement lines, with RNG k-ε being the one that performs slightly better. If however the exact modelling of the flow field below the hub is of greater interest than the overall prediction, k-ω SST or Realizable k-ε are better suited.

Turbulence model	$P[W]$	$H_{IEC}[m]$	$H_{F99}[m]$
Standard $k-\varepsilon$	7152.435	13.117	12.474
RNG $k-\varepsilon$	7018.815	12.977	12.334
Realizable $k-\varepsilon$	6991.620	12.452	11.809
$k-\omega$ SST	6835.755	11.848	11.205
Linear EARSM	7222.080	11.641	10.998

Table 4.4: Mechanical power and head with (H_{IEC}) and without (H_{F99}) the potential energy term at part load operation.

4.1.3 High load

Overview and qualitative analysis

The high load results show a confined region close to the axis of rotation with counter-clockwise swirl (i.e. against the runner rotation), which is visible in the streamlines (Figure 4.18) and the contours of axial vorticity (Figure 4.19a). The pressure in this region is considerably lower (Figure 4.19b). This flow pattern corresponds to what is expected for high load operation [3, 35, 36], with a swirl against the direction of rotation due to the excess in tangential velocity created by the higher flow rate. The profile in the outer regions of the draft tube shows some radial variations of the tangential velocity. While the swirl in the centre is somewhat attenuated until the second measurement line, the radial variations remain almost unchanged. The axial velocity shows a maximum just below the hub, as well as a local maximum close to the draft tube wall, which can also be seen on the contours of axial velocity (Figure 4.19c). At the axis of rotation there is a relatively small wake caused by the hub, which then becomes larger at the second measurement line. In the guide vane cascade (Figure 4.19d), the flow remains more or less unaffected by the increase in flow rate apart from a slightly moved stagnation point. As for best efficiency point, half of the static pressure difference in the runner is converted into kinetic energy or transmitted to the blades after one third of the blade length (Figure 4.20).

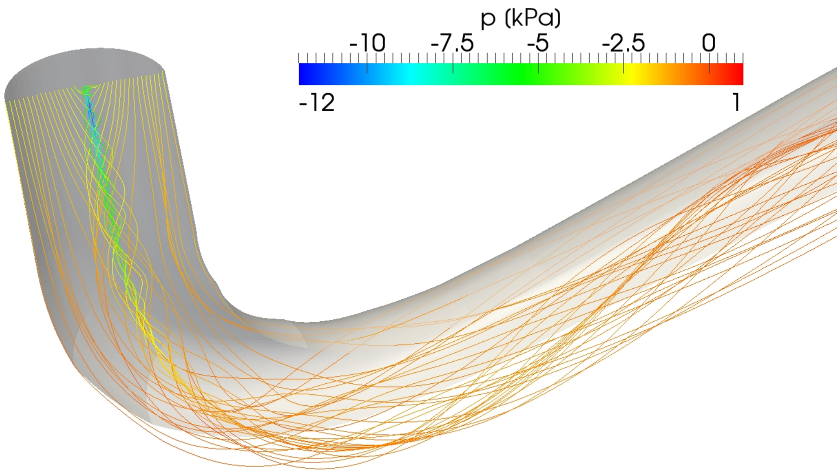

Figure 4.18: *Streamlines originating from a horizontal line at the runner outlet at high load.*

The iso-surfaces of the q-criterion in Figure 4.21a show the flow structures at the runner inlet. On the suction side of the blade and the splitter blade, a separation region is observed shortly after the leading edge. This is expected for high load, as the higher flow rate and modified guide vane position lead to a higher angle of attack at the leading edge. The flow is no longer aligned with the blade and not able to follow the blade surface, and separation occurs shortly after the leading edge. In addition, two vortices are observed at the leading edge of each blade and splitter, originating from both ends of the leading edge near the hub and shroud. These structures propagate through the blade channel (Figure 4.21b), where they remain close to the suction side of the blades and splitters.

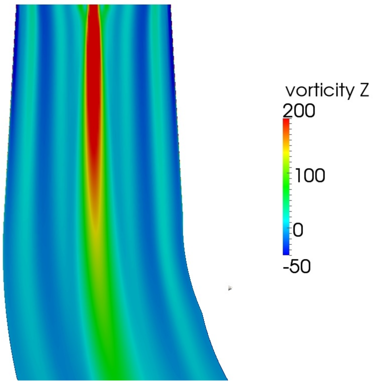

(a) *Distribution of axial vorticity in the symmetry plane ($y = 0$) of the runner outlet cone at high load.*

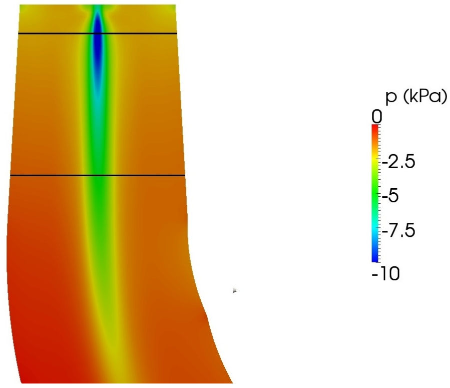

(b) *Pressure distribution in the symmetry plane ($y = 0$) of the runner outlet cone at high load. The black lines indicate the position of the velocity measurement lines.*

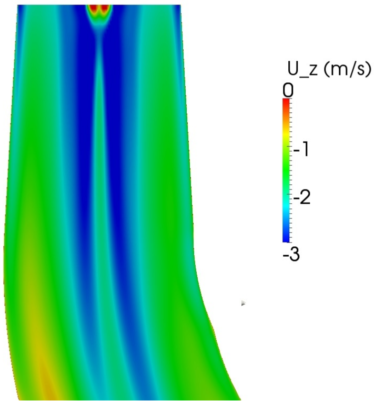

(c) *Distribution of axial velocity in the symmetry plane ($y = 0$) of the runner outlet cone at high load.*

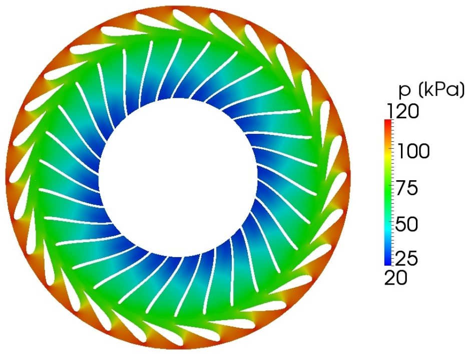

(d) *Pressure distribution in the guide vane passage and runner (cutting-plane $z = 0$) at high load.*

Figure 4.19: *Contours of pressure, velocity and vorticity at high load.*

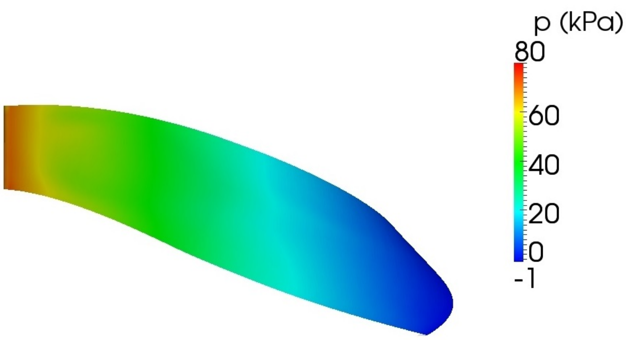

Figure 4.20: *Pressure distribution on the blade pressure side at high load.*

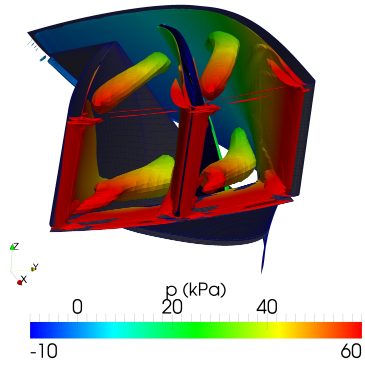

(a) *Iso-surface of q-criterion in the blade passage near the leading edge at high load, coloured by pressure.*

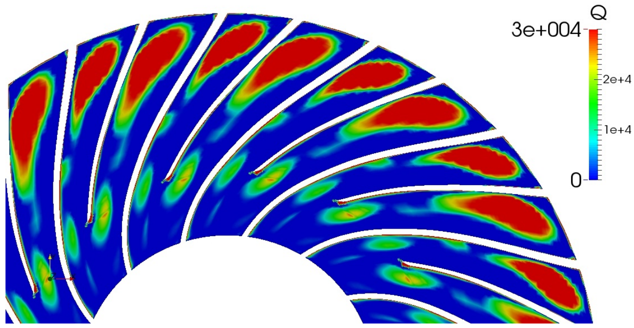

(b) *Contours of q-criterion in the blade passage near the trailing edge ($z = -0.04m$) at high load.*

Figure 4.21: *Coherent structures in the runner at high load.*

Comparison with experimental data

Pressure distribution The trend of the pressure distribution at the sensor locations (Figure 4.22) is predicted correctly by the mixing plane simulations. However, the difference to the experimental results and unsteady simulations by Trivedi *et al.* [7] is larger than for the other operating points. In particular, the pressure drop in the guide vane passage is underestimated. This can be caused a bad choice of the flow angle for the inlet boundary condition, leading to an under-prediction of the losses in the guide vane cascade. In order to obtain a more accurate prediction, the angle should be determined for example by simulating the flow through the stay vane and guide vane cascade separately or by using results from an unsteady simulation. Between the runner outlet and the draft tube, the simulations predict a drop in pressure while the experiment shows an increase, as it is the case at best efficiency point. Contrary to all other simulations, the standard k-ε mixing plane results predict correctly the pressure values in the blade passage that are observed experimentally.

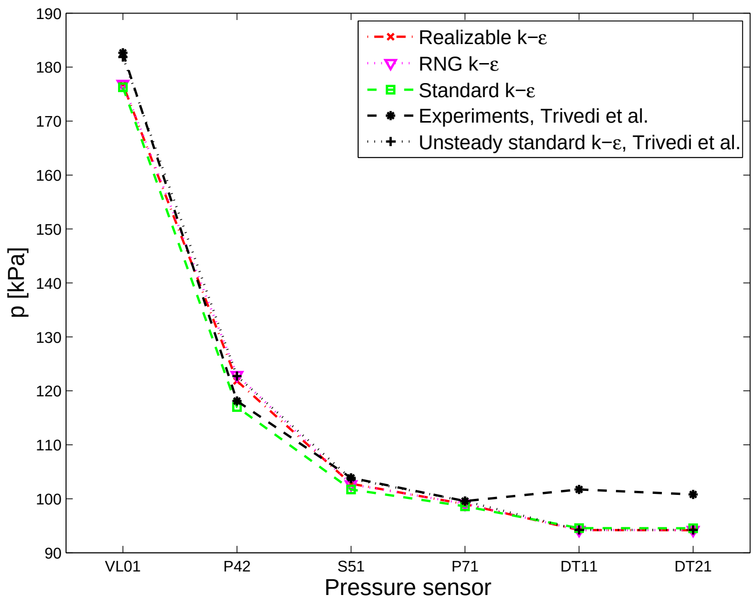

Figure 4.22: *Comparison of the pressure values at several locations with experimental and simulated results by Trivedi et al. [7] at high load.*

Velocity profiles The velocity profiles show good agreement with the experimental results at the first measurement line (Figure 4.23a). However, most models strongly over-predict the swirl near the axis of rotation,

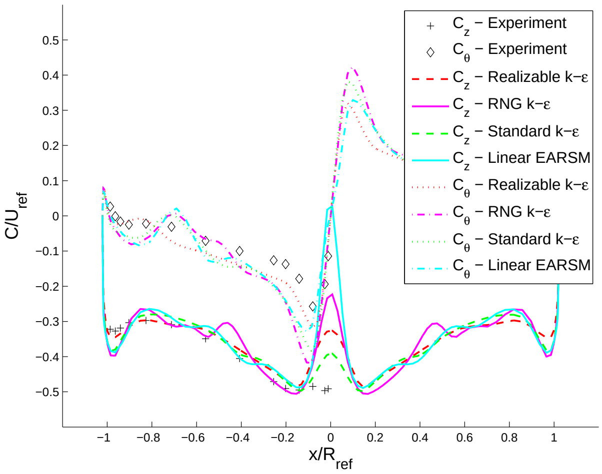

(a) *Velocity profiles at the runner outlet (line 1) for different turbulence models at high load (new operating point), compared with experimental results provided by the workshop committee [8].*

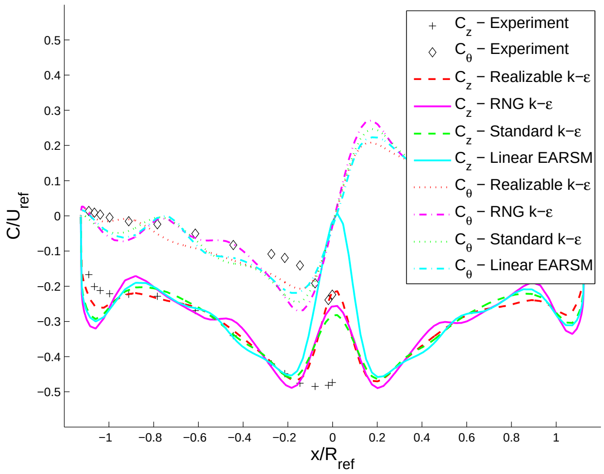

(b) *Velocity profiles at the runner outlet (line 2) for different turbulence models at high load (new operating point), compared with experimental results provided by the workshop committee [8].*

Figure 4.23: *Velocity profiles at the runner outlet at high load. C_z denotes the axial velocity component and C_θ the tangential velocity component. Velocities are normalised by the circumferential reference velocity U_{ref}, and the x axis by the runner outlet radius R_{ref}.*

and a recirculation zone below the hub is predicted which is not seen in the experiment. Except for the region near the axis of rotation, the results agree well with the experiments, but show some radial fluctuations which are not observed experimentally. At the second section (Figure 4.23b), the amount of swirl is correctly predicted, but the recirculation near the rotation axis is still present.

Efficiency The predicted efficiency values (Table 4.5) are much higher than the experimental values, and the realizable k-ε model gives even a value value above 100% for the efficiency $\eta_{h,F99}$. As the potential energy term is not included, this is however not necessarily unphysical. Surprisingly, the values are larger than at the designated best efficiency point. Most certainly this is caused by an inaccurate choice of the flow angle at the inlet.

Turbulence model	Hydraulic efficiency (IEC) $\eta_{h,IEC}$ [%]	Hydraulic efficiency (F99) $\eta_{h,F99}$ [%]
Standard $k-\varepsilon$	93.99	99.49
RNG $k-\varepsilon$	93.88	99.42
Realizable $k-\varepsilon$	94.81	100.40

Table 4.5: Efficiency values at high load for different turbulence models.

Influence of the turbulence model

Contrary to the other operating points, the turbulence model has an influence on the predicted pressure values in the turbine at high load. The standard k-ε model predicts correctly the difference between blade pressure and suction side which is measured experimentally, while all the other models follow the trend of the simulations by Trivedi *et al.* [7]. The different predictions of the losses also influence the obtained head, which is shown in Table 4.6. Large differences exist regarding the prediction of velocity profiles at the outlet (Figures 4.23a and 4.23b). The realizable k-ε model gives the best prediction of the swirl, while all other models strongly over-predict it. All models predict the axial velocity profile well, but overestimate the extent and intensity of the recirculation zone below the hub. Once again, the realizable k-ε model gives the best agreement with experimental data.

Turbulence model	$P[W]$	$H_{IEC}[m]$	$H_{F99}[m]$
Standard $k-\varepsilon$	23746.65	11.65	11.01
RNG $k-\varepsilon$	23514.60	11.55	10.91
Realizable $k-\varepsilon$	23717.40	11.54	10.89

Table 4.6: Mechanical power and head with (H_{IEC}) and without (H_{F99}) the potential energy term at high load operation.

4.1.4 Wall $y+$ values and mesh refinement

As wall functions are used to model the near-wall region, the values of the non-dimensional wall distance y^+ are calculated on all boundary patches. This shows that on several patches the values are considerably above or below the optimal value of $y^+ = 30$ which is good practice for high-Reynolds wall functions [37]. Such values could be a cause for the discrepancy regarding the simulated efficiency values and velocity profiles. A detailed analysis of the y^+ values including a comparison between the original and a refined mesh at best efficiency point is shown in Appendix C.2.

4.1.5 Convergence

In order to evaluate the convergence behaviour of the steady-state simulations, the pressure and velocity residuals are followed during the simulations. Additionally, the evolution of physical quantities is observed, allowing to verify whether the solution is stabilised. The evolution of the residuals and an evaluation of the convergence for the steady-state simulations are presented in Appendix B.1. All best efficiency point simulations are run for 10000 iterations. For the part load and high load cases, the simulations are run for 15000 iterations to stabilise the solution sufficiently. On 32 cores, the computational time for best efficiency point simulations for 10000 iterations is 36 hours, while for part load and high load simulations the computational time for 15000 iterations is 47 hours.

4.2 Unsteady simulations with constant rotational speed

Due to the large computational resources that are needed for the unsteady simulations, the new operating points for the velocity measurements are not simulated. The comparison between the experimental and simulated velocity profiles has therefore to be interpreted with care and can only give qualitative information about the accuracy of the results. Figures 4.24 and 4.25 show the efficiency values without and with the gravitational term for all three operating points using the standard k-ε and k-ω SSTF model. The results show good agreement with experimental data at best efficiency point, and correct trends but larger errors at off-design conditions. This trend corresponds to the unsteady results by Trivedi *et al.* [7] The difference between the standard k-ε and the k-ω SSTF model is very small both at best efficiency point and at off-design operation. In addition, the unsteady results give the losses in total pressure between the spiral casing inlet and the runner outlet, which correspond to 6.32% of the available energy at the turbine at part load, 3.86 % at best efficiency point and 2.96% at high load. This suggests that a large part of the efficiency over-estimation in the mixing plane simulations comes indeed from the reduction of the computational domain.

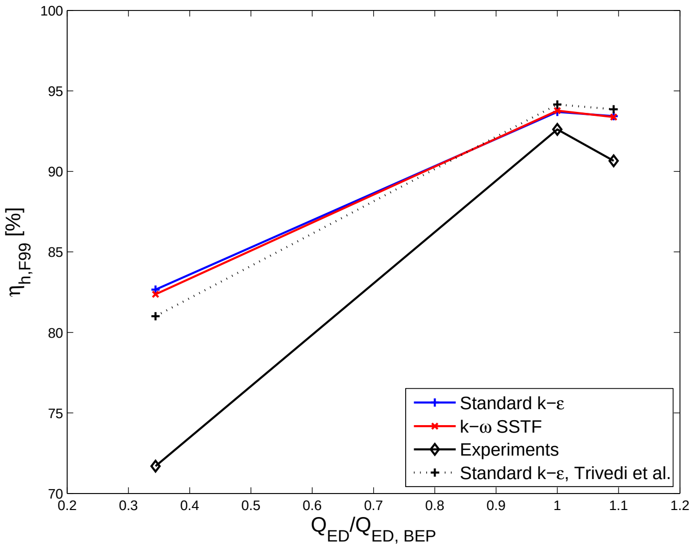

Figure 4.24: *Hydraulic efficiency (without the gravitational term) depending on the discharge compared to the experimental values provided by the workshop committee [8] and unsteady simulations by Trivedi et al. [7].*

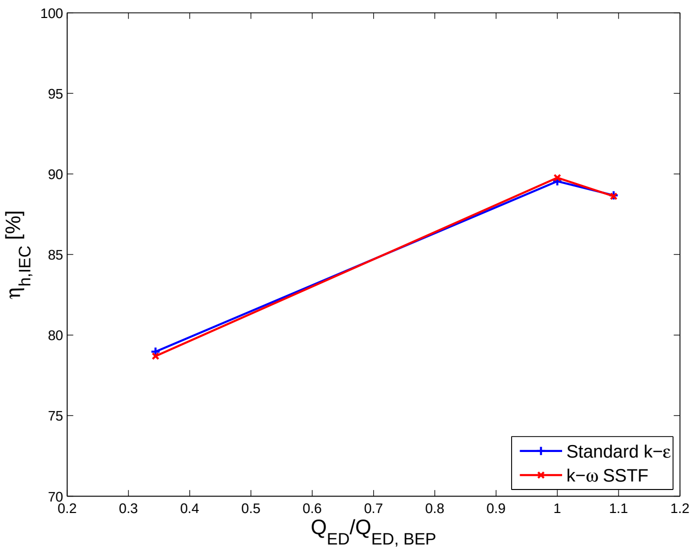

Figure 4.25: *Hydraulic efficiency as defined by the IEC standards depending on the discharge.*

4.2.1 Best efficiency point

Overview

The pressure contours of the spiral casing and guide vane cascade (Figure 4.26) show a very even and symmetric flow. In the streamlines at the runner outlet (Figure 4.27), an unusually strong swirl near the rotation axis can be seen, as it is expected for high load operation rather than best efficiency point. Similar observations were already made in Section 4.1.1 with the mixing plane simulations. This is confirmed by the contours of pressure (Figure 4.28) and axial vorticity (Figure 4.29a), which show a low pressure zone below the hub where the axial vorticity is very high and positive, corresponding to a counter-clockwise rotation. The axial velocity (Figure 4.29b) is low at the rotation axis, while in a region originating from the hub a very high axial velocity is observed.

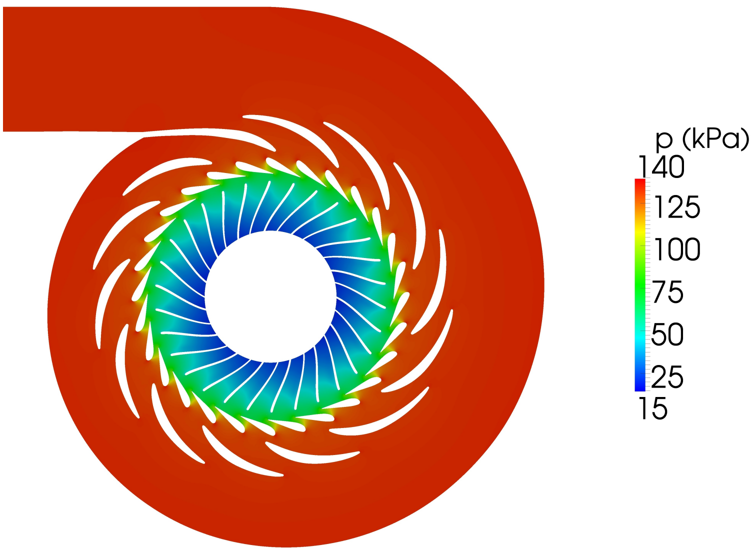

Figure 4.26: *Mean pressure distribution in the spiral casing, guide vane passage and runner (cutting-plane $z = 0$) at best efficiency point.*

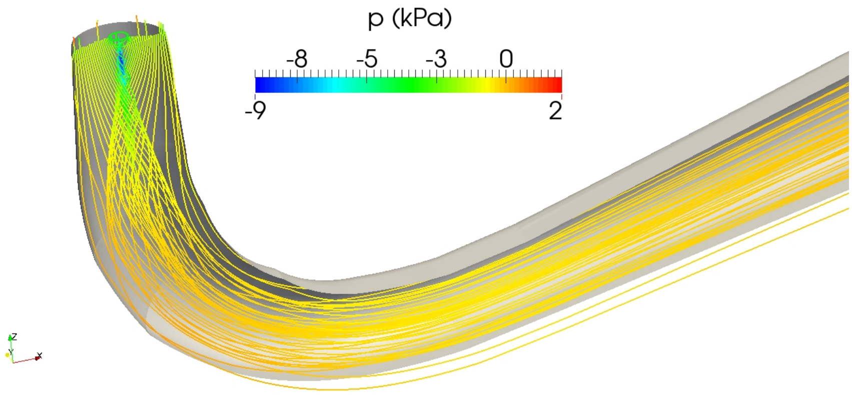

Figure 4.27: *Streamlines originating from a horizontal line at the runner outlet at best efficiency point.*

On Figure 4.30, the iso-surfaces of q-criterion show that on both the full length blades and the splitter blades, separation occurs shortly after the leading edge. This is surprising as the flow angles at the runner inlet should be optimal at best efficiency point and the flow coming from the guide vane cascade should be aligned with the blades. Together with the excess swirl that is observed, this is an indication that the flow rate and angle do not perfectly match the design conditions. It is unclear whether this comes from a particularity in

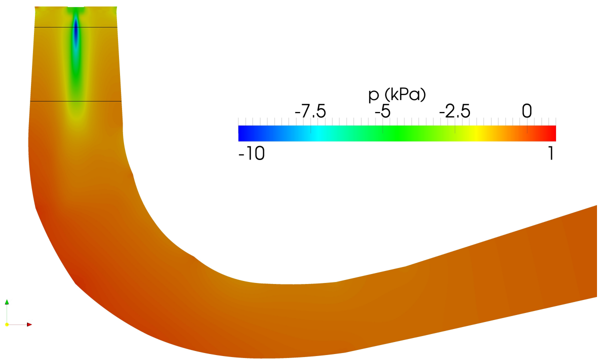

Figure 4.28: *Mean pressure distribution in the symmetry plane ($y = 0$) of the draft tube at best efficiency point.*

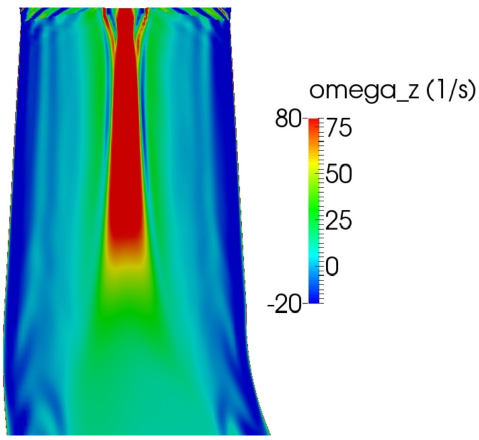

(a) *Instantaneous distribution of axial vorticity in the symmetry plane ($y = 0$) of the runner outlet cone at best efficiency point.*

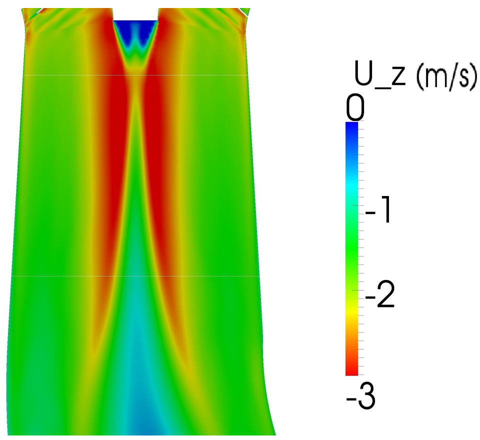

(b) *Mean distribution of axial velocity in the symmetry plane ($y = 0$) of the runner outlet cone at best efficiency point.*

Figure 4.29: *Flow field in the symmetry plane of the runner outlet cone at best efficiency point.*

the design of the blade profiles, an error in the measurements leading to a wrong choice of the best efficiency conditions or from an erroneous case set-up. Figures 4.31, 4.32 and 4.33 show contours of the q-criterion at different heights in the guide vane cascade and runner inlet. While on the full-length blades the separated region remains close to the suction side of the blade, it is carried away from the blade surface on the splitter blade. Figure 4.31 also shows that the separation is much more important on splitter blades, especially in the upper part of the leading edge.

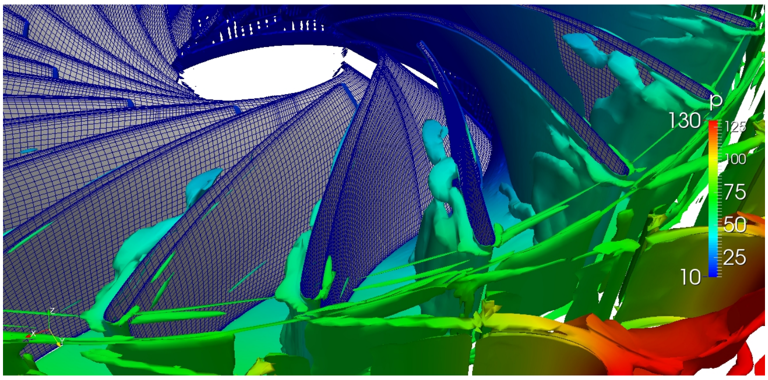

Figure 4.30: *Iso-surfaces of q-criterion at the runner inlet at best efficiency point.*

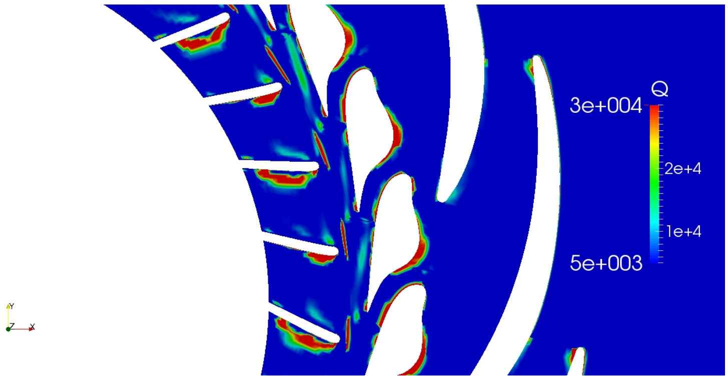

Figure 4.31: *Contours of q-criterion in the guide vane cascade ($z = 0.025m$) at best efficiency point.*

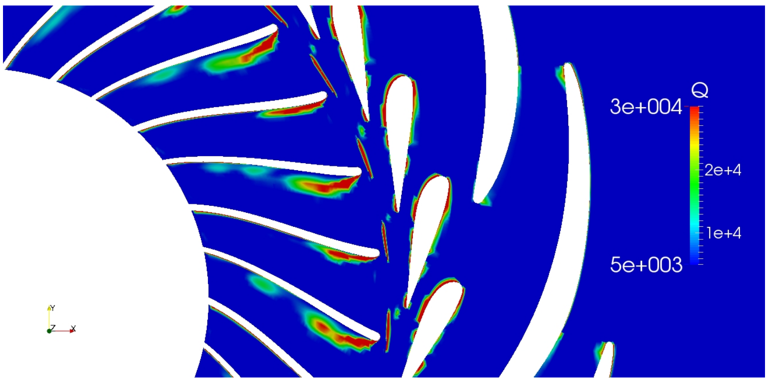

Figure 4.32: *Contours of q-criterion in the guide vane cascade ($z = 0$) at best efficiency point.*

At the trailing edge of the blades, no coherent structures are seen except for the wall effects near the shroud of the runner. On Figure 4.34, small perturbations near the shroud are visible which originate from the wakes of the splitter blades and the vortices generated at the blade leading edge.

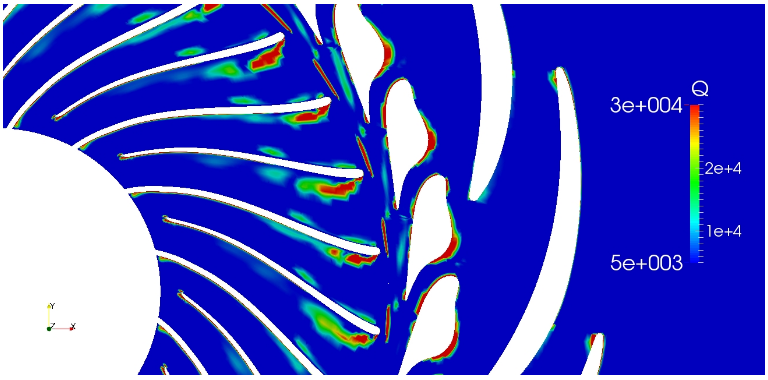

Figure 4.33: *Contours of q-criterion in the guide vane cascade ($z = -0.025m$) at best efficiency point.*

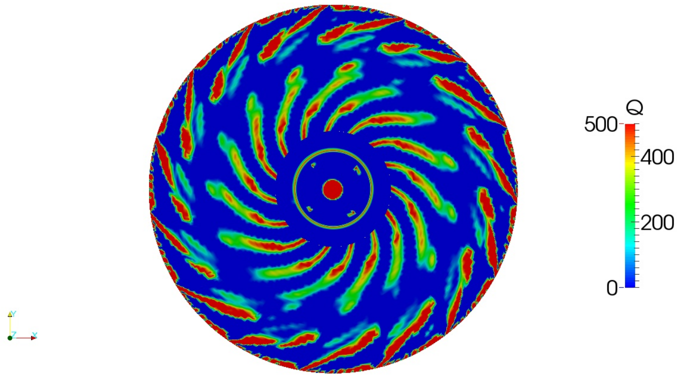

Figure 4.34: *Contours of q-criterion at the runner outlet ($z = -0.16m$) at best efficiency point.*

Comparison with experimental data

Pressure distribution The average pressure at the probe locations is presented in Figure 4.35. While the values are globally reasonably accurate and close to the experiments, they don't predict correctly the evolution on the blade surface. The pressure on the suction side of the blade is strongly overestimated by both turbulence models. The evolution on the pressure side of the blade and in the draft tube is however very similar to the numerical results obtained by Trivedi *et al.* [7], but in the guide vane passage the pressure drop is underestimated. While this leads to a better overall pressure drop, it falsifies the distribution of the losses on the different components.

Velocity profiles The time-averaged velocity profiles along the two lines at the runner outlet are shown in Figure 4.36. Figure 4.36a shows that almost a perfect match is obtained regarding the distribution of axial velocity below the runner. On the other hand, there is a considerable over-prediction of the swirl near the rotation axis, similar to what is observed for the mixing plane simulations at best efficiency point (Section 4.1.1). Near the draft tube wall, the predicted swirl corresponds well to the experimental observations. While both models predict well the axial velocity, the k-ω SSTF shows better agreement for the prediction of the tangential velocity. At the second measurement section (Figure 4.36b), both models strongly over-predict the recirculation zone below the hub. The profiles of tangential velocity show better agreement than at the first measurement section, but the swirl is still overestimated over the whole width of the runner outlet cone.

Pressure and torque fluctuations

Figure 4.37 shows the time evolution of the pressure probe values, while the frequency spectrum is shown in Figure 4.38. The frequency spectrum obtained from the experimental results is shown in Appendix F. The evolution in the vane-less space (Figure 4.37a) shows fluctuations which contain a basic oscillation frequency of 14.9 times the rotation frequency n. This is visible as a slight peak in the frequency spectrum, which is also found in the experimental results and corresponds to the blade passing frequency. The same frequency

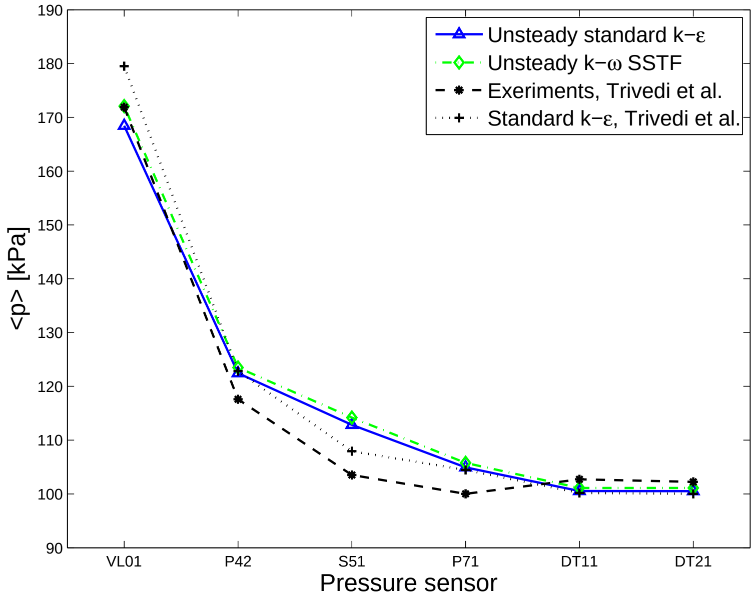

Figure 4.35: *Comparison of the time-averaged pressure values at several locations with experimental and simulated results by Trivedi et al. [7] at best efficiency point.*

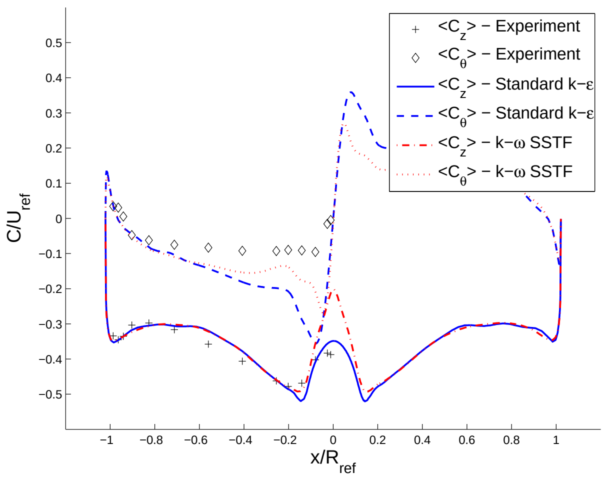

(a) *Time-averaged velocity profile at the runner outlet (line 1) at best efficiency point, compared with experimental results provided by the workshop committee [8].*

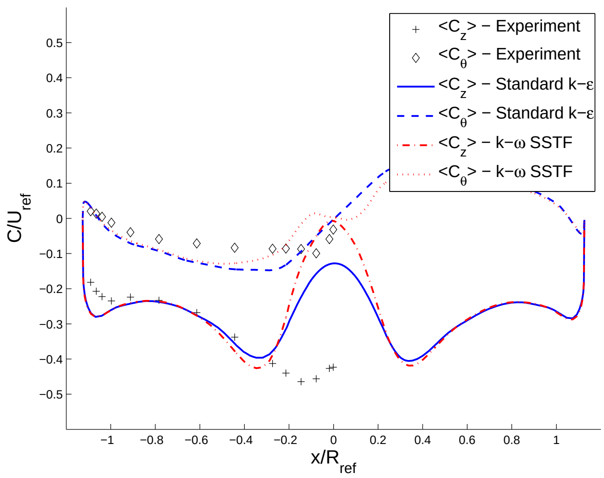

(b) *Time-averaged velocity profile at the runner outlet (line 2) at best efficiency point, compared with experimental results provided by the workshop committee [8].*

Figure 4.36: *Time-averaged velocity profiles at the runner outlet at best efficiency point. C_z denotes the axial velocity component and C_θ the tangential velocity component. Velocities are normalised by the circumferential reference velocity U_{ref}, and the x axis by the runner outlet radius R_{ref}.*

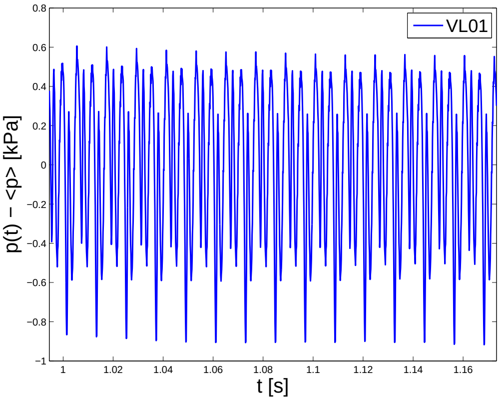

(a) *Time evolution of the pressure in the vane-less space (probe VL01) over one runner rotation at best efficiency point.*

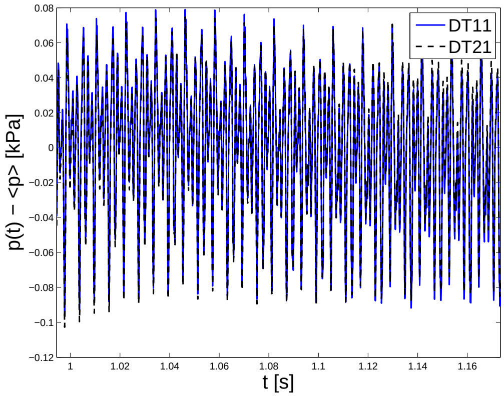

(b) *Time evolution of the pressure in the draft tube (probes DT11 and DT21) over one runner rotation at best efficiency point.*

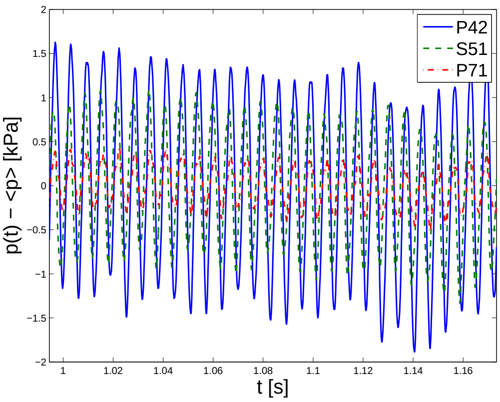

(c) *Time evolution of the pressure on the blade surface (probes P42, S51 and P71) over one runner rotation at best efficiency point.*

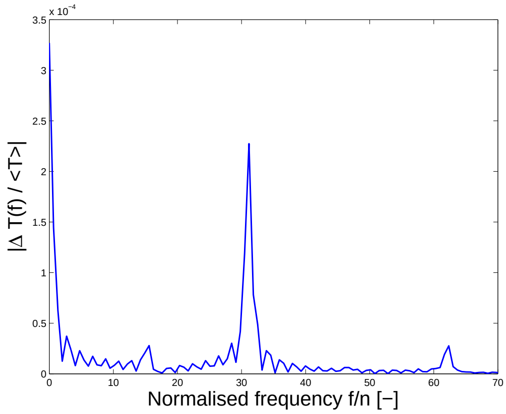

(d) *Frequency spectrum of the axial torque at best efficiency point, normalised by the runner rotation frequency.*

Figure 4.37: *Pressure and torque oscillations at best efficiency point.*

is present in the draft tube (Figure 4.37b). A harmonic corresponding to blades and splitter blades is found at $31.2n$, which experimentally is located at $29.6n$. The pressure on the blade surface (Figure 4.37c) shows a strong oscillation with $29.1n$. In the experimental data, this peak is located at $27.7n$, which corresponds to the blades passing the 28 guide vanes. A series of peaks on the blade surfaces located between $17.8n$ and $18n$ which is measured experimentally is not found in the simulations. On the other hand, the frequency located at $62.3n$ in the vane-less space and draft tube which is found in the numerical results (Figure 4.38) is not present in the measurements. Torque oscillations (Figure 4.37d) are observed with the main peak at $31.2n$ corresponding to the blade and splitter passage, and a lower amplitude at $15.6n$ corresponding to the blade passage. An additional peak is observed at $62.3n$, corresponding to the high-frequency pressure fluctuations on all sensors which are not observed experimentally.

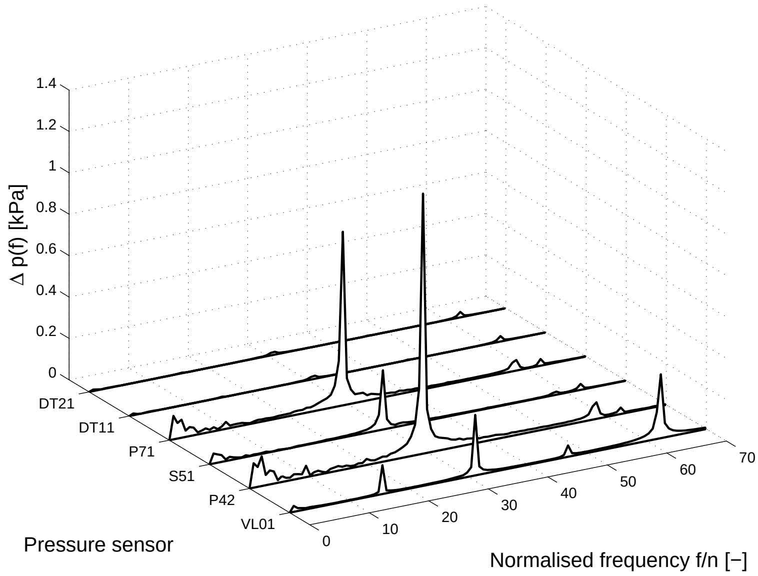

Figure 4.38: *Frequency spectrum of the pressure fluctuations at best efficiency point, normalised by the runner rotation frequency.*

4.2.2 Part load

Overview

At part load, a strong swirl is observed at the runner outlet, which is clearly visible in the streamlines (Figure 4.39). The mean distribution of pressure (Figure 4.40) and axial velocity (Figure 4.41a) show a large low-pressure recirculation zone near the axis of rotation, as it is observed with the steady-state simulations (Section 4.1.2). The vorticity contours (Figure 4.41b) show a strong rotation in the outer part of the draft tube and lower vorticity close to the rotation axis.

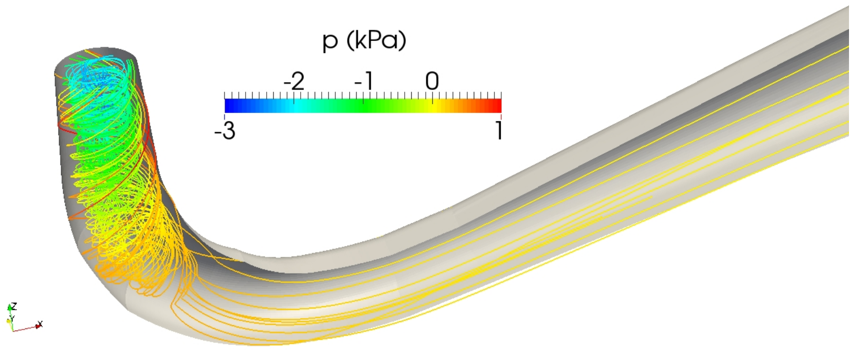

Figure 4.39: *Streamlines originating from a horizontal line at the runner outlet at part load.*

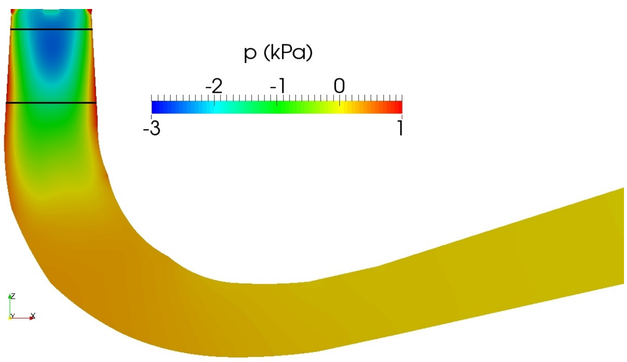

Figure 4.40: *Mean pressure distribution in the symmetry plane (*$y = 0$*) of the draft tube at part load.*

Iso-surfaces of the q-criterion near the runner inlet (Figure 4.42) show that separation occurs directly after the leading edge of the blades, and vortices are generated both near the shroud and near the hub. These structures are much stronger near the top and bottom walls of the guide vane passage, as it can be seen by comparing Figures 4.43, 4.44 and 4.45 which show contours of the q-criterion at different heights in the guide vane passage. While in Figure 4.44 hardly any structures are visible near the leading edges, they are easily observed in Figures 4.43 and 4.45. Figure 4.46 shows contours of the q-criterion near the runner outlet. The separation point is visible at the trailing edge of the splitter blades, and is slightly moved to the suction side. In the blade channel after the splitter blades, some perturbations are present which seem to be convected downstream from the leading edge or the guide vane cascade. Finally, strong separation is observed near the trailing edge of the blades on the suction side. Note the almost perfect symmetry of this pattern which occurs at the same location on all 15 blades.

Comparison with experimental data

Pressure distribution In contrast to the best efficiency point results, the simulations for part load show very good agreement with the simulations by Trivedi *et al.* [7] when it comes to pressure distribution in the turbine. Figure 4.47 shows the time-averaged pressure at the probe locations in comparison to the experimental and

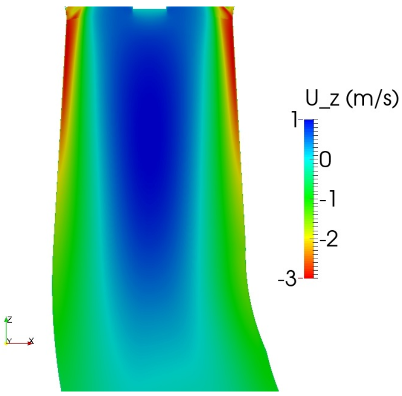

(a) *Mean distribution of axial velocity in the symmetry plane ($y = 0$) of the runner outlet cone at part load.*

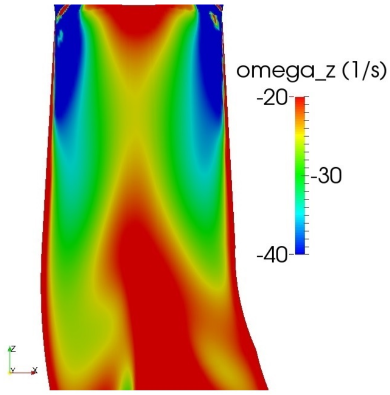

(b) *Instantaneous distribution of axial vorticity in the symmetry plane ($y = 0$) of the runner outlet cone at part load.*

Figure 4.41: *Flow field in the symmetry plane of the runner outlet cone at part load.*

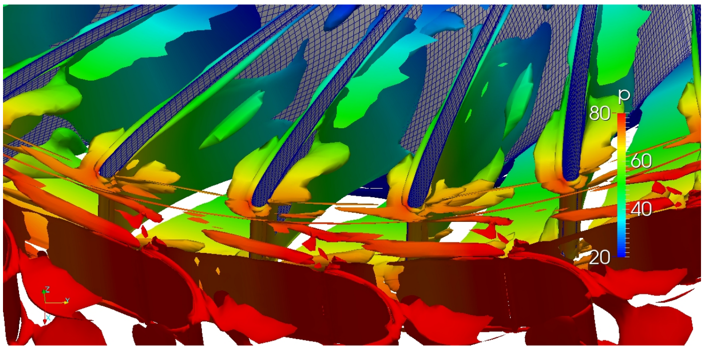

Figure 4.42: *Iso-surfaces of q-criterion at the runner inlet at part load.*

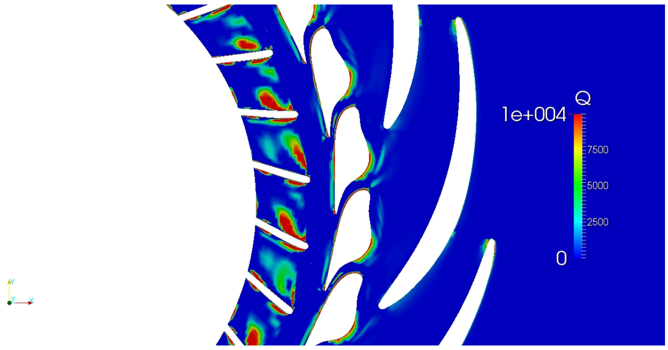

Figure 4.43: *Contours of q-criterion in the guide vane cascade ($z = 0.025m$) at part load.*

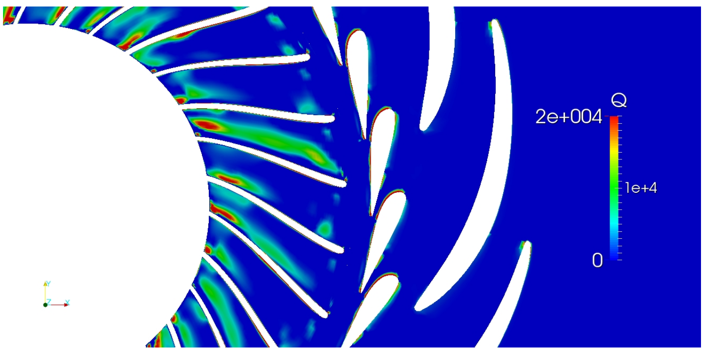

Figure 4.44: *Contours of q-criterion in the guide vane cascade ($z = 0m$) at part load.*

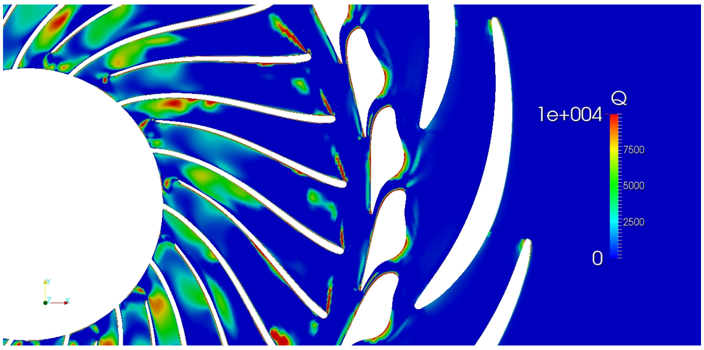

Figure 4.45: *Contours of q-criterion in the guide vane cascade ($z = -0.025m$) at part load.*

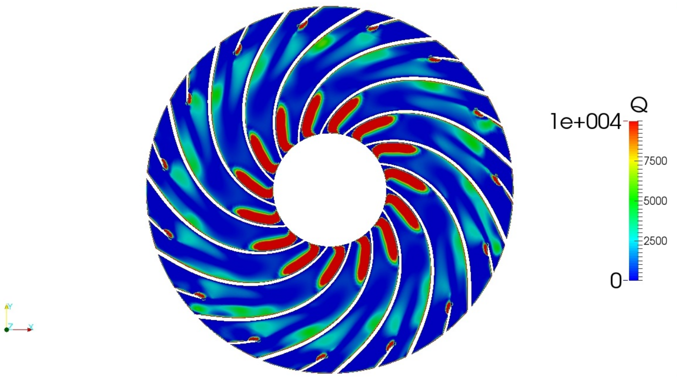

Figure 4.46: *Iso-surfaces of q-criterion near the runner outlet ($z = -0.16m$) at part load.*

numerical results from the paper. The most important difference takes place between the vane-less space and the runner blade. This leads to an overall pressure difference at the runner which is closer to the experimental measurements, but the losses in the guide vane cascade are not correctly predicted. This is most certainly caused by the bad convergence of the pressure, as the main problems in the mesh are located in the stay vane passage. The standard k-ε and the k-ω SSTF give almost identical pressure values.

Velocity profiles In Figure 4.48, the time-averaged velocity profiles at the runner outlet are shown. At the first measurement line (Figure 4.48a) qualitatively good agreement with the experimental measurements is obtained. The shape of the axial velocity profile is well predicted. The swirl near the draft tube wall is slightly underestimated, but the qualitative shape of the profile is satisfying. However, the second measurement line (Figure 4.48b) shows a considerable difference. While the axial velocity is once again well predicted, the swirling motion is strongly under-predicted by the standard k-ε. The k-ω SSTF model shows better agreement, but still underestimates the amount of swirl. This could be a sign that the flow is not sufficiently developed, which should be further investigated.

Pressure and torque fluctuations

The time evolution of the pressure probe values is shown in Figure 4.49, while Figure 4.50 shows the corresponding frequency spectrum. The frequency spectrum obtained from the experimental results is shown in Appendix F. In the vane-less space (Figure 4.49a), the blade-passing frequency is observed at $15.4n$, with the experiments showing it at $15n$. The blade and splitter passing frequency, which in the experiment is exactly at $30n$, is found at $30.77n$. The draft tube probes (Figure 4.49b) show the blade passing frequency at $15.4n$ which is located at 14.8 in the measurements, and the blade and splitter frequency at $30.8n$ which is present in the experiments with two peaks at $29.55n$ and at $30n$. The harmonic at $46.1n$ in the numerical results is measured at $44.3n$ in the experiments. A low frequency oscillation in the draft tube is observed at $0.27n$ in the experiments, while the numerical results show one at $0.5n$. However, the peak is very weak and no clear single frequency is present. This is consistent with the observation made by Dörfler *et al.* [36, pp. 40-41] that the vortex rope is replaced by random pulsations at very low part load. On the blade surface (Figure 4.49c), the guide vane

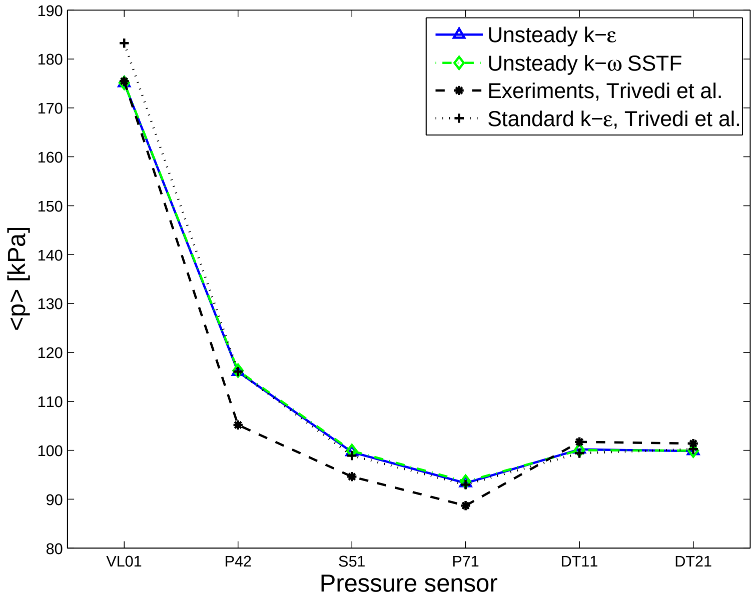

Figure 4.47: *Comparison of the time-averaged pressure values at several locations with experimental and simulated results at part load.*

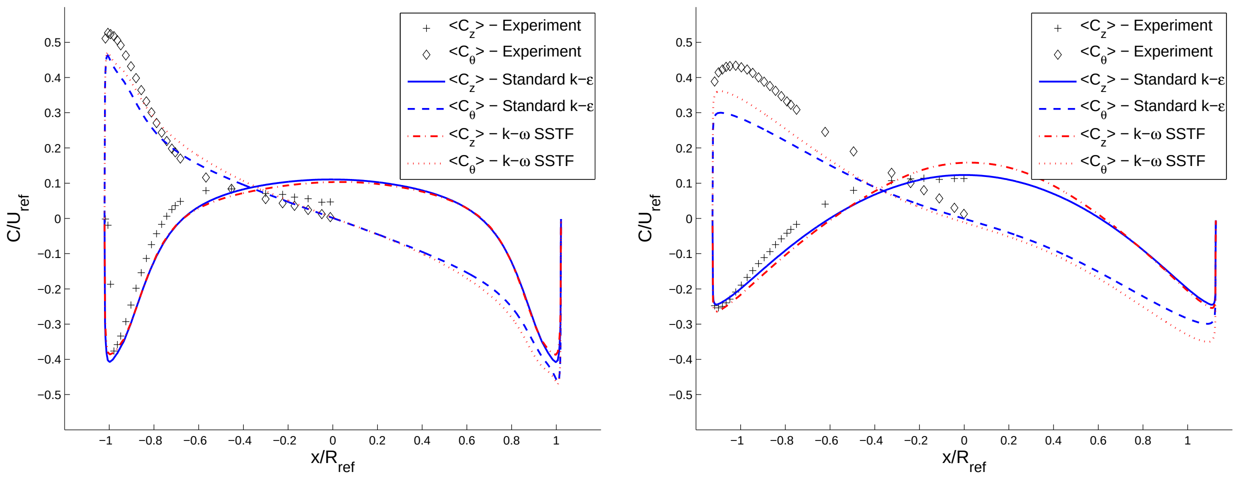

(a) *Time-averaged velocity profile at the runner outlet (line 1) at part load.*

(b) *Time-averaged velocity profile at the runner outlet (line 2) at part load.*

Figure 4.48: *Time-averaged velocity profiles at the runner outlet at part load. C_z denotes the axial velocity component and C_θ the tangential velocity component. Velocities are normalised by the circumferential reference velocity U_{ref}, and the x axis by the runner outlet radius R_{ref}.*

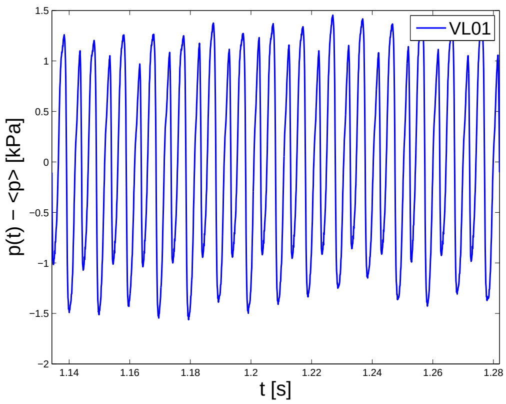

(a) *Time evolution of the pressure in the vaneless space (probe VL01) over one runner rotation at part load.*

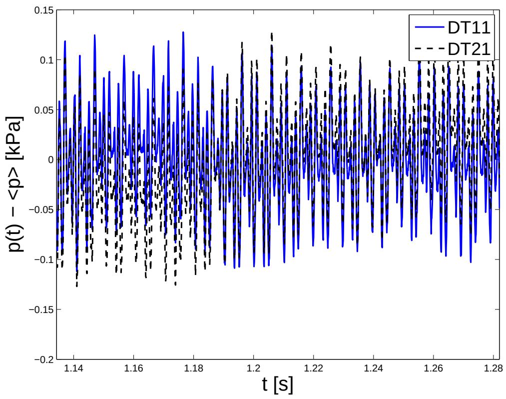

(b) *Time evolution of the pressure in the draft tube (probes DT11 and DT21) over one runner rotation at part load.*

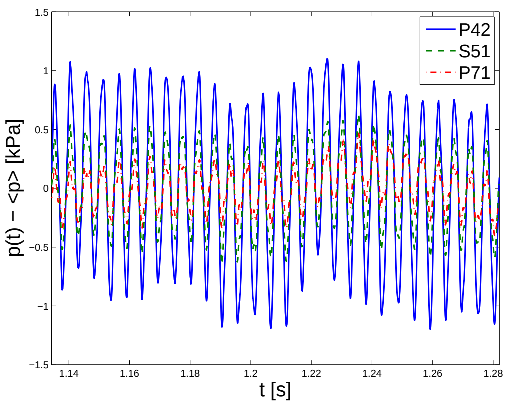

(c) *Time evolution of the pressure on the blade surface (probes P42, S51 and P71) over one runner rotation at part load.*

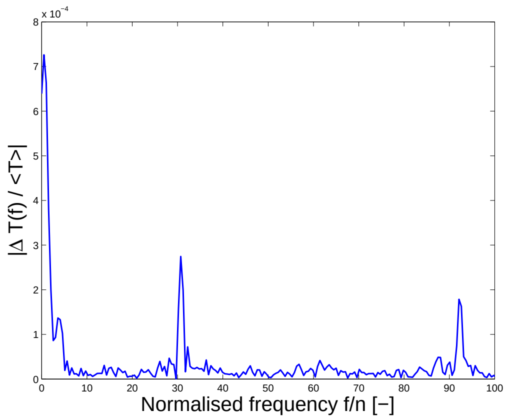

(d) *Frequency spectrum of the axial torque at part load, normalised by the runner rotation frequency.*

Figure 4.49: *Pressure and torque oscillations at part load.*

passing frequency is at $28.7n$, while the measurements locate it exactly at $28n$ with a second peak at $29.55n$ which is not observed numerically. The experiments also show a strong peak at $44.3n$, that is far weaker and slightly shifted to $46.1n$ in the numerical results.

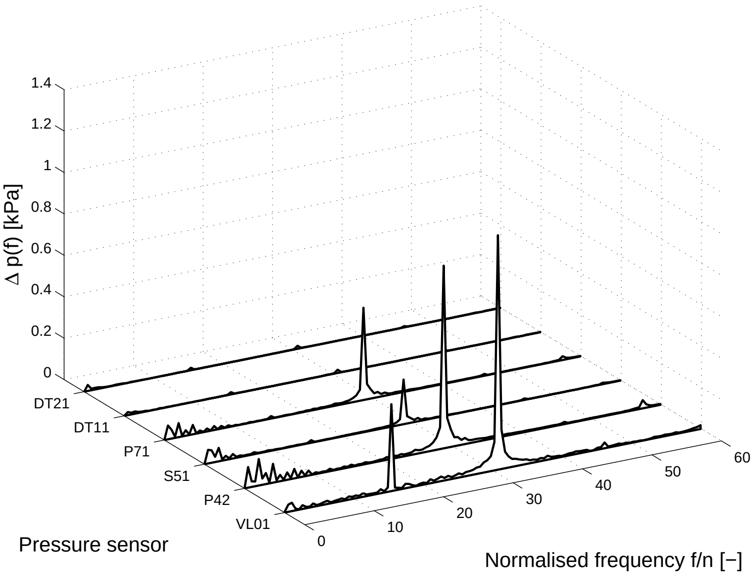

Figure 4.50: *Frequency spectrum of the pressure fluctuations at part load, normalised by the runner rotation frequency.*

4.2.3 High load

Overview

In Figure 4.51, the streamlines show a strong swirl at the axis of rotation with lower pressure, as it can be seen in the pressure contours on Figure 4.52. The contours of axial vorticity (Figure 4.53a) confirm the strong swirling motion in the counter-clockwise direction, while vorticity in the remaining part of the draft tube is relatively low. Originating from the hub, a zone with very high axial velocity is observed (Figure 4.53b) while the outer and central part of the flow are at lower axial velocity.

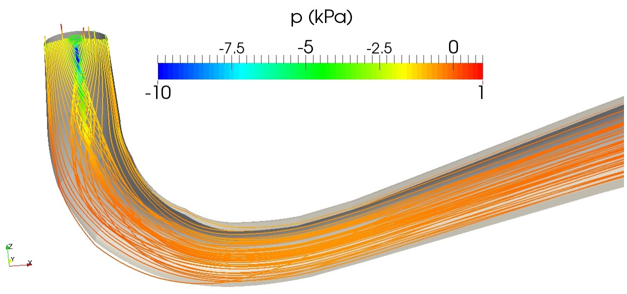

Figure 4.51: *Streamlines originating from a horizontal line at the runner outlet at high load.*

On Figure 4.54, iso-surfaces of q-criterion show that strong vortices originate from both ends of the blade leading edges. These structures are also visible on the contours of q-criterion in the guide vane passage and runner inlet (Figure 4.55). Separation is observed behind the leading edge of the blades and splitter blades on the suction side. In addition, strong perturbations are seen starting from the pressure side of the guide vanes that are convected downstream into the runner inlet. These structures are originating from the bulge on both ends of the guide vanes which is used for the regulating mechanism.

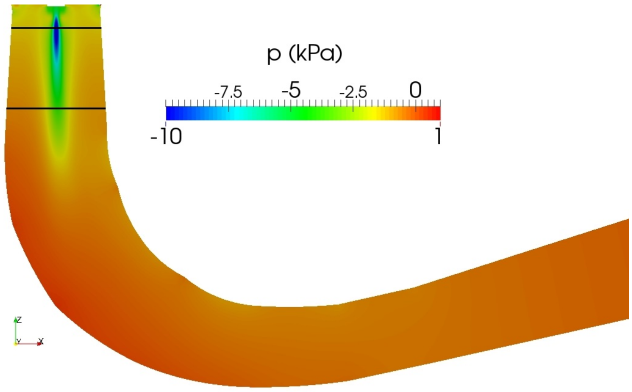

Figure 4.52: *Pressure distribution in the symmetry plane ($y = 0$) of the draft tube at high load.*

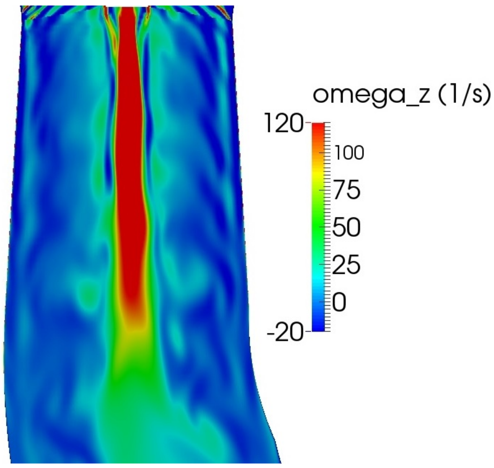

(a) *Distribution of axial vorticity in the symmetry plane ($y = 0$) of the runner outlet cone at high load.*

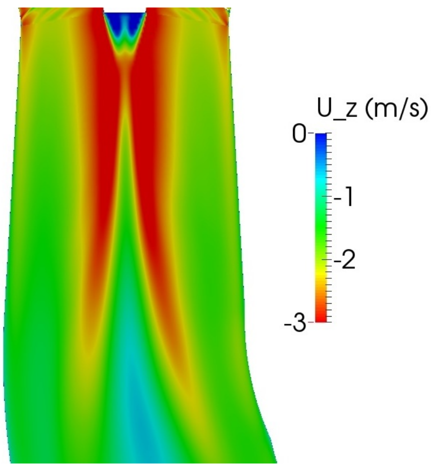

(b) *Distribution of axial velocity in the symmetry plane ($y = 0$) of the runner outlet cone at high load.*

Figure 4.53: *Flow field in the symmetry plane of the runner outlet cone at high load.*

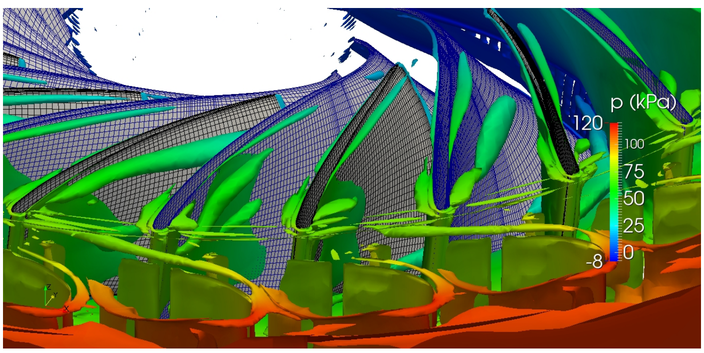

Figure 4.54: *Iso-surfaces of q-criterion at the runner inlet at high load.*

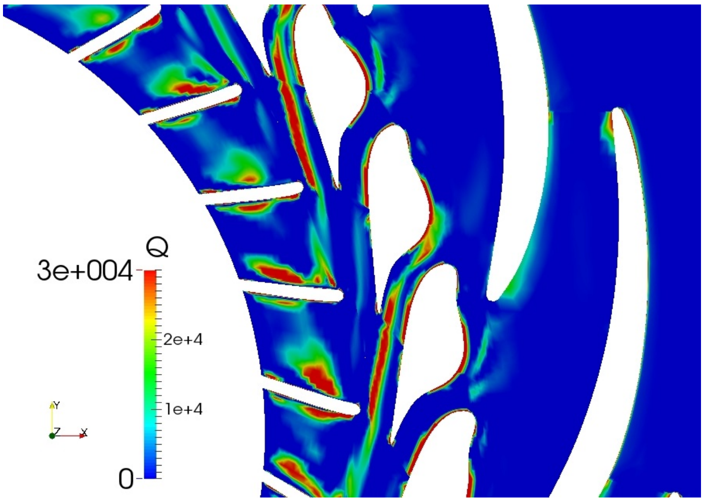

Figure 4.55: *Contours of q-criterion in the guide vane cascade ($z = 0.025m$) at high load.*

Comparison with experimental data

Pressure distribution The time-averaged pressure values at the probe locations (Figure 4.56) show good agreement with the experimental and numerical results by Trivedi *et al.* [7]. The largest difference occurs between the vane-less space and the runner, where the pressure drop is underestimated. In all other probe locations, the numerical values agree well but don't match the experimental results exactly, in particular in the draft tube, similarly to what is observed at the other operating points.

Velocity profiles Figure 4.57 shows the velocity profiles at the runner outlet. At the first measurement line (Figure 4.57a), the swirl is slightly overestimated but the qualitative shape of the tangential velocity profile corresponds to the experimental results. The agreement is better at the second line (Figure 4.57b), but the swirl is still overestimated in the simulations. Near the axis of rotation, the measurements show a zone of very strong swirl which is not sufficiently captured numerically. At both measurement lines the axial velocity is well predicted, except for the recirculation zone below the hub which is strongly overestimated, as it is the case at best efficiency point (Section 4.2.1).

Pressure and torque fluctuations

Figure 4.58 shows the time evolution of the pressure values at high load. The numerical frequency spectrum is presented in Figure 4.59, while the frequency spectrum obtained from the experimental results is shown in Appendix F. In the vane-less space, the blade and splitter passing frequencies are shifted from their expected values of $15n$ and $30n$ to $14.1n$ and $28.2n$ respectively. In the pressure measurements, these frequencies are not observed. The blade and splitter frequency is also observed in the draft tube at $28.2n$. On the blade surface, the guide vane passing frequency is at $26.3n$, while experimentally two peaks are observed at $28n$ and $30n$ respectively. The experimental frequencies at $48.7n$ are not present in the simulations. On the other hand, the peak at $56.4n$ in the vane-less space is not present in the measurement results.

4.2.4 Wall $y+$ values

Similarly to the mixing plane simulations, very low and excessively high y^+ values appear because the mesh size is not suitable for the simulated flow in certain regions. Due to the size and complexity of the full mesh and the large computational effort, no mesh refinement is done for the unsteady simulations. The y^+-values for the unsteady simulations are given in Appendix C.3.

4.2.5 Convergence

Despite ramping-up of the flow rate and gradual modifications of the numerical settings, the convergence of the pressure field remains unsatisfactory. The obtained solution is however qualitatively and quantitatively

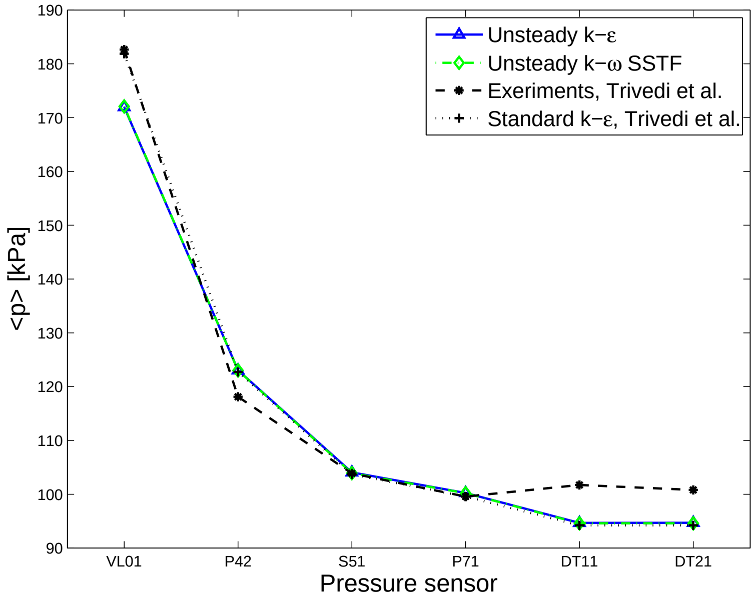

Figure 4.56: *Comparison of the time-averaged pressure values at several locations with experimental and simulated results by Trivedi et al. [7] at high load.*

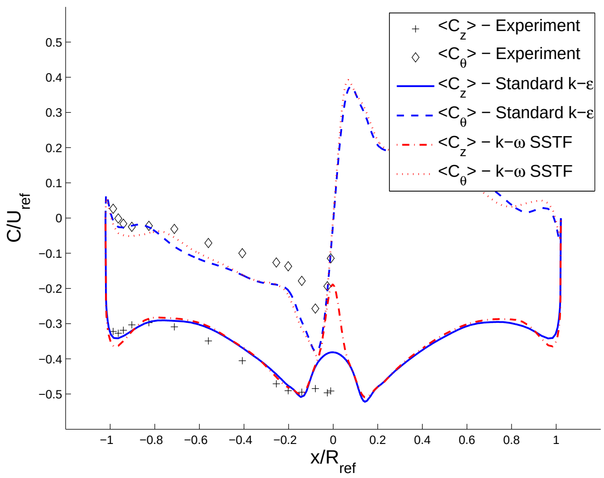

(a) *Time-averaged velocity profile at the runner outlet (line 1) at high load.*

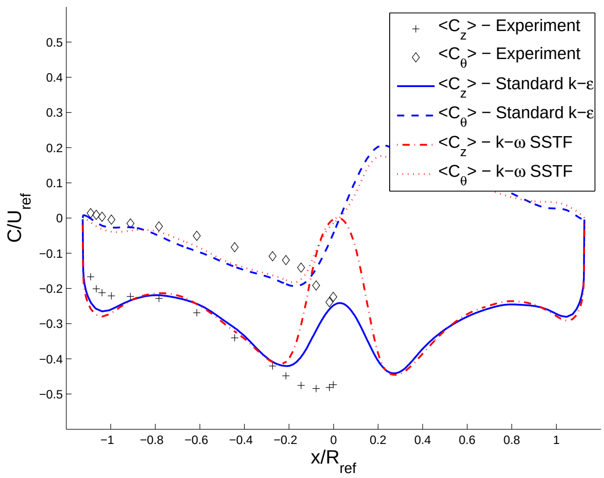

(b) *Time-averaged velocity profile at the runner outlet (line 2) at high load.*

Figure 4.57: *Time-averaged velocity profiles at the runner outlet at high load.* C_z *denotes the axial velocity component and* C_θ *the tangential velocity component. Velocities are normalised by the circumferential reference velocity* U_{ref}*, and the* x *axis by the runner outlet radius* R_{ref}*.*

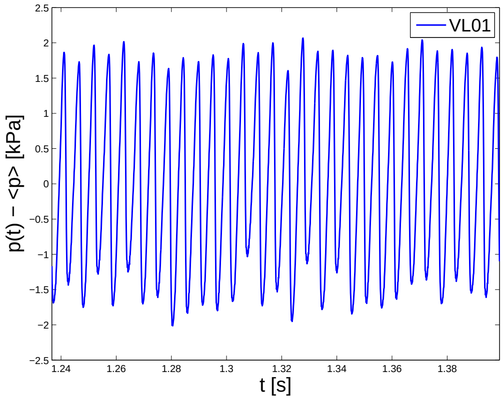

(a) *Time evolution of the pressure in the vaneless space (probe VL01) over one runner rotation at high load.*

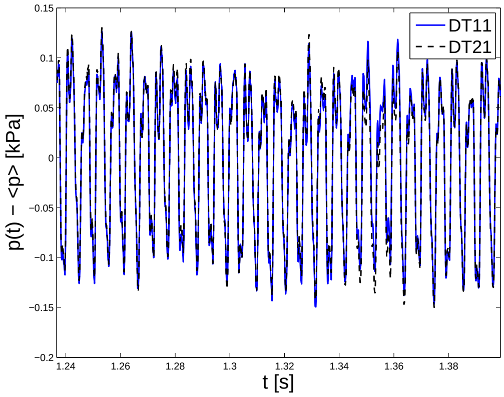

(b) *Time evolution of the pressure in the draft tube (probes DT11 and DT21) over one runner rotation at high load.*

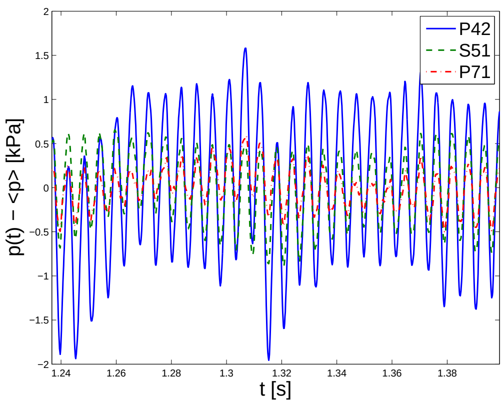

(c) *Time evolution of the pressure on the blade surface (probes P42, S51 and P71) over one runner rotation at high load.*

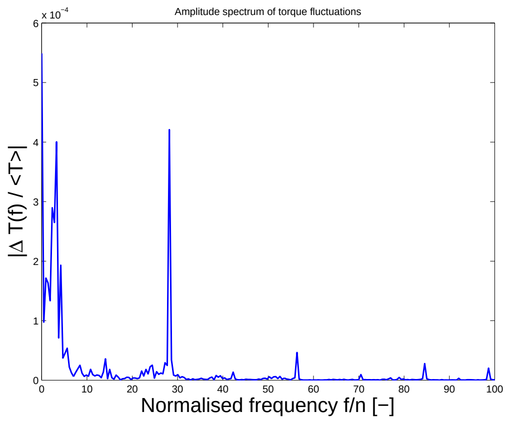

(d) *Frequency spectrum of the axial torque at high load, normalised by the runner rotation frequency.*

Figure 4.58: *Pressure and torque oscillations at high load.*

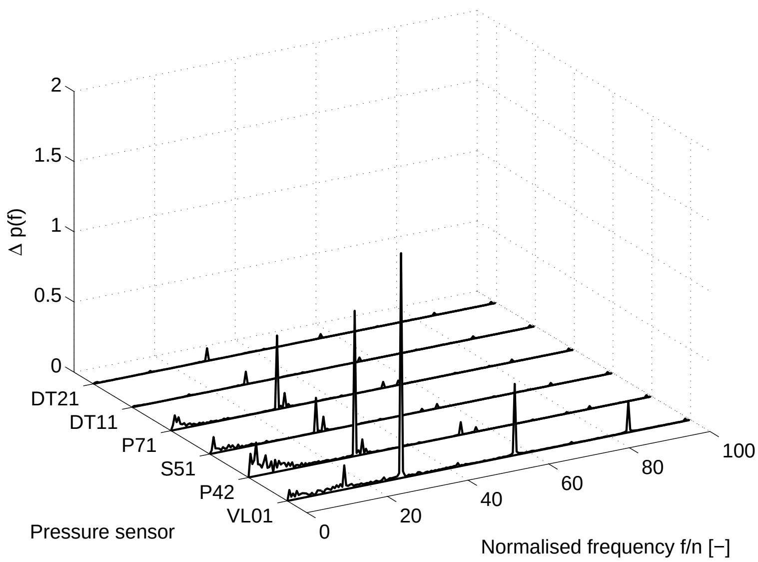

Figure 4.59: *Frequency spectrum of the pressure fluctuations at high load, normalised by the runner rotation frequency.*

acceptable despite the insufficient convergence. A particularly sensitive point is the region between the stay vanes and the guide vanes, where large velocities were obtained during early iterations and divergence was most likely to start. This problem is most certainly linked to the poor mesh quality in this region (see Section 3.5.2). A detailed evaluation of the convergence behaviour as well as the evolution of global quantities is given in Appendix B.2. The computation time on 128 processors for one second of simulated time is 330 hours. For a simulation at best efficiency point where the flow is ramped up within 0.1 seconds, stabilised over five runner rotations and then simulated over one runner rotation, the overall computational time is 367 hours.

4.3 Unsteady simulations with variations in rotational speed

4.3.1 Choice of the oscillation

In order to mimic the behaviour of the runner during oscillations of the shaft, the main frequency of the torque oscillations $f = 31.17 \cdot n = 174.24Hz$ (Section 2.4) is taken as the frequency for the oscillations in rotational speed. As very little is known about the mechanical properties of the turbine, such as inertia of the runner or stiffness of the shaft, an arbitrary oscillation with this frequency is chosen. The instantaneous rotational speed is then

$$n(t) = n_0 + \tilde{n}(t) = n_0 + \hat{n}\sin(\omega(t + t_0)), \tag{4.1}$$

with the pulsation

$$\omega = 2\pi f = 1094.78s^{-1} \tag{4.2}$$

and the time shift

$$t_0 = \frac{\pi}{2\omega} = 1.4348 \cdot 10^{-3}s. \tag{4.3}$$

The amplitude of the runner speed oscillation is chosen arbitrarily to be $\hat{n} = 0.05n_0 = 0.2795s^{-1}$. Using equation 2.21, the amplitude of the angular runner oscillation can be calculated as

$$\hat{\theta} = \hat{n}\frac{2\pi}{\omega} = 0.0016rad = 0.0919°. \tag{4.4}$$

4.3.2 Pressure and torque fluctuations

As shown in Figures 4.60a and 4.60c, the runner oscillations cause strong pressure fluctuations both in the vane-less space and on the runner blades, which are one order of magnitude higher than without runner oscillations. In the draft tube (Figure 4.60b) the fluctuations are weaker, but still twice as high as without oscillations. The frequency spectrum (Figure 4.61) shows that the strong pressure fluctuations occur at $29.7n$. The guide vane passing frequency on the blades and the blade passing frequency in the vane-less space remain unchanged but are negligible compared to the fluctuations caused by the runner oscillations. In the frequency spectrum of the torque fluctuations in Figure 4.60d, the only frequency which is present is at $29.7n$ and thus caused by the pressure fluctuations on the blade surface.

4.3.3 Added coefficients

As only one dominant frequency is observed in the torque fluctuations (Figure 4.60d) which is in phase with the angular oscillation of the runner, the added coefficients can easily be extracted using equation 2.26 and the definition of the force coefficients in phase and out of phase (equations 2.27 and 2.28). The coefficient of forces out of phase is $C_o = 0$, while the coefficient of forces in phase C_i is

$$C_i = (k' - I'\omega^2)\hat{\theta} = \hat{T} = 336.4Nm. \tag{4.5}$$

The oscillating system including the added torque can be expressed as

$$I\ddot{\tilde{\theta}} + c\dot{\tilde{\theta}} + k\tilde{\theta} + C_i\tilde{\theta} = 0. \tag{4.6}$$

If the expression of the chosen basic oscillation (equation 2.18) is introduced and the terms in phase and out of phase are regrouped, this expression becomes

$$-I\omega^2\hat{\theta}\sin(\omega t) + c\hat{\theta}\omega\cos(\omega t) + (k - I\omega^2 + C_i)\hat{\theta}\sin(\omega t) = 0. \tag{4.7}$$

This means that the fluid loading adds stiffness to and/or removes inertia from the oscillating runner, while no added damping is present. The simulated oscillations are thus not prone to divergence, as this would only occur if the overall stiffness was reduced to zero or negative damping was added to the system [20].

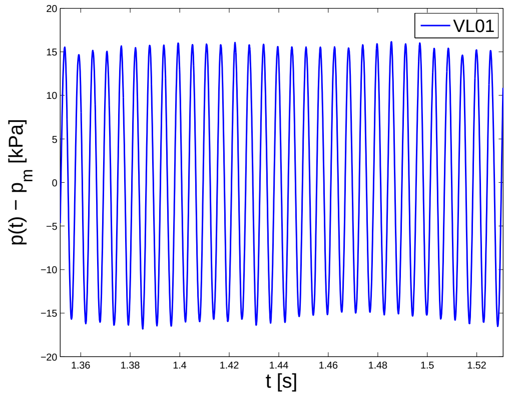

(a) *Time evolution of the pressure in the vaneless space (probe VL01) over one runner rotation at best efficiency point with oscillations in runner rotational speed.*

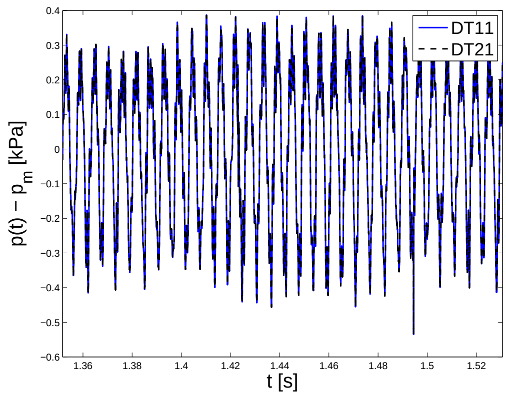

(b) *Time evolution of the pressure in the draft tube (probes DT11 and DT21) over one runner rotation at best efficiency point with oscillations in runner rotational speed.*

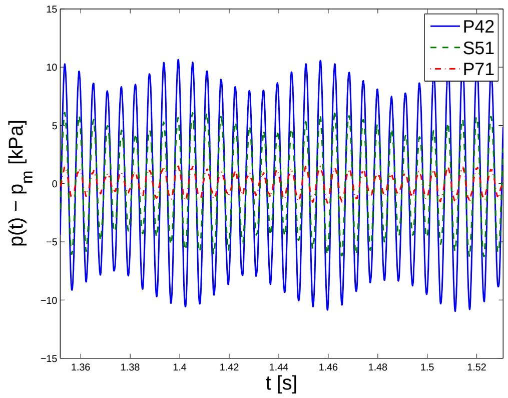

(c) *Time evolution of the pressure on the blade surface (probes P42, S51 and P71) over one runner rotation at best efficiency point with oscillations in runner rotational speed.*

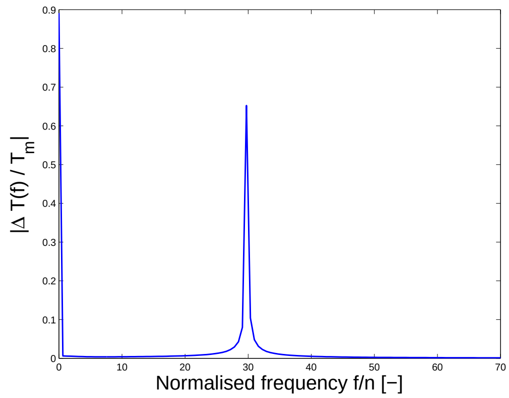

(d) *Frequency spectrum of the axial torque at best efficiency point with oscillations in runner rotational speed, normalised by the runner rotation frequency.*

Figure 4.60: *Pressure and torque oscillations at best efficiency point with oscillations in runner rotational speed.*

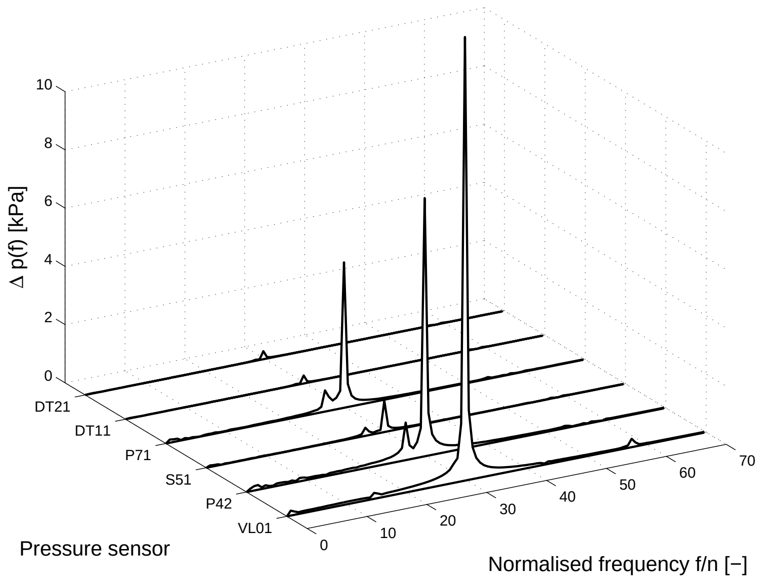

Figure 4.61: *Frequency spectrum of the pressure fluctuations at best efficiency point with oscillations in runner rotational speed, normalised by the mean runner rotation frequency.*

5 Future work

5.1 Mesh improvement

In Section 3.5 it was pointed out that several issues are present in the mesh which was supplied by the workshop organisers and is currently used. Improving the mesh quality and solving the main issues should be the first step for any future project dealing with this turbine geometry. The mesh topology in the stay vane passage doesn't allow a smooth transition between small and larger cells and must therefore be changed. Furthermore, the size of the boundary layer mesh in certain regions (guide vane surface, trailing edge of the blades, below the hub) is not suitable and needs to be modified in order to respect the criteria for y^+ - values.

5.2 Additional turbulence models and validation

Several different turbulence models have been employed within the scope of this thesis. However, a lot of options that could be of interest have not been examined. A more exhaustive investigation of the performance of recently developed turbulence models and their influence on the solution could be a potential research area for the continuation of the work. The complete EARSM was only partly implemented and has not been used, and the linear EARSM has not been validated in its current version in OpenFOAM. Validation on simple cases, where experimental data and numerical results from other methods are available, would be necessary in order to exclude possible mistakes in the implementation. The implemented equations should also be verified independently to avoid potential programming mistakes in the code.

5.3 Transient operation

In the scope of the present work, only steady turbine operation was considered. In view of the continuation of the Francis-99 workshop series, investigating transient operation such as start-up, change of operating point or runaway during an electric power interruption would be of interest. The flexibility of OpenFOAM for user-created functions makes it an appropriate tool for this type of simulations.

5.4 Further investigation of runner oscillations, deformation analysis of the runner blades and cavitation

Only one particular type of runner oscillations has been examined until now, and the runner was assumed to be completely rigid. In order to obtain a more detailed picture of the dynamical behaviour of the turbine, possible oscillations of the runner as well as the resulting deformations of the blades should be examined, allowing to gain insight into more complex fluid-structure interaction phenomena that might occur. Furthermore, the issue of cavitation has not at all been addressed in the scope of this work. Zhang and Zhang [14] used OpenFOAM to model cavitation in a Francis runner, and a similar procedure could be envisaged for the Francis-99 turbine. In this context, an additional operating point at upper part load could be of interest, where the characteristic vortex rope should appear. Investigating cavitation in relation with runner oscillations at off-design conditions could be of great interest.

6 Conclusions

In the scope of the present work, a large number of simulations were conducted which allowed to obtain a good understanding of the flow in the Francis-99 turbine model. Steady and unsteady simulations were performed at three different operating points. On one hand, the mixing plane simulations gave an accurate and quick prediction of the flow field in the turbine. In addition, unsteady simulation were performed to obtain a time-resolved solution of the flow. While the steady-state simulations use multiple rotating frames of reference, the unsteady simulations use a rotating mesh to represent the runner rotation. A large number of turbulence models was used, and the resulting data was compared to experimental measurements and simulations by other authors. Furthermore, the feasibility of unsteady simulations with sinusoidal runner oscillations was investigated and the resulting torque fluctuations were extracted.

The steady-state mixing plane simulations give an accurate prediction of the pressure distribution and velocity profiles at all operating points, except for best efficiency point where the swirl at the runner outlet is over-estimated. This shows that the mixing plane as it is implemented in OpenFOAM is an appropriate tool to predict the mean flow in a Francis turbine. Furthermore, the mixing plane simulations are just as accurate regarding the prediction of the mean velocity and pressure in the turbine. However, the present steady-state simulations overestimate the hydraulic efficiency of the turbine. A possible reasons for this is the choice of the inlet boundary condition in directly before the guide vanes, which means that the losses in the spiral casing and stay vane passage are neglected. The efficiency prediction is satisfying with the unsteady simulations, and while there is some over-prediction compared to the experiment, the results are comparable to simulations by other authors. Both types of simulations predict however a strong swirl at the runner outlet at best efficiency point which is similar to high load operation and is not observed experimentally. Time-resolved data from the unsteady simulations allowed to find the main frequencies of rotor-stator interaction in the turbine. The obtained frequency spectrum shows good agreement with the measured data, although most peaks contain a small frequency shift in the numerical results. Furthermore, no periodic low-frequency fluctuations in the draft tube at off-design were identified. A longer observation period of several runner rotations could lead to a more complete picture of the oscillating forces on the runner.

The linear EARSM was successfully implemented and tested on the mixing plane case at all operating points. In its current implementation it proved however to be inferior to classical models on this particular geometry, and should be validated on simple test cases before any further use in order to exclude possible programming errors. In a future step, the complete EARSM, which is only partly implemented and not yet functional, should also be tested and validated. For unsteady simulation, the k-ω SSTF model was implemented and gave in general very similar results to the standard k-ε model, but showed better agreement with the experimental velocity profiles. While with the steady-state simulations large differences occurred both regarding the efficiency prediction and the velocity profiles depending on the turbulence model that is chosen, only slight differences between the standard k-ε and the k-ω SSTF model are observed with the unsteady simulations. In both cases, the pressure distribution in the turbine is not considerably affected by the choice of the turbulence model. The largest differences between the turbulence models and compared to the experimental results occur in the region below the hub and in the runner outlet cone, affecting the resulting efficiency.

Oscillations in rotational speed at the frequency of the main torque oscillations were simulated at best efficiency point and the coefficients of added torque were extracted. As no information is available on the mechanical properties of the turbine at this stage, the amplitude and phase of the runner oscillations were chosen arbitrarily. No experimental or numerical data is currently available to verify the accuracy of the results. The simulated oscillations can however give an indication of what is possible with the methodology and software that were used in this thesis.

To conclude, it can be said that while there remains room for improvements, further research and continuation of the work, the main goals of the present thesis have been achieved. The basis for a meaningful contribution to the Francis-99 workshop is laid, and promising results were obtained using different simulation strategies.

Göteborg, 28$^{\text{th}}$ of September 2014

Lucien Stoessel

References

[1] Avellan, F. *Hydraulic Turbomachines - Course Notes.* École polytechnique fédérale de Lausanne. Sept. 2012.

[2] Nicolet, C. "Hydroacoustic modelling and numerical simulation of unsteady operation of hydroelectric systems". PdD Thesis. Lausanne, Switzerland: École polytechnique federale de Lausanne, 2007.

[3] Shingai, K., Okamoto, N., Tamura, Y., and Tani, K. Long-Period Pressure Pulsation Estimated in Numerical Simulations for Excessive Flow Rate Condition of Francis Turbine. *Journal of Fluids Engineering* **136(7)**.071105, July 2014. DOI: `10.1115/1.4026584`.

[4] Keck, H. and Sick, M. Thirty years of numerical flow simulation in hydraulic turbomachines. *Acta Mechanica* **201(1)**, Dec. 2008, 211–229. DOI: `10.1007/s00707-008-0060-4`.

[5] Nicolet, C., Zobeiri, A., Maruzewski, P., and Avellan, F. Experimental Investigations on Upper Part Load Vortex Rope Pressure Fluctuations in Francis Turbine Draft Tube. *International Journal of Fluid Machinery and Systems* **4(1)**, Jan. 2011, 179–190. DOI: `10.5293/IJFMS.2011.4.1.179`.

[6] Mazzouji, F. and Leroy, P. "CFD & Francis turbine design". Guest Lecture at EPFL. Nov. 2011.

[7] Trivedi, C., Cervantes, M. J., Gandhi, B., and Dahlhaug, O. G. Experimental and Numerical Studies for a High Head Francis Turbine at Several Operating Points. *Journal of Fluids Engineering* **135 (11)**.111102, Nov. 2013, 1–17. DOI: `10.1115/1.4024805`.

[8] *Francis-99 Workshop.* Last verified 16th of July 2014. Luleå University of Technology. URL: `http://www.ltu.se/research/subjects/Stromningslara/Konferenser/Francis-99?l=en`.

[9] Nilsson, H. Evaluation of OpenFOAM for CFD of turbulent flow in water turbines. *23th IAHR Symposium on Hydraulic Machinery and Systems*, Oct. 2006.

[10] Petit, O. "Towards Full Predictions of the Unsteady Incompressible Flow in Rotating Machines, Using OpenFOAM". PhD Thesis. Göteborg, Sweden: Department of Fluid Dynamics, Chalmers University of Technology, 2012.

[11] Javadi, A. "Time-accurate Turbulence Modeling of Swirling Flow for Hydropower Application". Licentiate Thesis. Göteborg, Sweden: Department of Fluid Dynamics, Chalmers University of Technology, 2014.

[12] Page, M., Beaudoin, M., and Giroux, A.-M. Steady-state Capabilities for Hydroturbines with OpenFOAM. *International Journal of Fluid Machinery and Systems* **4(1)**, Jan. 2011, 161–171. DOI: `10.1088/1755-1315/12/1/012076`.

[13] Petit, O., Bosioc, A. I., Nilsson, H., Muntean, S., and Susan-Resiga, R. F. A swirl generator case study for OpenFOAM. *25th IAHR Symposium on Hydraulic Machinery and Systems* **12(1)**.012056, 2010.

[14] Zhang, H. and Zhang, L. Numerical simulation of cavitating turbulent flow in a high head Francis turbine at part load operation with OpenFOAM. *Procedia Engineering* **31**, 2012, 156–165. DOI: `10.1016/j.proeng.2012.01.1006`.

[15] Susan-Resiga, R., Muntean, S., Stein, P., and Avellan, F. Axisymmetric Swirling Flow Simulation of the Draft Tube Vortex in Francis Turbines at Partial Discharge. *International Journal of Fluid Machinery and Systems* **2(4)**, Oct. 2009, 295–302. DOI: `10.5293/IJFMS.2009.2.4.295`.

[16] Maruzewski, P., Hayashi, H., Munch, C., Yamaishi, K., Hashii, T., Mombelli, H. P., Sugow, Y., and Avellan, F. Turbulence modeling for Francis Turbine water passages simulation. *IOP Conference Series: Earth and Environmental Science* **12(1)**, 2010, 1–9. DOI: `10.1088/1755-1315/12/1/012070`.

[17] Wu, Y., Liu, S., Wu, X., Dou, H., Zhang, L., and Tao, X. Turbulent flow computation through a model Francis turbine and its performance prediction. *IOP Conference Series: Earth and Environmental Science* **12**.012004, 2010. DOI: `10.1088/1755-1315/12/1/012004`.

[18] Nilsson, H. Simulations of the vortex in the Dellenback abrupt expansion, resembling a hydro turbine draft tube operating at part load. *4th OpenFOAM Workshop*, June 2009.

[19] *IEC 60193 Hydraulic tturbine, storage pumps and pump-turbines - Model acceptance tests.* Geneva, Switzerland: International Electrotechnical Comission, 1999.

[20] Spadoni, A. *Aeroelasticity and fluid-structure interaction - Course Notes.* Ecole polytechnique fédérale de Lausanne. Sept. 2013.

[21] Nicolet, C. *Hydrodynamique acoustique - Course Notes.* École polytechnique fédérale de Lausanne. Feb. 2012.

[22] Pennacchi, P., Chatterton, S., and Vania, A. Modeling of the dynamic response of a Francis turbine. *Mechanical Systems and Signal Processing* **29**, May 2012, 107–119. DOI: `10.1016/j.ymssp.2011.05.012`.

[23] Gyllenram, W. and Nilsson, H. Very large eddy simulation of draft tube flow. *23th IAHR Symposium on Hydraulic Machinery and Systems*, Oct. 2006.

[24] Beaudoin, M. and Jasak, H. "Development of a Generalized Grid Interface for Turbomachinery simulations with OpenFOAM". Open Source CFD International Conference 2008. Berlin, Germany, 2008.

[25] Petit, O., Page, M., Beaudoin, M., and Nilsson, H. The ERCOFTAC centrifugal pump OpenFOAM case-study. *3rd IAHR International Meeting of the Workgroup on Cavitation and Dynamic Problems in Hydraulic Machinery and Systems*, Oct. 2009.

[26] Denton, J. The Calculation of Three-Dimensional Viscous Flow Through Multistage Turbomachines. *Journal of Turbomachinery* **114(1)**, Jan. 1992, 18–26.

[27] Brandvik, T. and Pullan, G. An accelerated 3D Navier-Stokes solver for flows in turbomachines. *Journal of turbomachinery* **133(2)**.021025, Oct. 2010. DOI: 10.1115/1.4001192.

[28] Páscoa, J. C., Xisto, C., and Göttlich, E. Performance assessment limits in transonic 3D turbine stage blade rows using a mixing-plane approach. *Journal of Mechanical Science and Technology* **24**, June 2010, 2035–2042. DOI: 10.1007/s12206-010-0713-9.

[29] Jasak, H. "Error Analysis and Estimation for the Finite Volume Method with Applications to Fluid Flows". PhD Thesis. London, United Kingdom: Imperial College, University of London, 1996.

[30] Wallin, S. "Engineering turbulence modelling for CFD with a focus on explicit algebraic Reynolds stress models". PhD Thesis. Stockholm, Sweden: Royal Institute of Technology (KTH), 2000.

[31] Wallin, S. and Johansson, A. V. An explicit algebraic Reynolds stress model for incompressible and compressible turbulent flows. *Journal of Fluid Mechanics* **403**, Jan. 2000, 89–132. DOI: 10.1017/S0022112099007004.

[32] Gyllenram, W. and Nilsson, H. Design and Validation of a Scale-Adaptive Filtering Technique for LRN Turbulence Modeling of Unsteady Flow. *Journal of Fluids Engineering* **130(5)**.051401, Apr. 2008. DOI: 10.1115/1.2911685.

[33] Nilsson, H. *CFD with OpenSource software - Course Notes*. Chalmers tekniska högskola. 2013.

[34] Hunt, J. C. R., Wray, A. A., and Moin, P. Eddies, streams, and convergence zones in turbulent flows. *2. Proceedings of the 1988 Summer Program*, Dec. 1988, 193–208.

[35] Avellan, F. Introduction to cavitation in hydraulic machinery. *Scientific Bulletin of the Politehnica University of Timisoara*. Scientific Bulletin of the Politehnica University of Timisoara,Transactions on Mechanics - Special issue, Oct. 2004.

[36] Dörfler, P., Sick, M., and Coutu, A. *Flow-Induced Pulsation and Vibration in Hydroelectric Machinery*. Springer, 2013. DOI: 10.1007/978-1-4471-4252-2.

[37] Tu, J., Yeoh, G.-H., and Liu, C. *Computational Fluid Dynamics: A Practical Approach*. Second Edition. Chicago, USA: Butterworth-Heinemann, 2013.

[38] Bredberg, J. *On the Wall Boundary Condition for Turbulence Models*. Tech. rep. Göteborg, Sweden: Department of Thermo and Fluid Dynamics, Chalmers University of Technology, 2000.

[39] Schobeiri, M. T. *Fluid Mechanics for Engineers - A Graduate Textbook*. Springer, 2010.

Appendices

A Additional results

As different operating conditions were used for pressure and velocity measurements at best efficiency point and high load, the comparison with experimental data wasn't done with the same simulations for pressure values and velocity profiles. The additional data which wasn't presented in Chapter 4 is thus given here for completeness. The simulated velocity profiles for the original operating points are presented in Section A.1 while the pressure and efficiency for the new operating points are shown in Section A.2.

A.1 Velocity profiles for mixing-plane simulations at the original operating points

In this section, the velocity profiles for the original operating conditions at best efficiency point and at high load are shown.

A.1.1 Best efficiency point

Figure A.1 shows the velocity profiles for best efficiency point with the original operating conditions (see Table 2.2). On Figure A.1a, the profiles for the first measurement line are shown, while the profiles for the second measurement line are on Figure A.1b.

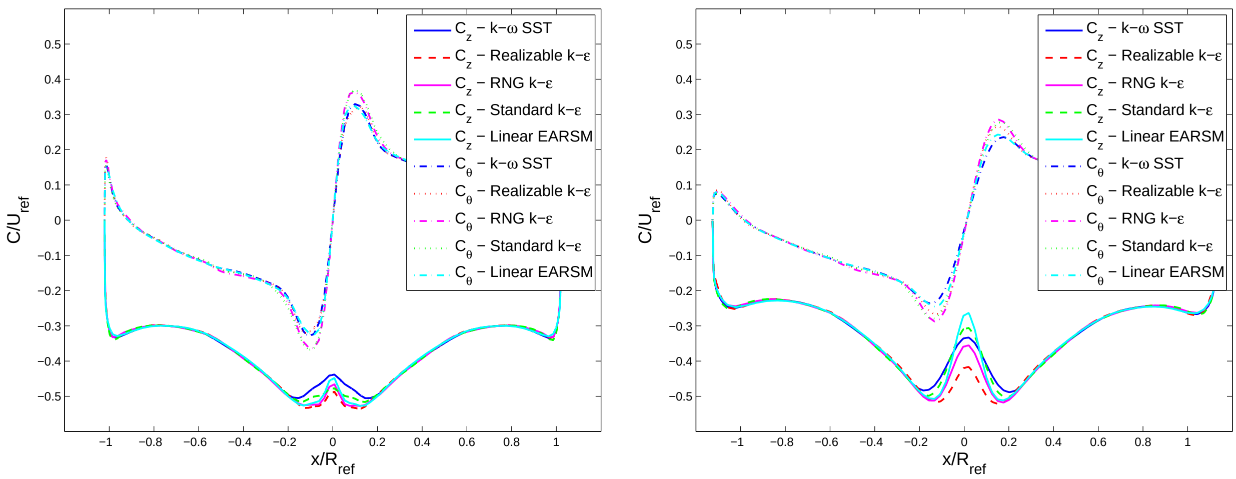

(a) *Velocity profile at the runner outlet (line 1) at best efficiency point (initial operating point) for different turbulence models.*

(b) *Velocity profile at the runner outlet (line 2) at best efficiency point (initial operating point) for different turbulence models.*

Figure A.1: *Velocity profiles at the runner outlet at best efficiency point (initial operating point). C_z denotes the axial velocity component and C_θ the tangential velocity component. Velocities are normalised by the circumferential reference velocity U_{ref}, and the x axis by the runner outlet radius R_{ref}.*

A.1.2 High load

Figure A.2 shows the velocity profiles for high load with the original operating conditions (see Table 2.2). On Figure A.2a, the profiles for the first measurement line are shown, while the profiles for the second measurement line are on Figure A.2a.

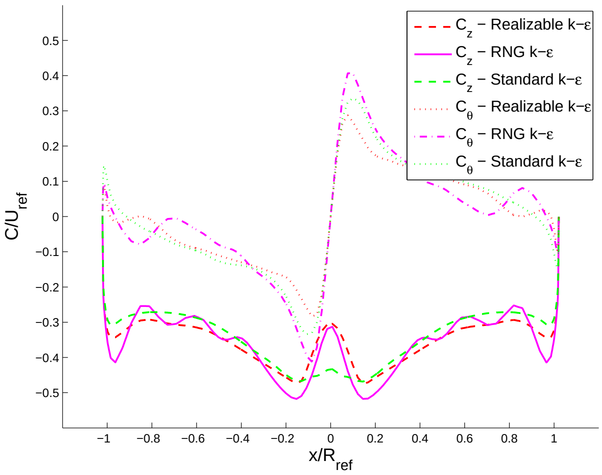

(a) *Velocity profile at the runner outlet (line 1) at high load (initial operating point) for different turbulence models.*

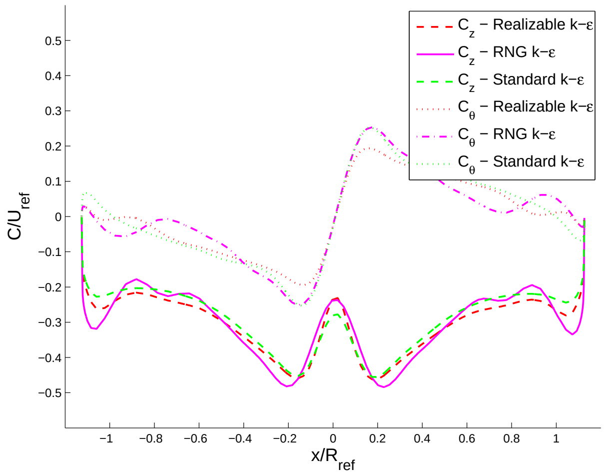

(b) *Velocity profile at the runner outlet (line 2) at high load (initial operating point) for different turbulence models.*

Figure A.2: *Velocity profiles at the runner outlet at best efficiency point (initial operating point). C_z denotes the axial velocity component and C_θ the tangential velocity component. Velocities are normalised by the circumferential reference velocity U_{ref}, and the x axis by the runner outlet radius R_{ref}.*

A.2 Pressure and efficiency data for mixing-plane simulations at the new operating points

In this section, the pressure values for the new operating conditions at best efficiency point and at high load are shown.

A.2.1 Best efficiency point

Figure A.3 shows the pressure values for best efficiency point with the new operating conditions (see Table 2.1). The corresponding values of efficiency and head are shown in Table A.1.

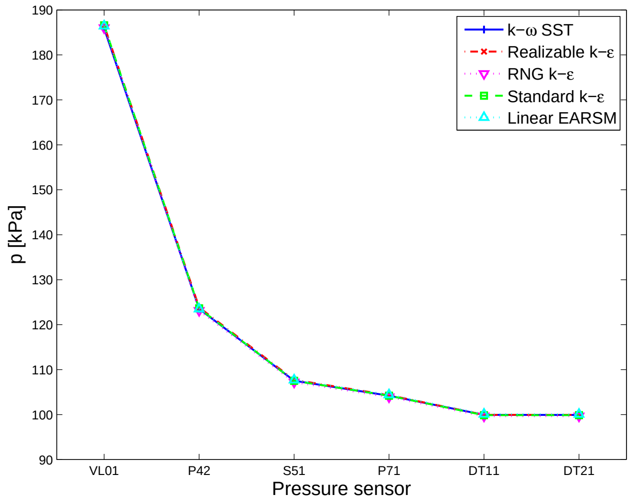

Figure A.3: *Comparison of the pressure values at several locations for different turbulence models at best efficiency point (new operating point).*

Turbulence model	$\eta_{IEC}[\%]$	$\eta_{F99}[\%]$	$H_{IEC}[m]$	$H_{F99}[m]$
Standard $k-\varepsilon$	92.09	96.19	15.08	14.44
RNG $k-\varepsilon$	92.03	96.13	15.07	14.43
Realizable $k-\varepsilon$	92.11	96.22	15.03	14.39
$k-\omega$ SST	92.39	96.55	14.93	14.29
Linear EARSM	92.12	96.24	14.99	14.35

Table A.1: Hydraulic efficiency and head with (H_{IEC}) and without (H_{F99}) the potential energy term at best efficiency point (new operating point).

A.2.2 High load

Figure A.4 shows the pressure values for best efficiency point with the new operating conditions (see Table 2.1). The corresponding values of efficiency and head are shown in Table A.2.

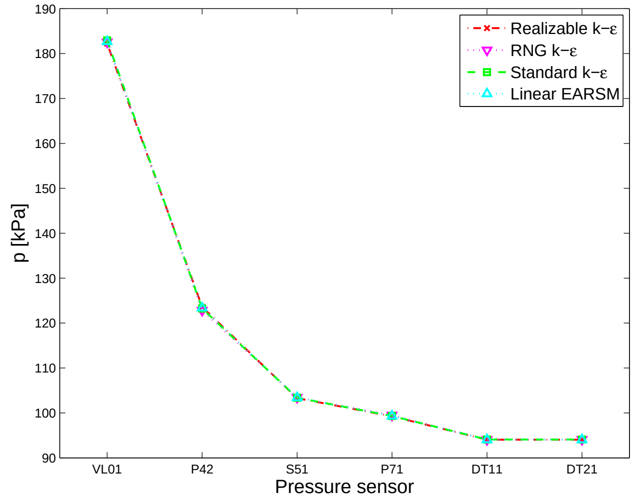

Figure A.4: *Comparison of the pressure values at several locations for different turbulence models at high load (new operating point).*

Turbulence model	$\eta_{IEC}[\%]$	$\eta_{F99}[\%]$	$H_{IEC}[m]$	$H_{F99}[m]$
Standard $k-\varepsilon$	92.15	96.98	12.90	12.26
RNG $k-\varepsilon$	91.58	96.40	12.84	12.20
Realizable $k-\varepsilon$	93.01	97.95	12.76	12.12
Linear EARSM	92.29	97.16	12.82	12.18

Table A.2: Hydraulic efficiency and head with (H_{IEC}) and without (H_{F99}) the potential energy term at high load (new operating point).

B Convergence

B.1 Steady-state mixing plane simulations

The evolution of the pressure and velocity residuals is monitored in order to assess the convergence of the simulations. Pressure residuals for the simulations are shown in the following sections for the 3 different operating points. For simplicity, only the residuals for the standard k-ε model are shown. In addition to the residuals, the evolution of axis power, head and local pressure gives an indication whether the solution is sufficiently stabilised. In order to do that, a relative residual compared to the final value is defined for these quantities, which allows to judge whether the solution is fully established or still fluctuating:

$$R_f = \frac{f(t) - f(t_{final})}{f(t_{final})}. \tag{B.1}$$

B.1.1 Best efficiency point

The residuals at best efficiency point (figures B.1a, B.1b and B.1c), drop quickly after around 1500 iterations, before stabilising and remaining largely constant with slight oscillations. After 6600 iterations, a peak is observed in all residuals because of changes in the solver settings. After this peak the residuals decrease again to their former values and remain stable. This behaviour is almost identical for the pressure, k and ε residuals. The velocity residuals are less sensitive, and the peak is somewhat covered by the ordinary fluctuations which are much stronger than for the other variables. Figure B.1d shows the evolution of the head and axial power for the best efficiency point simulations. Both the head and the axial power tend to a stable value after only 50 iterations. While the axial power then remains almost constant, the head keeps fluctuating while the pressure is converging. The fluctuations of the head remain until the end of the simulation, but with an amplitude far below 1% the solution can be considered being stabilised. The pressure at the probe locations (Figure B.2) fluctuates strongly around a mean value even when the solution is entirely converged.

B.1.2 Part load

The velocity residuals at part load (Figure B.3a) show that the solution is not yet converged after 10000 iterations. Several peaks are still appearing, until the solution finally converges. The k and ε residuals (Figure B.3b) show a similar behaviour, but without any peaks. The pressure residuals on the other hand (Figure B.3c) drop almost instantly and remain at a very low level. The evolution of the pressure at the probe locations (Figure B.4) confirms that the solution is not converged yet after 10000 iterations and the values are still changing. After around 13000 iterations however, the values remain stable and the solution is sufficiently converged. The head and axial power B.3d converge very quickly and remain almost fixed with only small oscillations.

B.1.3 High load

The high load simulations show good convergence behaviour once they are stabilised, and the velocity residuals (Figure B.5a) decrease to very low values which are even lower than the ones at best efficiency point. The pressure residuals (Figure B.5b) show a very similar behaviour, with a number of peaks before they eventually stabilise and remain constant. The residuals of k and ε (Figure B.5c) converge much quicker, with a quick drop around 6500 iterations and almost constant values for the remaining iterations. The head and axial power values at high load (Figure B.5d) tend very quickly to a fixed value and remain almost constant without peaks or fluctuations. In contrast, the pressure values at the probe locations (Figure B.6) fluctuate strongly as the solution is developing, before they eventually tend to a constant value and remain stable.

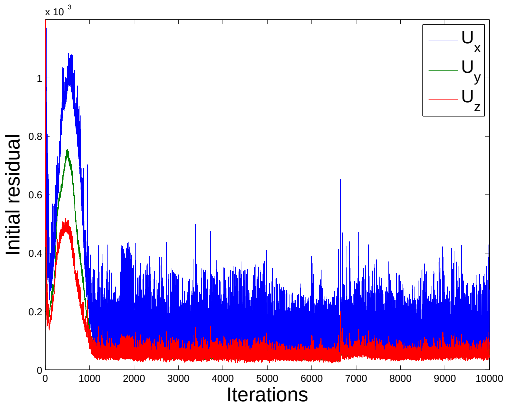

(a) *Evolution of the velocity residuals for standard k-ε model at best efficiency point.*

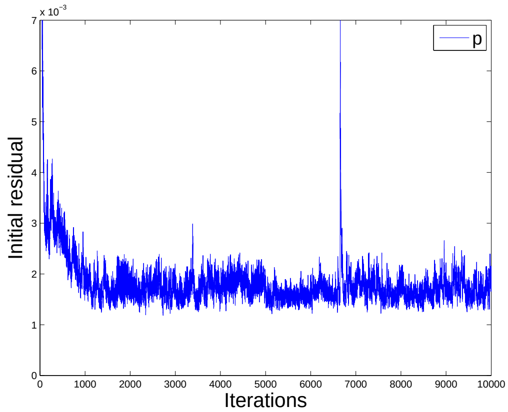

(b) *Evolution of the pressure residuals for standard k-ε model at best efficiency point.*

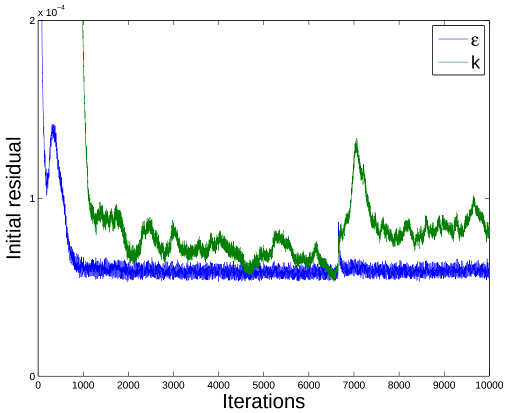

(c) *Evolution of the k and ε residuals for standard k-ε model at best efficiency point.*

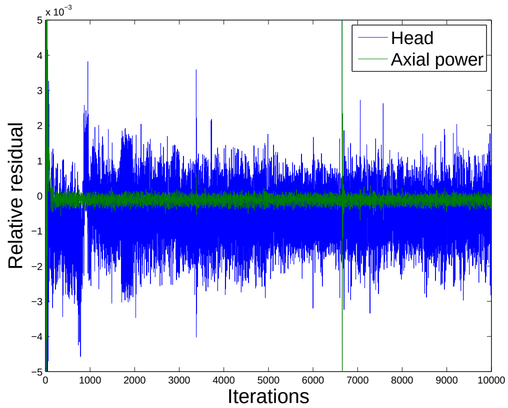

(d) *Evolution of the relative residuals of head and axial power for standard k-ε model at best efficiency point.*

Figure B.1: *Convergence behaviour of the mixing plane simulations at best efficiency point.*

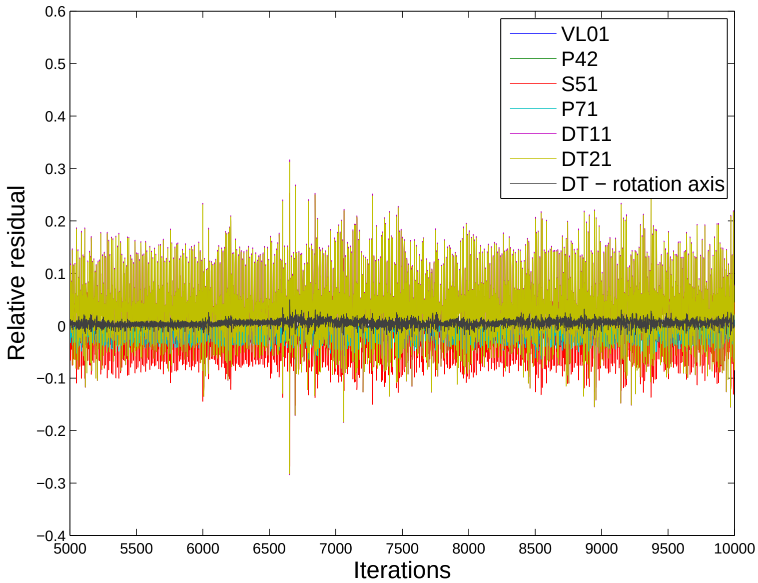

Figure B.2: *Evolution of the relative residuals of pressure at the probe locations for standard k-ε model at best efficiency point.*

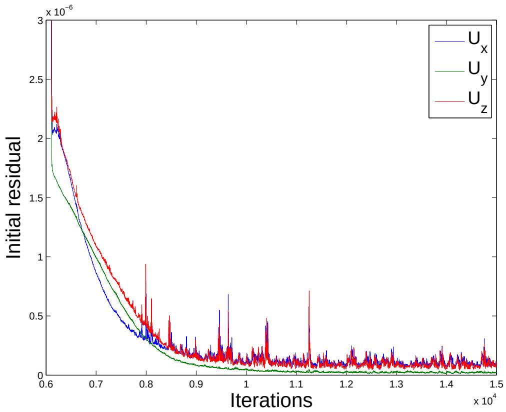

(a) *Evolution of the velocity residuals for standard k-ε model at part load.*

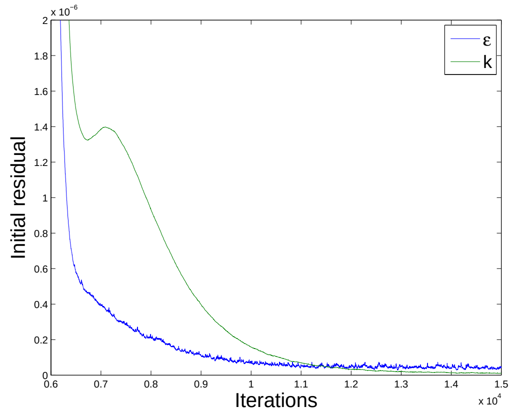

(b) *Evolution of the k and ε residuals for standard k-ε model at part load.*

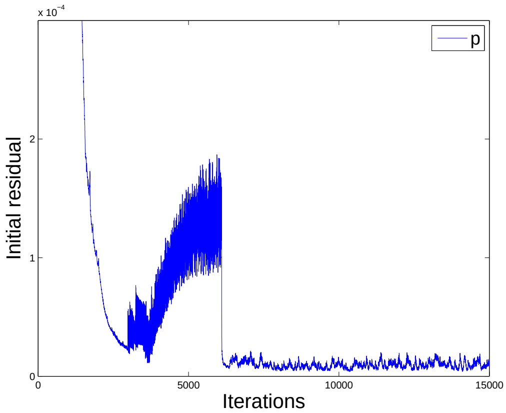

(c) *Evolution of the pressure residuals for standard k-ε model at part load.*

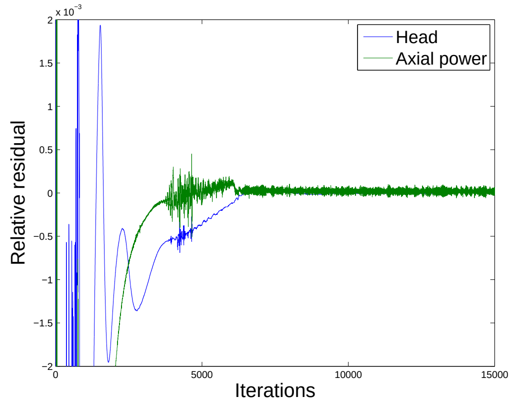

(d) *Evolution of the relative residuals of head and axial power for standard k-ε model at part load.*

Figure B.3: *Convergence behaviour of the mixing plane simulations at part load.*

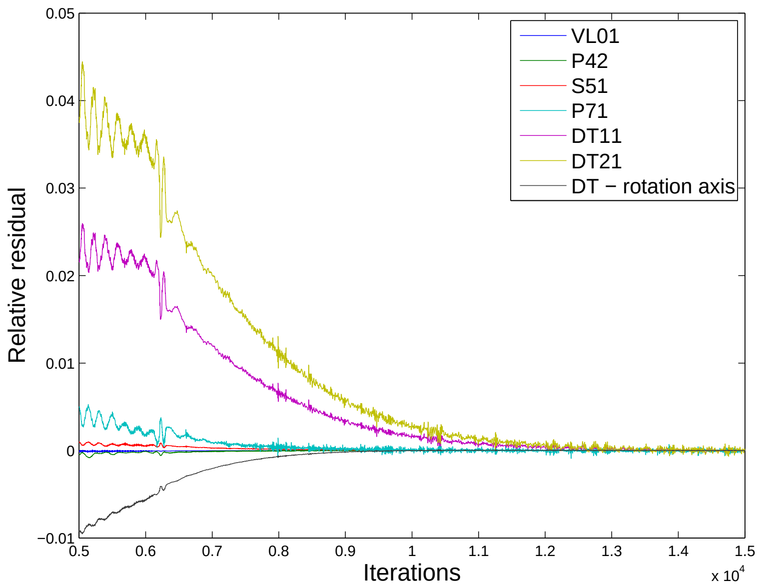

Figure B.4: *Evolution of the relative residuals of pressure at the probe locations for standard k-ε model at part load.*

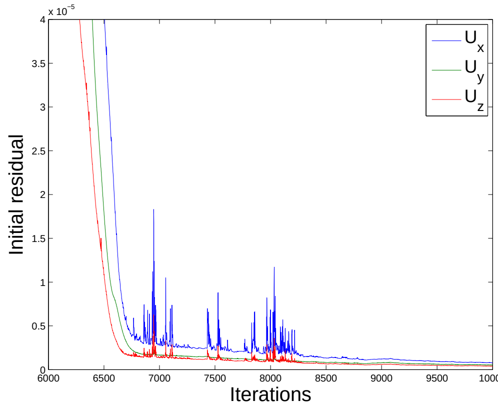

(a) *Evolution of the velocity residuals for standard k-ε model at high load.*

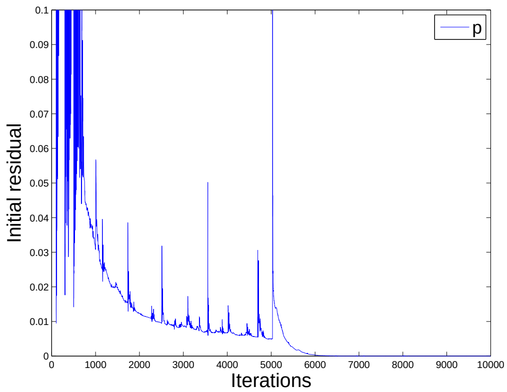

(b) *Evolution of the pressure residuals for standard k-ε model at high load.*

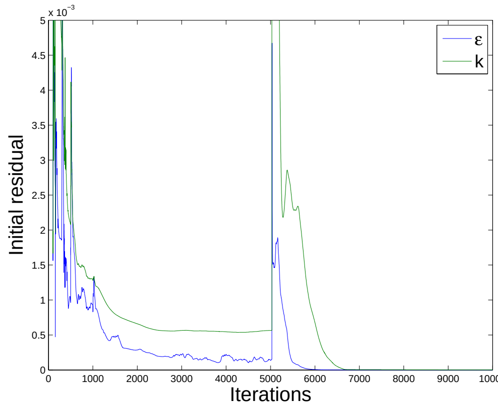

(c) *Evolution of the k and ε residuals for standard k-ε model at high load.*

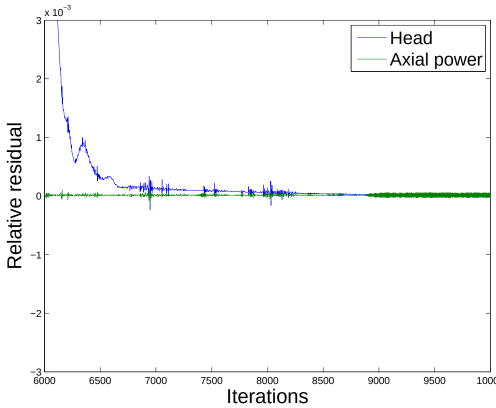

(d) *Evolution of the relative residuals of head and axial power for standard k-ε model at high load.*

Figure B.5: *Convergence behaviour of the mixing plane simulations at high load.*

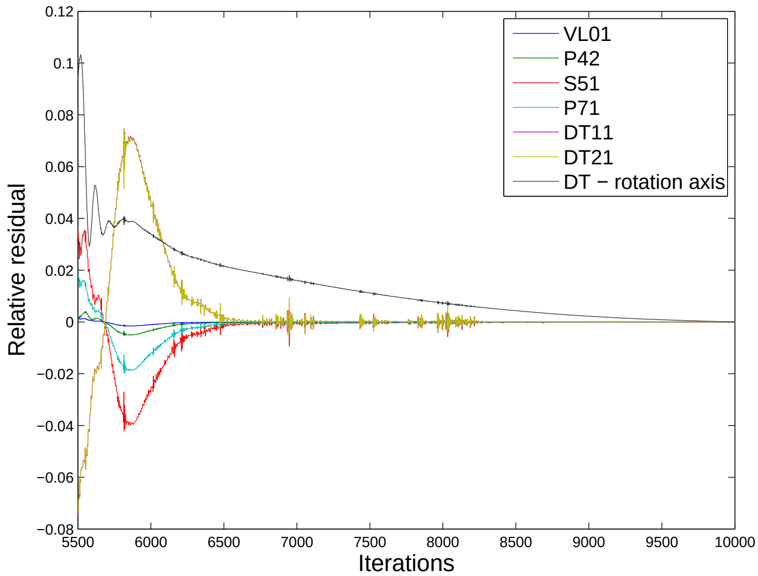

Figure B.6: *Evolution of the relative residuals of pressure at the probe locations for standard k-ε model at high load.*

B.2 Unsteady simulations

One of the main issues for the unsteady simulations is the bad pressure convergence. After the resolution of the momentum equation, the pressure equation is resolved three times before solving for k and ε, and this entire procedure is repeated four times. A large part of the computational effort is thus invested in solving the pressure field, and having a bad pressure convergence means that a lot of computational time is wasted on calculations that don't improve the quality of the simulations. The evolution of the pressure residuals for each operating point is shown in the following sections. In addition to the residuals, the Courant number is monitored to verify if the solution remains stable. Once the flow is fully developed, the maximum Courant number should remain stable except for slight periodic oscillations. A suddenly increasing maximum Courant number would give an indication that the velocity at some location in the flow is constantly increasing, which could be an early sign of divergence.

B.2.1 Best efficiency point

In Figure B.7a, the evolution of the initial pressure residuals for one time step are shown. Even though the residuals are decreasing each time the pressure equation is solved, the difference between consecutive iterations is relatively small. Every time the velocity is solved (after iterations 3, 6 and 9), the initial residuals increase strongly again. Several modifications in the settings have been tried out, but no substantial improvement has been achieved. Most certainly, the convergence behaviour is negatively affected by the errors in the mesh that are outlined in Section 3.5.2. Figure B.7b shows the evolution of the Courant number over an entire runner rotation. The maximum value remains stable without any abrupt increase, and only periodic oscillations are present, indicating that the solution is stable.

B.2.2 Part load

The pressure residuals at part-load (Figure B.7c) show also a strong increase after every time the velocity equation is solved. After the 6^{th} and 9^{th} iteration, the residuals increase even above the residuals at the previous step, and the final residuals remain almost an order of magnitude higher than at best efficiency point. Figure B.7d shows the maximum Courant number, which shows oscillations around a stable value but no sharp increase or divergence.

B.2.3 High load

The behaviour at high load is similar to what is observed at the other operating points. Figure B.7e shows the initial and final residuals for one time step. As for the best efficiency point simulations, the residuals re-increase every time the velocity is solved. After all iterations however, the residuals go finally to relatively low values, and the convergence behaviour is globally similar to the best efficiency point and better than at part load. The maximum Courant number (Figure B.7f) oscillates around a stable value, but remains bounded.

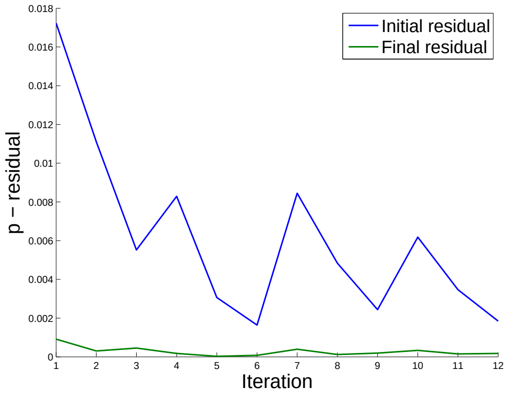

(a) *Evolution of the initial and final pressure residuals for one time step at best efficiency point.*

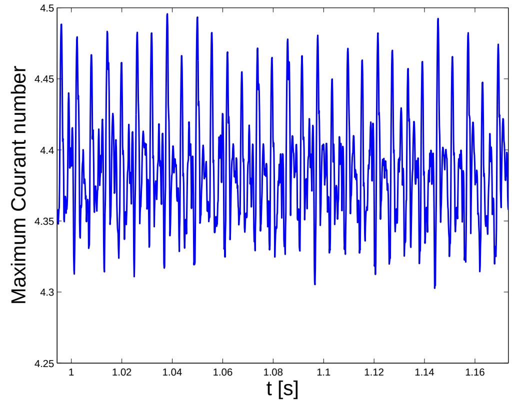

(b) *Time history of the maximum Courant number at best efficiency point.*

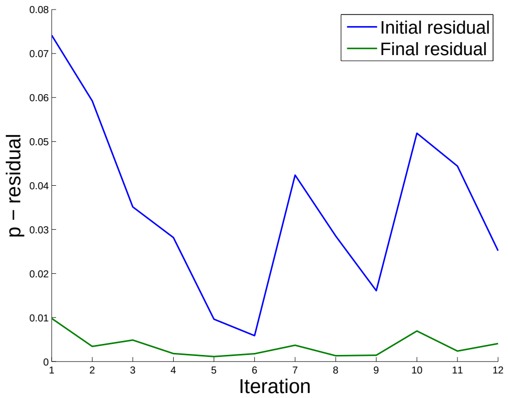

(c) *Evolution of the initial and final pressure residuals for one time step at part load.*

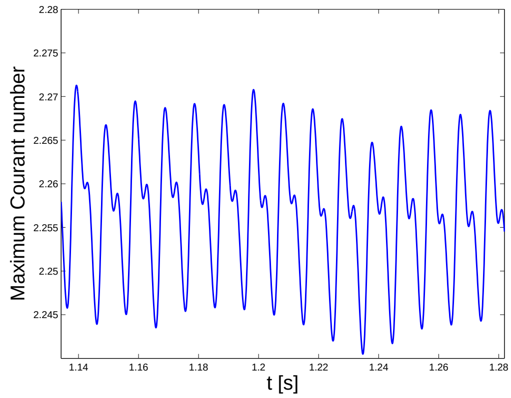

(d) *Time history of the maximum Courant number at part load.*

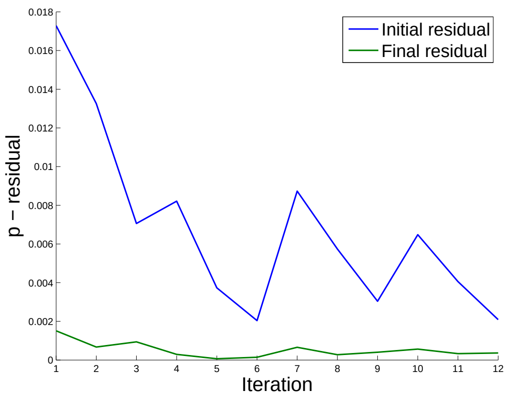

(e) *Evolution of the initial and final pressure residuals for one time step at high load.*

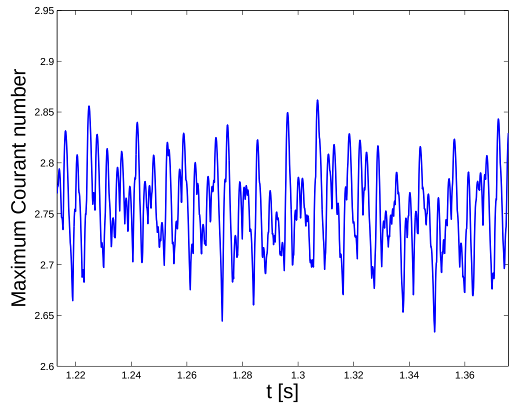

(f) *Time history of the maximum Courant number at high load.*

Figure B.7: *Convergence behaviour of the unsteady simulations at best efficiency point, part load and high load.*

C Mesh generation, refinement and y^+ - values

C.1 Original mesh supplied by the workshop committee

The geometry of the entire turbine model as well as a mesh were provided by the organising committee of the workshop. The original mesh is block-structured mesh for the full 3D geometry, with the characteristics presented in Table C.1. It consists of 3 separate components (spiral casing, runner and draft tube), while the runner is once again split in two parts. The runner consists of a main part defining most of the geometry, with an additional cylindrical volume below the hub which is meshed separately.

Part	Number of cells		
	BEP	High load	Part load
Spiral Casing	3772349	3924534	3775745
Runner - main part	5447085		
Runner - second part	606816		
Draft tube	3706144		
Total	13532394	13684579	13535790

Table C.1: Number of cells in the original mesh.

In the original mesh, problems arise on cylindrical surfaces due to the resolution of curves in the mesh generation software. While the surfaces are properly represented with a high resolution, the corresponding curves are piecewise linear, which creates disturbances near the border of the surfaces (see Figure C.1). As the guide-vane outlet and the runner inlet are concerned by this issues, this affects the mixing plane interpolation and leads to divergence. The problem is fixed by splitting the concerned surfaces into smaller pieces with sufficient resolution.

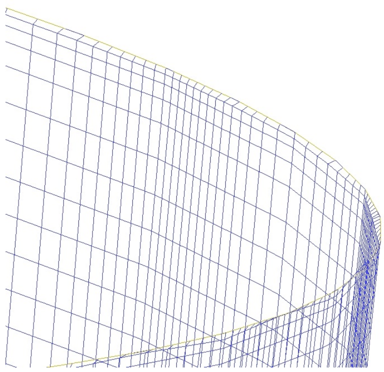

Figure C.1: *Piecewise linear curves due to insufficient resolution on the cylindrical surface at the runner inlet.*

C.2 Wall y^+ - values and mesh refinement for steady-state mixing plane simulations

An analysis of the $y+$ distribution shows that the problematic areas with too high values are mainly close to the curved surface of the guide vane, and at the runner outlet below the hub. Having too low values means that the first grid point is situated in the viscous sub-layer where the logarithmic approximation is not verified, leading to a falsification of the results. Too high values signify that the region covered by the wall function is too large and the boundary layer is not accurately resolved due to a low grid resolution [39, 38]. In the following section, the values and distribution for each operating point are presented. Furthermore, the results for the original mesh for best efficiency point are shown and compared to the refined mesh. For simplicity, only the results for the standard k-ε are shown as the comparison between old and new mesh was done with this model.

Initial meshes

Best efficiency point Figure C.2 shows the y^+ distribution at best efficiency point with the mesh before refinement. The maximum and minimum value for each patch are summed up in Table C.2. On Figure C.2a, the high values are clearly visible on the hub near the outlet of the runner, as well as around the leading edge of the blades. Figures C.2a and C.2b also show the very low values on both the pressure and the suction side of the blades. The values on the guide vanes are shown in Figure C.2c, where very high values are present over a large area of the low pressure side and on the central part of the high pressure side.

Patch	Lowest y^+ value	Highest y^+ value
Blade pressure side	2.554	50.922
Blade suction side	5.096	202.289
Splitter blade	2.729	131.370
Guide vanes	4.870	175.968
Hub	3.308	79.541
Shroud	2.914	95.021

Table C.2: Values of wall y^+ at best efficiency point with the initial mesh before refinement.

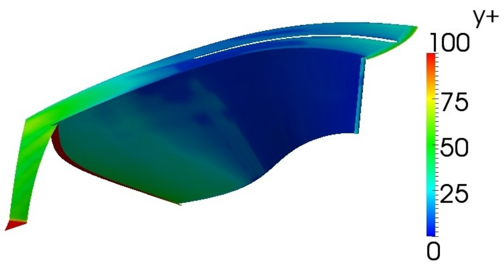

(a) *Distribution of y^+ values on the blade pressure side and the hub at best efficiency point with the initial mesh before refinement.*

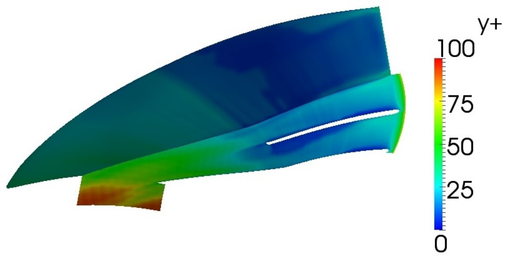

(b) *Distribution of y^+ values on the blade suction side and the shroud at best efficiency point with the initial mesh before refinement.*

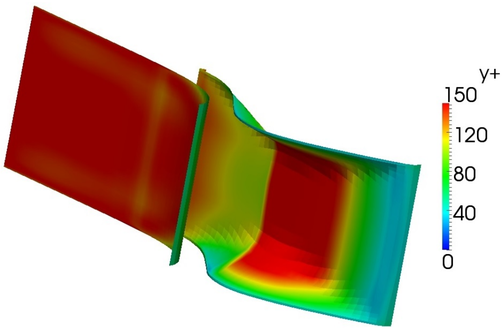

(c) *Distribution of y^+ values on the guide vanes side and the hub at best efficiency point with the initial mesh before refinement.*

Figure C.2: *Distribution of wall y^+ - values in the runner and guide vane passage at best efficiency point with the initial mesh before refinement.*

Part load The distribution on the blades and in the guide vane passage for part load is presented in Figure C.3. The extreme values for each patch are shown in Table C.3. The distribution is similar to what is observed at best efficiency point, but the flow velocities are obviously lower which leads to lower maximum values in the guide vane passage (Figure C.3c). On the other hand, this leads also to even lower values at locations where they were already too low at best efficiency point. Surprisingly, the high values near the trailing edge of the blade and around the hub are even more pronounced than at best efficiency point.

Patch	Lowest y^+ value	Highest y^+ value
Blade pressure side	1.228	39.875
Blade suction side	4.145	372.391
Splitter blade	2.762	106.698
Guide vanes	9.647	121.321
Hub	1.739	177.003
Shroud	1.638	80.212

Table C.3: Values of wall y^+ at part load operation.

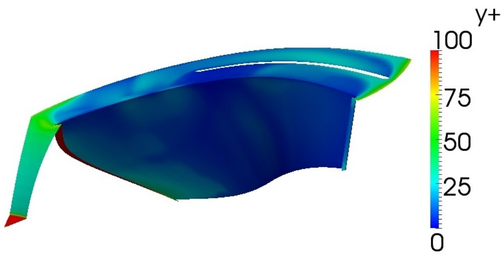

(a) *Distribution of y^+ values on the blade pressure side and the hub at part load.*

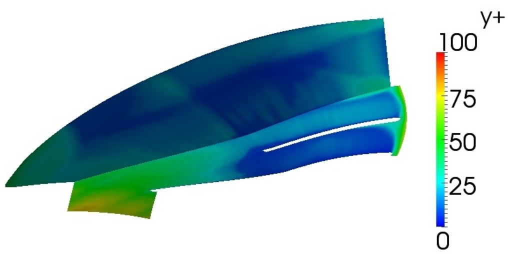

(b) *Distribution of y^+ values on the blade suction side and the shroud at part load.*

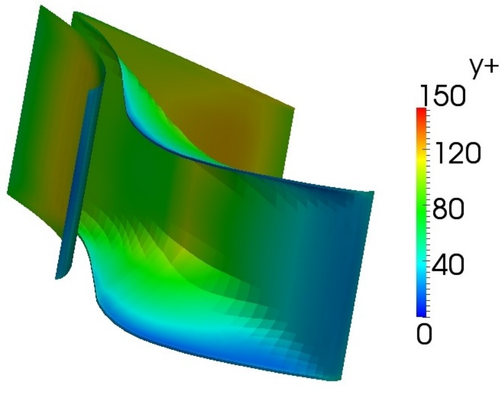

(c) *Distribution of y^+ values on the guide vanes side and the hub at part load.*

Figure C.3: *Distribution of wall y^+ - values in the runner and guide vane passage at part load.*

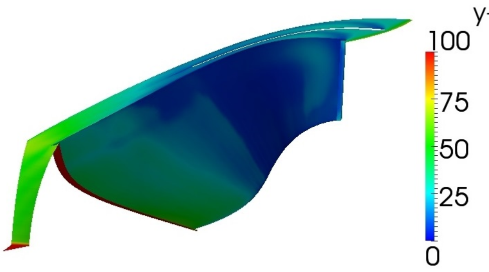

(a) *Distribution of y^+ values on the blade pressure side and the hub at high load.*

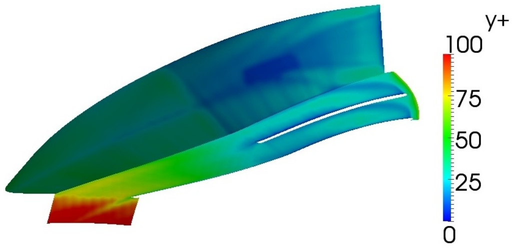

(b) *Distribution of y^+ values on the blade suction side and the shroud at high load.*

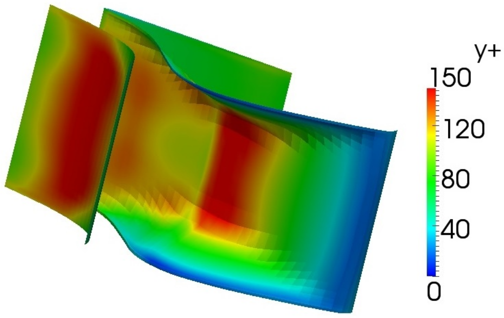

(c) *Distribution of y^+ values on the guide vanes side and the hub at high load.*

Figure C.4: *Distribution of wall y^+ - values in the runner and guide vane passage at high load.*

High load At high load operation, very high values are present below the hub as well as on the blade pressure side (Table C.4). A closer look at the distribution (Figure C.4) shows that the problematic zones are the same as for the other operating points, with exceptionally high values at the blade trailing edge and below the hub (Figure C.4a). The high values on the shroud are also located close to the trailing edge of the blade and near the runner outlet (Figure C.4b). On the guide vane surface, the values are also very high (C.4c), similarly to what is observed at best efficiency point.

Patch	Lowest y^+ value	Highest y^+ value
Blade pressure side	1.863	60.955
Blade suction side	5.510	236.721
Splitter blade	3.165	218.402
Guide vanes	7.112	187.926
Hub	3.039	287.771
Shroud	2.157	115.117

Table C.4: Values of wall y^+ at high load operation.

Refined mesh for best efficiency point

While the meshes at high load and part load remain unchanged, a refined mesh for the runner and guide vane passage is created for best efficiency point. All the simulations at best efficiency point presented previously were conducted with this refined mesh. As the most problematic regions are located below the hub of the runner and on the surface of the guide vane pressure side, the mesh grading in these regions is changed in order to reduce the y^+ values and increase the resolution. As the log-law approximation is only valid on a flat plate, the resolution of the mesh around the sharp corner of the hub is expected to be more important than the y^+ values. The initial mesh below the hub is shown in Figure C.5a, while the refined one is presented in Figure C.5b. One can see that the first row of cells is brought closer to the surface of the hub, and the number of cells in the axial direction is increased from 9 to 13. However, a drawback of this modification is that this refined region goes over the whole width of the runner and creates a jump in stream-wise grid size between the

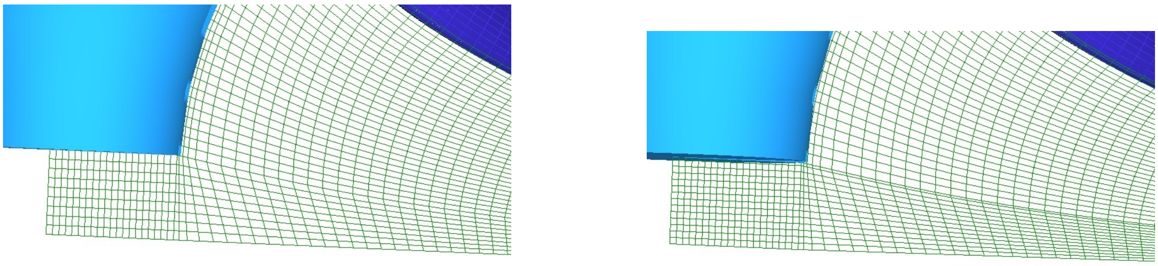

(a) *Original mesh between the hub and the runner outlet.*

(b) *Refined mesh between the hub and the runner outlet.*

Figure C.5: *Mesh refinement in the runner below the hub for best efficiency point.*

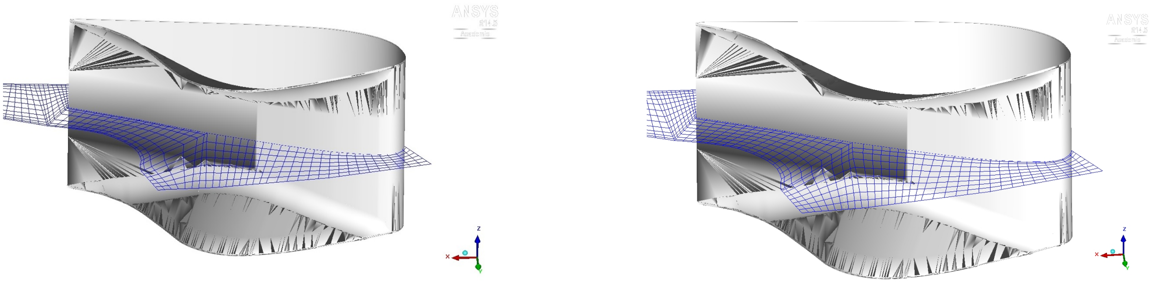

(a) *Original mesh in the guide vane passage.*

(b) *Refined mesh in the guide vane passage.*

Figure C.6: *Mesh refinement in the guide vane passage for best efficiency point.*

blades and the runner outlet. In a further step, this should be avoided by modifying the blocking and grading accordingly in both regions.

The second region which is modified is the pressure side of the guide vanes. Due to the particular shape of the guide vanes, the grid becomes coarser in the centre of the guide vane passage (see Figure C.6a). In order to refine the mesh in that region, the number of cells in the cross-flow direction is increased from 7 to 9 and the grading is adapted so as to obtain a thinner first cell at the wall. The refined mesh is shown in Figure C.6b. While the near wall resolution is effectively improved, the refinement leads also to more skewed cells at the limit between the different blocks.

The size of the mesh increases from 3927245 to 3947947 cells for the new mesh. The main increase in the number of cells is in the runner (from 335218 to 351860 cells), with only a slight increase (from 21083 to 25143 cells) in the guide vane passage. While the refinement has positive effects on the wall y^+ values, it does affect the overall mesh quality negatively. The number of non-orthogonal faces is now 18775 compared to 8387 in the original mesh. The average non-orthogonality increases from 15.37 to 15.59, while the maximum goes from 76.73 to 80.38. The quality of the runner mesh remains largely unaffected by the modifications. All the additional non-orthogonal cells are located in the region near the leading edge of the second guide vane (Figure 3.3b), which is affected by the changes in the grading. Due to these negative impact on the mesh quality, no such modifications are made on the meshes for part load and high load, as introducing additional cells of bad quality would only let the convergence behaviour deteriorate further. To allow an evaluation of the mesh influence, a comparison is made between the original and the refined mesh for best efficiency point. Table C.5 shows the wall y^+ values for the refined mesh. The maximum values are considerably lower than with the original mesh (see Table C.2). This has also an influence on the efficiency prediction, which is 0.4% lower with the refined mesh and thus closer to the experimental value (see Table C.6). However, the pressure distribution is practically identical between the two meshes (see Figure C.7). The most important impact of the refinement can be observed on the velocity profiles, where the mesh below the hub has obviously a strong influence on the flow (Figure C.8a). This difference is however only local, and has almost disappeared at the second measurement line (Figure C.8b).

Patch	Lowest y^+ value	Highest y^+ value
Blade pressure side	0.448	22.653
Blade suction side	0.954	3.015
Splitter blade	2.624	189.853
Guide vanes	2.054	34.733
Hub	1.387	22.869
Shroud	0.560	5.857

Table C.5: Values of wall y^+ at best efficiency point with the refined mesh.

Mesh	Hydraulic efficiency (IEC) $\eta_{h,IEC}$ [%]	Hydraulic efficiency (F99) $\eta_{h,F99}$ [%]
Original mesh	94.40	99.02
Refined mesh	94.04	98.63

Table C.6: Efficiency values at best efficiency point for original and refined mesh.

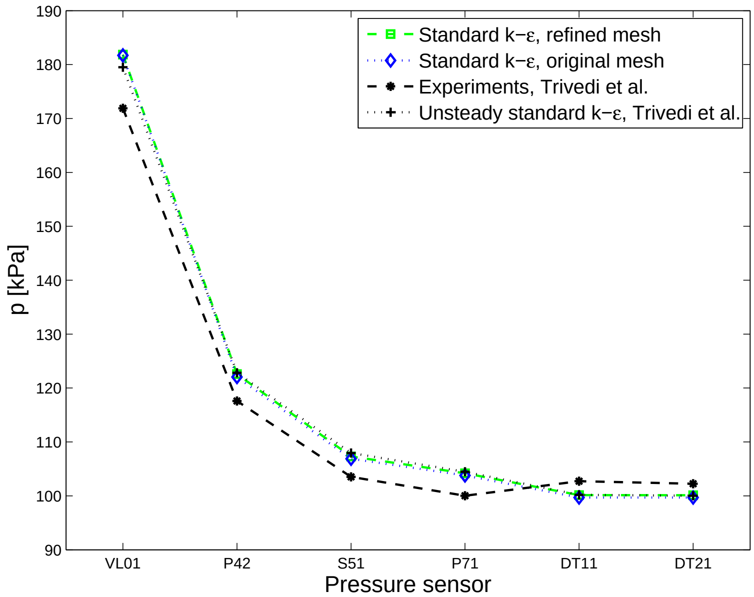

Figure C.7: *Comparison of the pressure evolution in the turbine for the original and the refined mesh.*

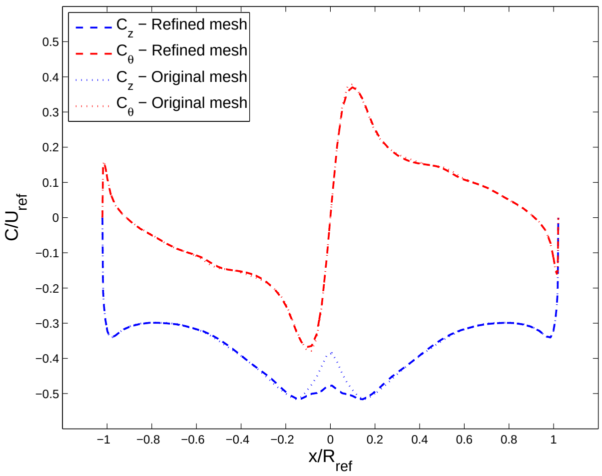

(a) *Comparison of the velocity profiles at the runner outlet (line 1) for original and refined mesh.*

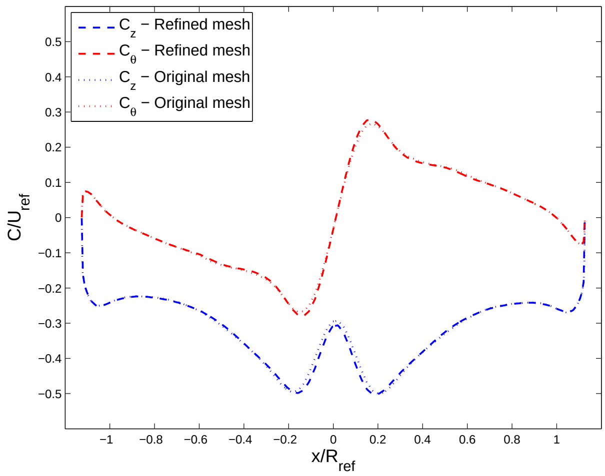

(b) *Comparison of the velocity profiles at the runner outlet (line 2) for original and refined mesh.*

Figure C.8: *Velocity profiles at the runner outlet at best efficiency point for original and refined mesh. C_z denotes the axial velocity component and C_θ the tangential velocity component. Velocities are normalised by the circumferential reference velocity U_{ref}, and the x axis by the runner outlet radius R_{ref}.*

C.3 Wall y^+ - values for unsteady simulations

In this section, the maximum and minimum wall y^+ values for the unsteady simulations are shown.

Best efficiency point

Table C.7 shows the maximum and minimum wall y^+ values on all patches at best efficiency point.

Patch	Lowest y^+ value	Highest y^+ value
Blade pressure side	2.117	81.19
Blade suction side	3.804	154.197
Splitter blade	2.903	148.175
Guide vanes	22.933	480.508
Stay vanes	2.822	534.661
Hub	2.593	80.750
Shroud	2.546	99.035

Table C.7: Values of wall y^+ at best efficiency point for unsteady simulations.

Part load

Table C.8 shows the maximum and minimum wall y^+ values on all patches at part load.

Patch	Lowest y^+ value	Highest y^+ value
Blade pressure side	0.627	58.928
Blade suction side	1.715	379.907
Splitter blade	2.903	148.175
Guide vanes	22.933	480.508
Stay vanes	2.822	534.661
Hub	2.593	80.750
Shroud	2.546	99.035

Table C.8: Values of wall y^+ at part load for unsteady simulations.

High load

Table C.9 shows the maximum and minimum wall y^+ values on all patches at high load.

Patch	Lowest y^+ value	Highest y^+ value
Blade pressure side	1.201	89.663
Blade suction side	4.585	183.321
Splitter blade	1.937	261.322
Guide vanes	12.644	242.433
Stay vanes	3.405	582.842
Hub	2.580	70.132
Shroud	1.283	118.194

Table C.9: Values of wall y^+ at high load for unsteady simulations.

D Analysis of the mixing plane and GGI interfaces

D.1 Behaviour of the mixing plane and cyclic GGI interfaces

By calculating a circumferential average of all quantities, the mixing plane cancels out a large amount of information regarding the wakes of the guide vane passage and the runner blades. This averaging process leads to a clearly visible border between the different regions both at the inlet and outlet of the runner. Figure D.1 shows the interface between the guide vane passage and the runner inlet, with white imprints of the guide vanes in the top half and the runner blades in the bottom half. An interesting feature is the high pressure region around the stagnation point at the runner leading edge, which doesn't propagate upstream and leads to an abrupt change in the pressure field at the interface. Figure D.2 shows an overlay of the runner outlet and draft tube inlet, illustrating that at the runner outlet the effect of the averaging at the mixing plane interface is also clearly visible.

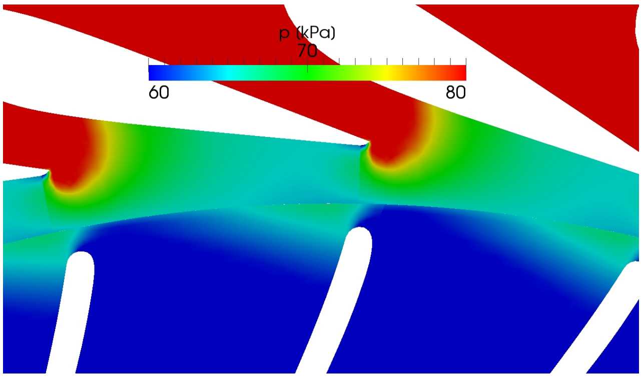

Figure D.1: *Influence of the mixing plane interface at the runner inlet at best efficiency point using standard k-ε model.*

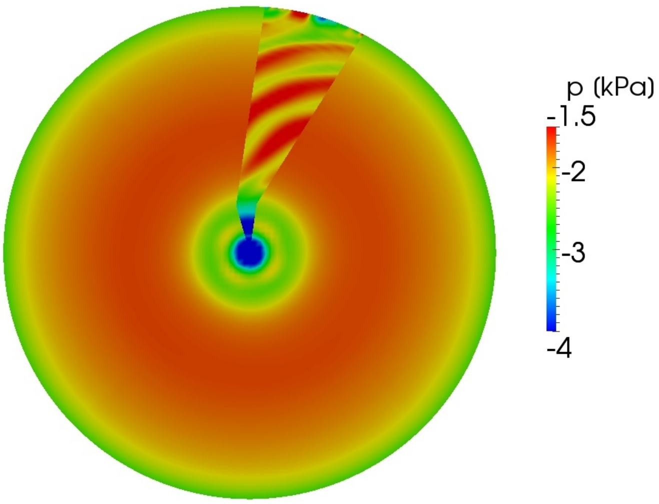

Figure D.2: *Influence of the mixing plane interface at the runner outlet at best efficiency point using standard k-ε model. The entire circle shows the draft tube inlet, while the slice shows the runner outlet.*

The cyclic GGI can also be identified in the results on the low pressure side of the guide vanes, close to the trailing edge (see Figure D.1). Looking at the mesh near the cyclic boundary, differences in the mesh size in the direction perpendicular to the interface between the two sides become apparent (see Figure D.3). This should be avoided in the future as it influences the values near the cyclic GGI interface, leading to disturbances on the periodic boundary.

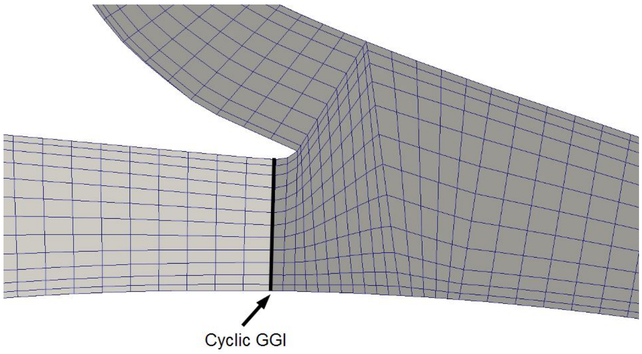

Figure D.3: *Difference in mesh size at the cyclic GGI interface at the trailing edge of the guide vanes.*

D.2 Influence of the mixing plane schemes

Identical simulations are conducted with two sets of mixing plane schemes at best efficiency point using the standard k-ε model to investigate the influence of the schemes. Table D.1 shows the difference for the global quantities, while the pressure distribution is shown in Figure D.4. In figures D.5 and D.6, velocity profiles at the outlet are compared between the two cases. At the first line (Figure D.5), a clear difference is visible between the two cases. The old mixing plane schemes (area averaging) show a more pronounced, but also more confined recirculation region below the hub. The region with strong swirl is considerably narrower. These effects are still visible at the second line (Figure D.6), but are already greatly reduced leading to a better agreement between the two simulations. Even though the influence of the schemes is locally confined to the mixing plane interface, these results show that it can have a certain impact on the whole simulation, including the global quantities such as efficiency and head. The pressure probes however give almost identical results for the two types of schemes, and the differences for the velocity profiles are in the same order of magnitude as the influence of the turbulence model.

Schemes	Hydraulic efficiency (IEC) $\eta_{h,IEC}$ [%]	Hydraulic efficiency (F99) $\eta_{h,F99}$ [%]	Head (IEC) $H_{h,IEC}$ $[m]$	Head (F99) $H_{h,IEC}$ $[m]$
Area averaging	94.15	98.76	13.771	13.128
New schemes	94.04	98.63	13.790	13.148

Table D.1: Efficiency values at best efficiency point for the different mixing plane schemes.

D.3 Behaviour of the general grid interface

For the unsteady simulations, a general grid interface is used on both the inlet and outlet of the runner to connect the rotating and the stationary meshes. Figure D.7 shows the guide vane passage and the runner inlet. Even though there are some disturbances due to the interpolation and different grid sizes on the two sides of the interface, the limit between the two regions is hardly visible. On the outlet interface (Figure D.8), some differences between the two patches become apparent, with disturbances on the upstream patch that are not present on the downstream patch. Apart from these details, the interface is however performing well and transmitting the flow field correctly to the downstream patch.

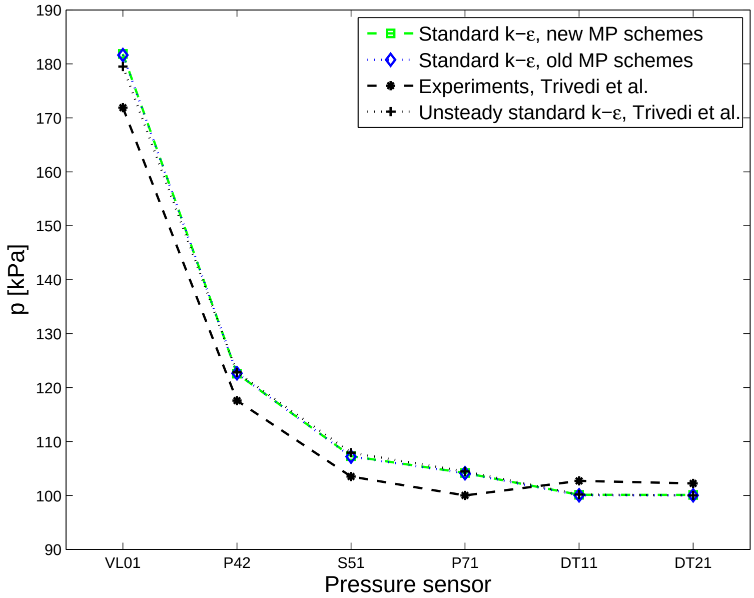

Figure D.4: *Comparison of the pressure evolution in the turbine for old and new mixing plane schemes.*

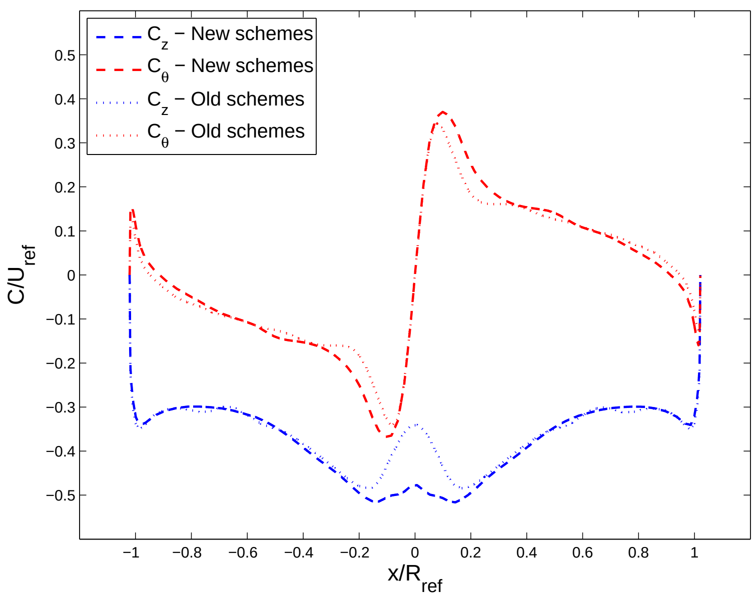

Figure D.5: *Comparison of the velocity profiles at line 1 at best efficiency for old and new mixing plane schemes using standard k-ε model.*

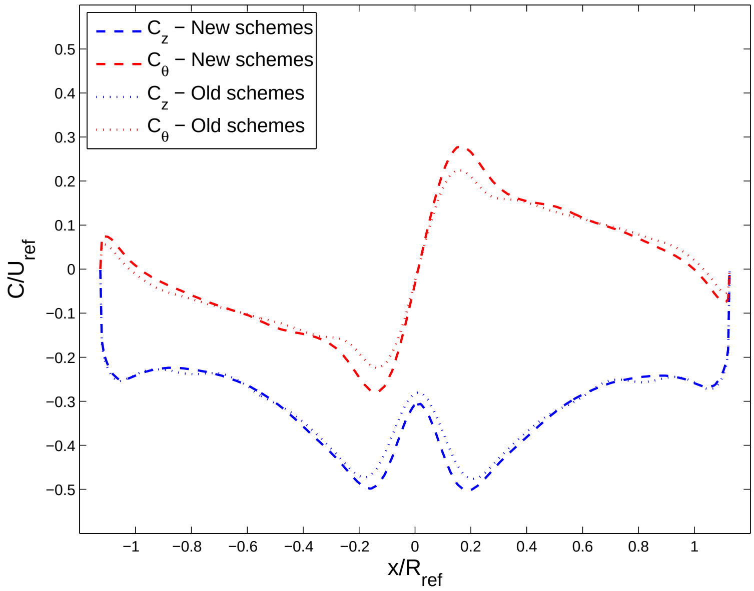

Figure D.6: *Comparison of the velocity profiles at line 2 at best efficiency for old and new mixing plane schemes using standard k-ε model.*

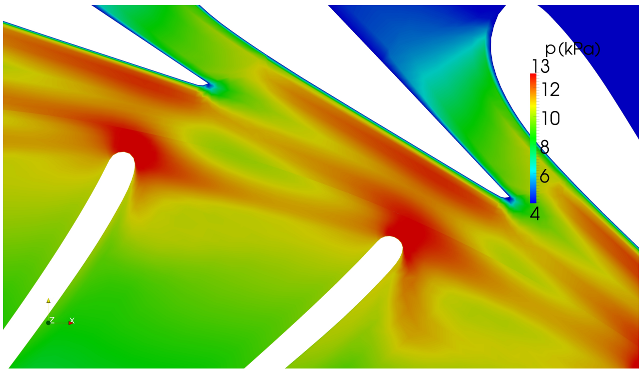

Figure D.7: *Pressure distribution around the general grid interface at the runner inlet.*

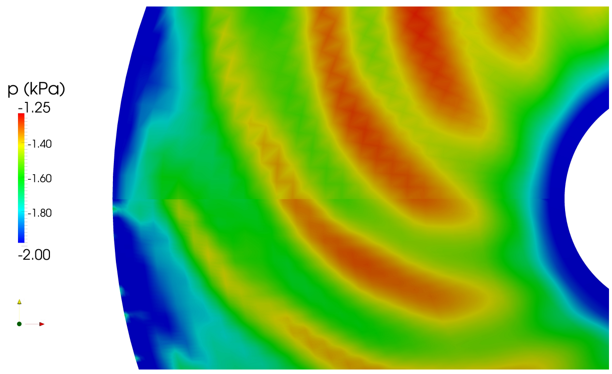

Figure D.8: *Pressure distribution around the general grid interface at the runner inlet. The top half is the downstream patch, the bottom half is the upstream patch.*

E Turbulence modelling

For the turbulence models described in section 3.6, the default coefficients implemented in OpenFOAM were used. The coefficients for each of the used models are listed in Table E.1.

Coefficient	Value
C_μ	0.09
C_1	1.44
C_2	1.92
α_ε	0.76923

(a) Coefficients used for the standard $k-\varepsilon$ model.

Coefficient	Value
C_μ	0.0845
C_1	1.42
C_2	1.68
α_k	1.39
α_ε	1.39
η_0	4.38
β	0.012

(b) Coefficients used for the RNG $k-\varepsilon$ model.

Coefficient	Value
C_μ	0.09
A_0	4.0
C_2	1.9
α_k	1
α_ε	0.833333

(c) Coefficients used for the Realizable $k-\varepsilon$ model.

Coefficient	Value
β^*	0.09
β	0.075
α	0.5556
σ_K	2.0
σ_ω	2.0
C_1'	1.8
C_τ	6.0

(d) Coefficients used for the linear EARSM model.

Coefficient	Value
α_{k1}	0.85034
α_{k2}	1.0
$\alpha_{\omega1}$	0.5
$\alpha_{\omega2}$	0.85616
γ_1	0.5532
γ_2	0.4403
β_1	0.075
β_2	0.0828
β^*	0.09
A_1	0.31
C_1	10
C_μ	0.09

(e) Coefficients used for the $k-\omega$ SST and $k-\omega$ SSTF model.

Table E.1: Coefficients for the turbulence models.

F Frequency spectrum of experimental pressure measurements

The frequency spectrum of the measured pressure values (Figure F.1) is calculated with the same method as for the numerical results (section 4.2), based on the experimental pressure results provided by the workshop committee [8].

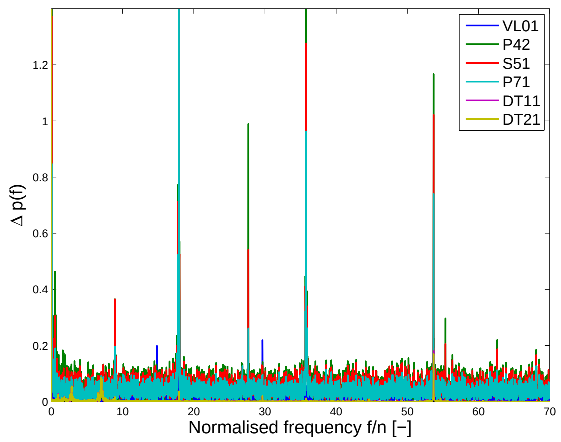

(a) *Frequency spectrum of the measured pressure fluctuations at best efficiency point, normalised by the runner rotation frequency.*

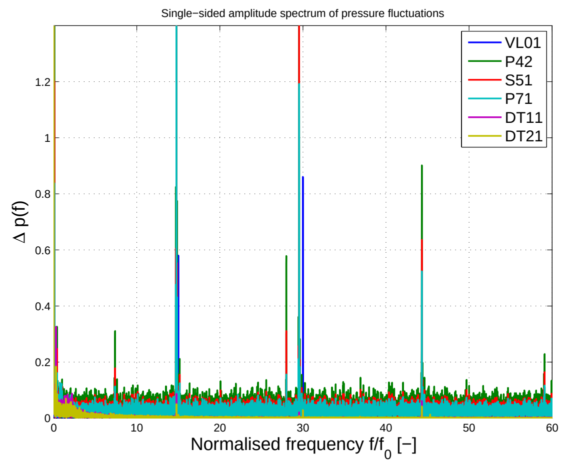

(b) *Frequency spectrum of the measured pressure fluctuations at part load, normalised by the runner rotation frequency.*

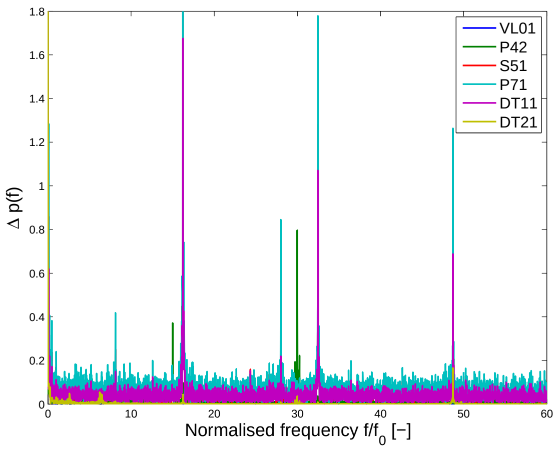

(c) *Frequency spectrum of the measured pressure fluctuations at high load, normalised by the runner rotation frequency.*

Figure F.1: *Frequency spectrum of experimental pressure measurements at all three operating points, based on the data provided by the workshop committee [8].*

G Additions to OpenFOAM

Several features that are needed for the above-mentioned simulations are not currently included in the distribution of foam-extend that was used. Certain personal modifications and minor developments had therefore to be done.

G.1 Moving probes in a rotating domain

For the unsteady simulations using a dynamic mesh, probes must be set on the blades at the locations where the pressure sensors were installed for the experimental measurements. By default, pressure probes remain at fixed coordinates even when the region around them is moving. In order to let the probes move together with the mesh and stay on the blades, the corresponding class had to be adapted accordingly. The modified version allows the user to change for each set of probes whether they should move with the mesh or remain at the chosen coordinate.

G.2 Variable rotational speed for moving mesh simulations

The existing class "turboFvMesh" that is used to rotate the runner mesh for unsteady simulations allows the use of several regions with different angular velocities, but only rotation at constant speed is possible. In order to simulate runner oscillations, a variation of this class that allows variable rotational speed had to be written. The current version ("variableTurboFvMEsh") allows the use of constant rotation, ramped angular speed and sinusoidal oscillations around a constant rotational speed. This feature is also convenient to ramp up the rotational speed of the runner at the beginning of simulations if stability is an issue.

G.3 Turbulence models

The linear explicit algebraic Reynolds stress model (linear EARSM, see Section 3.6.2) was implemented based on the available standard k-ω model in OpenFOAM. This was achieved by adding the relevant parameters and fields to the class. For the implementation of the k-ω SSTF model, the available k-ω SST model was adapted by modifying the relevant equations as described in Section 3.6.3.